UC Santa Barbara

UC Santa Barbara Electronic Theses and Dissertations

Title

Onset and Deglaciation of Cryogenian Snowball Earth

Permalink

https://escholarship.org/uc/item/7qx990jr

Author

Pu, Judy Pin

Publication Date

2023

Supplemental Material

https://escholarship.org/uc/item/7qx990jr#supplemental

Peer reviewed|Thesis/dissertation

UNIVERSITY OF CALIFORNIA

Santa Barbara

Onset and Deglaciation of

Cryogenian Snowball Earth

A dissertation submitted in partial satisfaction of the

requirements for the degree Doctor of Philosophy

in Earth Science

by

Judy Pin Pu

Committee in charge:

Professor Francis Macdonald, Chair

Professor Roberta Rudnick

Professor Matthew Rioux

September 2023

The dissertation of Judy Pin Pu is approved.

_____

Roberta Rudnick

_____

Matthew Rioux

_____

Francis Macdonald, Committee Chair

June 2023

Onset and Deglaciation of

Cryogenian Snowball Earth

ACKNOWLEDGEMENTS

Elizabeth Erickson will travel to the ends of the Earth to rescue me if they need to. Thanks also to Adrian, Anna, and Sam Lo for being my family in Santa Barbara.

I am very grateful to Patience, Julia, and Rin, whose company during undergraduate and graduate school gave me some of my happiest and most memorable experiences. This dissertation would not have been written without Patience spending hours and hours working alongside me and Rin's encouragement for my defense.

Finally, I would like to thank my family for their unconditional support and for making my education possible.

DEDICATION

This dissertation is dedicated to Professor Sam Bowring.

In my second year of college, I got to celebrate Sam's 60th birthday with his lab group. They had gone all out and gotten a blow-up dinosaur balloon and a big piñata for his birthday, but Sam was hard to track down in the days leading up to it. I remember worrying that maybe he was embarrassed or nervous to turn 60, so I decided to write him a birthday card. In the card, I tried to impress on him what a historic occasion a 60th birthday was, especially in Chinese culture (my parents had just informed me for their own purposes), and how lucky we all were to be able to celebrate his 60th with him. He showed up for his party eventually, made a big show of using his sledgehammer to take down the piñata, and the following week when it was my birthday, he had a card for me too. The cover had a cartoon of Noah's ark and all the animals walking aboard except for one pair who were hanging out, reading and tanning on a beach towel, probably about to miss their ride. Though the caption said, "Relax, it's your birthday," the message when coupled with the cartoon was more like, "relax at your own peril." It was a fitting card to receive from a professor who rarely took time to relax himself. He wrote in the card how glad he was that I had joined the lab, and he was looking forward to seeing me start my own projects. I have looked back on this card many times during my PhD to remember his encouragement.

I learned so many things from Sam, from how to make a good field chili to how to approach complex global problems. He had a dry, biting sense of humor but his cynicism did not extend to his undergraduate students; he was steadfast in his belief that each of us could make a difference in the world. He never let us settle or say that it was too late to change things. He made it his goal to impart that sense of self-worth and ambition to his first-year

class every year. I would not be where I am today if it wasn't for Sam Bowring, and I cannot

thank him enough for all that he did for me.

JUDY PIN PU

Santa Barbara, CA | (646) 431-0568 | judypu@ucsb.edu

EDUCATION

University of California, Santa Barbara (UCSB)   2018-Present

    PhD Candidate, Earth Sciences
    Advisor: Dr. Francis A. Macdonald

Massachusetts Institute of Technology (MIT)   2012-2016

    S.B. in Earth, Atmospheric, and Planetary Sciences

RESEARCH EXPERIENCE

University of California, Santa Barbara; Harvard University   *Aug. 2016-Present*
PhD Dissertation: Constraining the onset and deglaciation mechanisms of Cryogenian Snowball Earth glaciations
Projects: Emplacement of the Franklin LIP and initiation of the Sturtian Snowball Earth; paleogeographic and sedimentary models for Cryogenian glaciations on Kalahari Craton

    Fieldwork: Mapped and measured sections during the summers of 2017-2019 in the Naukluft Nappes and on Farm Trekpoort by Rosh Pinah, Namibia.

    Lab work: Mineral separation, thin section petrography, cathodoluminescence (CL) imaging, lab chemistry for chemical abrasion-isotope dilution-thermal ionization mass spectrometry (CA-ID-TIMS) and Sm-Nd isotopes, whole rock geochemistry for XRD analyses, laser ablation split stream analyses (LASS) using an inductively coupled plasma mass spectrometer (ICPMS) and multi-collector (MC-ICPMS).

MIT Radiogenic Isotope Lab Cambridge, MA   *June 2013–June 2016*
Undergraduate senior thesis: Geochronological constraints on the Trinity Diamictite in Newfoundland: Implications for Ediacaran glaciation

    Fieldwork: Mapping and stratigraphy on Bonavista Peninsula, Newfoundland in Aug. 2015.

    Lab work: Performed mineral separation, CA-ID-TIMS, column chemistry and TIMS for Pb and Sr isotopes, solution-ICPMS of water samples.

LDEO Argon Geochronology Lab Palisades, NY   *May–July 2015*
Project: K/Ar geochronology as a tool for tracing dust provenance in the Southern Hemisphere

    Lab work: Sieved and settled samples to collect different grain size distributions for radiogenic isotope geochemistry, performed noble gas mass spectrometry.

PUBLICATIONS AND TALKS

5. Pu, J. P., Macdonald, F. A., Schmitz, M. D., Rainbird, R. H., Bleeker, W., Peak, B. A., Flowers, R. M., Hoffman, P. F., Rioux, M., Hamilton, M. A., 2022, Emplacement of the Franklin large igneous province and initiation of the Sturtian Snowball Earth, *AGU Fall Meeting*, invited speaker.
4. Pu, J. P., Macdonald, F. A., Schmitz, M. D., Rainbird, R. H., Bleeker, W., Peak, B. A., Flowers, R. M., Hoffman, P. F., Rioux, M., Hamilton, M. A., 2022, Emplacement of the Franklin large

igneous province and initiation of the Sturtian Snowball Earth, *Science Advances*, https://doi.org/10.1126/sciadv.adc9430.

3. Pu, J. P., Macdonald, F. A., Schmitz, M. D., Rainbird, R. H., Bleeker, W., Peak, B. A., Flowers, R. M., Hoffman, P. F., Rioux, M., Hamilton, M. A., 2022, Emplacement of the Franklin large igneous province and initiation of the Sturtian Snowball Earth, *Virtual Seminars in Precambrian Geology*, https://youtu.be/3Z8FXR49c64.

2. Pu, J. P., Schmitz, M. D., Crowley, J. L., Rainbird, R. H., and Macdonald, F. A., 2018, Geochronological constraints on the emplacement of the Franklin LIP: Testing hypotheses for the onset of the Sturtian snowball Earth, *Goldschmidt Conference,* oral presentation.

1. Pu, J. P., Bowring, S. A., Ramezani, J., Myrow, P., Raub, T. D., Landing, E., Mills, A., Hodgin, E., and Macdonald, F. A., 2016, Dodging snowballs: Geochronology of the Gaskiers glaciation and the first appearance of the Ediacaran biota, *Geology*, https://doi.org/10.1130/G38284.1.

LEADERSHIP/TEACHING EXPERIENCE

Harvard, UCSB Research Mentor *June 2017–Present*
Taught and mentored undergraduates and graduate students as field and lab assistants.

UCSB Earth Science Student JEDI Council *Jan. 2020–Present*
Create and work on initiatives to advance equity within the geosciences.

Instructor and teaching assistant, UCSB Earth Sciences *Oct. 2020–June 2023*
Instructor of record for Earth 123 (The Solar System) in Summer 2021, TA for several classes

UCSB Women in STEM Mentoring Program (WiSMP) Mentor *Oct. 2019–Mar. 2019*

UCSB Pillars of Teaching Assistantship Certificate *Oct. 2019–Dec. 2019*

Harvard Women in STEM (WiSTEM) Mentor *Sept. 2017–May 2018*

Terrascope (MIT) Associate Advisor and Teaching Fellow *Sept. 2013–May 2016*

MIT Educational Studies Program: Splash *Nov. 2015*
Taught an introductory geology course to high school students

SCHOLARSHIPS AND AWARDS

NSF GRFP Fellowship *Mar. 2017–2022*

Gordon Research Conference in Geochronology Scholarship *July 2019*

Lloyd and Mary Edwards Field Studies Fellowship *June 2019*

Phi Beta Kappa *May 2016*

Marshall Scholarship Finalist *Oct. 2015*

MIT EAPS Achievement Award, for focused course work and leadership *May 2015*

MIT EAPS Excellence as Undergraduate Teaching Assistant, for 12.001 *May 2015*

ABSTRACT

Onset and Deglaciation of

Cryogenian Snowball Earth

by

Judy Pin Pu

Cryogenian Snowball Earth glaciations are some of the most extreme changes in Earth's climate through its history. Decades of work have established the global ubiquity of Snowball Earth sedimentary deposits and their synchroneity in time, yet key questions remain concerning the potential causes for global glaciations and their drastically different durations and expressions in the rock record. This dissertation addresses these questions and proposes explanations for the onset of global glaciation and how the abrupt termination of a Snowball event could explain the differences in chemical sediments seen between the two Cryogenian Snowball events.

In Chapter 1, I evaluate the emplacement of a large igneous province as a potential trigger for the Sturtian Snowball Earth (717-661 Ma). This work was done in collaboration with Francis A. Macdonald, Mark D. Schmitz, Robert H. Rainbird, Wouter Bleeker, Barra A. Peak, Rebecca M. Flowers, Paul F. Hoffman, Matthew Rioux, and Michael A. Hamilton. Previous geochronology has suggested a rough coincidence of glacial onset with one of the largest magmatic episodes in the geological record, the Franklin large igneous province. I show that

chemical abrasion-isotope dilution-thermal ionization mass spectrometry (CA-ID-TIMS) U-Pb geochronology on zircon and baddeleyite from sills associated with the paleo-equatorial Franklin large igneous province in Arctic Canada record rapid emplacement between 719.86 ± 0.21 and 718.61 ± 0.30 Ma ago, 0.9 to 1.6 Ma before the onset of widespread glaciation. Geologic observations and (U-Th)/He dates on Franklin sills are compatible with major post–Franklin exhumation, possibly due to development of mafic volcanic highlands on windward equatorial Laurentia and increased global weatherability. After a transient magmatic CO_2 flux, long-term carbon sequestration associated with increased weatherability could have nudged Earth over the threshold for runaway ice-albedo feedback.

In Chapter 2, I address whether there is evidence for glaciations in the 50 Myr prior to the Sturtian glaciation by examining the proposed ca. 750 Ma Kaigas glaciation. I evaluate this hypothesis at the eponymous location with detailed stratigraphy and geochronology through the Kaigas, Rosh Pinah, and Numees formations on the western margin of the Kalahari craton in southern Namibia. This work was done in collaboration with Francis A. Macdonald, Emily F. Smith, Jahandar Ramezani, and Nicholas Swanson-Hysell. We find that glacial deposits previously assigned to the Kaigas Formation are instead ca. 717-661 Ma diamictites of the Sturtian Numees Formation. Pre-Numees strata, including the Kaigas Formation, host facies associations diagnostic of fan delta deposition along an active normal fault. Interbedded volcanic rocks in the Rosh Pinah Formation overlying the Kaigas Formation were dated with U-Pb CA-ID-TIMS on zircon at ca. 752 Ma. These Tonian deposits are interpreted as being deposited in an active rift basin without evidence for glaciation. Rosh Pinah magmatism could be correlative with the Mount Rogers Complex in Virginia, USA, consistent with a scenario of the Kalahari craton actively rifting from Laurentia and associated terranes within 20º of the

equator at the time. We conclude that, at least in marine settings, evidence for low-latitude glaciation is limited to the 717-635 Ma Cryogenian Period.

In Chapter 3, I propose an explanation for why the Sturtian and Marinoan glaciations differ. This work was done in collaboration with Mark D. Schmitz and Francis A. Macdonald. I present new geological mapping, measured stratigraphic sections, and U-Pb zircon geochronology and geochemistry on Cryogenian successions exposed in the Naukluft Nappes of Namibia. Stratigraphic sections measured in the context of geological mapping document glacial deposition on a slope setting below the ice grounding line. Deglaciation is marked by an abrupt coarsening, boulder-sized dropstones, and the appearance of volcaniclastic deposits. Large lithic fragments within the volcaniclastics and detrital zircon provenance using laser ablation split stream mass spectrometry suggest a local source. CA-ID-TIMS on these units yielded a weighted mean $^{206}Pb/^{238}U$ date of 635.84 ± 0.22/0.29/0.71 Ma, which is interpreted as a depositional age. We suggest that glacio-isostatic unloading reactivated the formerly rifted passive margin. This age overlaps with dates near the top of Marinoan glacial deposits on the Swakop terrane, Australia, and South China. We suggest that all of these dates record deglaciation and that deglacial volcanism associated with isostatic unloading provided a positive feedback for both albedo and CO_2 that shortened the Marinoan glaciation.

TABLE OF CONTENTS

I. Emplacement of the Franklin large igneous province and initiation of the Sturtian Snowball Earth

A. Introduction

Sedimentological, paleomagnetic, and geochronological data have established the presence of ice at low latitudes during the Cryogenian Period (720–635 Ma), providing evidence for two global glaciations, the Sturtian (~717-659 Ma) and Marinoan (>639-635 Ma) (*1*). The Snowball Earth episodes are the most extreme climate changes in Earth's history, and yet the triggers for their initiation remain unclear and debated. Studies of the emplacement of large igneous provinces (LIPs) have demonstrated correlations with environmental perturbations (*2, 3*), and geochronological constraints on the older of the two episodes, the Sturtian Snowball Earth, have highlighted a possible correlation in timing of onset with the emplacement of the Franklin LIP (e.g., *4, 5*).

Previous work has attributed the global cooling that led to the Sturtian glaciation to LIP emplacement, either because of drawdown of CO_2 by silicate weathering for millions of years following eruption of the Franklin LIP (*4, 6–8*), or the immediate effects from the radiative forcing of sulfur aerosol emissions (*5*). Several paleomagnetic studies have demonstrated that the Franklin LIP was emplaced at tropical latitudes (e.g., *9, 10*), which is critical for both hypotheses as the climate impact of changes in weatherability and albedo are both strongly latitude dependent (*5, 6*). Past U-Pb geochronology studies have also produced emplacement ages for the Franklin LIP ranging from 750–710 Ma (*4, 10–13*), which roughly coincide with constraints on the establishment of steady-state ice margins and the onset of Sturtian glaciation between 717.4 ± 0.2 Ma and 716.9 ± 0.4 Ma (*14*), but the published

uncertainties are too large to determine whether there is a causal link between LIP emplacement and the onset of the Sturtian glaciation or differentiate between the proposed climate cooling mechanisms.

In the past several years, geochronology studies have constrained the duration and tempo of LIP emplacement, showing that >75% of total volume is emplaced in pulses of <5 Myr, with almost all high-precision studies showing emplacement in <1 Myr (*3*, *15*). Based on the established rates for LIP emplacement, the actual duration of emplacement for the Franklin LIP could be only a small portion of the current range in dates, highlighting the need for higher precision and accuracy in dating.

Obstacles to the accurate and precise dating of Proterozoic LIPs have included the lack of felsic, zircon-rich rocks and the extent of radiation damage in Proterozoic zircon grains, which often leads to pervasive Pb-loss. In this study, we used U-Pb isotope dilution-thermal ionization mass spectrometry (ID-TIMS) on zircon and baddeleyite extracted from intermediate to felsic differentiates of the Franklin LIP from locations across Arctic Canada. Whole-rock geochemistry was used to place precisely dated samples in the context of an emplacement model to clarify the relationship between the Franklin LIP and the onset of glaciation. To minimize the impact of Pb-loss, we used the chemical abrasion method (*16*), in most cases dating minute, remnant fragments from aggressive dissolution of uranium-rich zircon crystals. Apatite and zircon (U-Th)/He thermochronology dates were also obtained and combined with geologic observations to evaluate the timing and magnitude of post-emplacement exhumation.

1. Geologic setting

The Franklin magmatic event is one of the largest preserved LIPs in the geological record (*17*). Sills and dykes of the Franklin LIP (*9*) stretch from Alaska across Arctic Canada, from Victoria Island to Baffin Island and into Greenland (*9, 10*) (Fig. 1). Some sills previously mapped as part of the 1.27 Ga Mackenzie magmatic event (*18*) are now recognized as part of the Franklin LIP, extending the coverage of the LIP farther south to Great Slave Lake (*19*). Assuming that these intrusions fed an extrusive continental flood basalt province that was later eroded away, the outline of this area traces a half circle that covers >5 Mkm^2 of North America with dykes radiating away from a focal point north of Banks Island (Fig. 1). If there was a conjugate margin of similar area radiating away in the opposite direction that later rifted away, potentially in Siberia (*20*), the Franklin LIP would be of comparable size to the ~11 Mkm^2 Central Atlantic Magmatic Province (CAMP) and much larger than the 4 Mkm^2 Siberian traps (*17*).

The Franklin LIP was emplaced on the Arctic margin of Laurentia prior to the rifting of Siberia (*20*), and directly after rifting of North China from the northwest Cordillera (*21*), creating an open margin. During an earlier stage of rifting of the Cordilleran margin, the ca. 778 Ma Gunbarrel LIP was emplaced from Wyoming to Yukon and across the western Slave craton (Fig. 2) (*22*). The Gunbarrel LIP may have covered much of western North America with basalt, but the extrusive component is only preserved in narrow, post-778 Ma rift basins in the Mackenzie Mountains. In the Yukon, these late Tonian rift basins were reactivated by Franklin-age magmatism (*4*).

In Arctic Canada, the Franklin LIP intrudes Archean to Paleoproterozoic basement and Paleoproterozoic to Neoproterozoic sedimentary rocks and is locally preserved as extensive basalt flows on Victoria Island (Fig. 2). Initial observations of dykes feeding

multiple sills at different stratigraphic levels and crosscutting extrusive parts of the Franklin LIP led to the conclusion that the emplacement of the sills, dykes, and flows were all closely linked in time (*23*). Franklin sills range from 1–100 m thick and show geochemical evidence for both fractional crystallization and crustal contamination (*23–25*). Much of the Franklin LIP has been eroded away, but to capture the geographic and compositional range of the Franklin LIP, samples for the present study include sills and dykes from the Amundsen Basin (Minto Inlier on Victoria Island, the Brock Inlier on the southern Amundsen Gulf, the Coppermine area in Coronation Gulf), Great Slave Lake, and the Cumberland Peninsula on Baffin Island (Fig. 1).

The best exposures of the intrusive and extrusive relationships of the Franklin LIP units are on Victoria Island, where the bulk of the volcanostratigraphic relationships have been established and provide a geochemical framework for the rest of the Franklin LIP (*23, 25–27*). On Victoria Island, the >4 km-thick Shaler Supergroup includes organic-rich shale and sulfate evaporites (*28, 29*) and is succeeded by a >1 km-thick flood basalt sequence, the Natkusiak Formation (*30*). In southwestern exposures, the Shaler Supergroup and Natkusiak Formation contact is conformable, but to the northeast the contact is unconformable and marked by sedimentary breccia (*29, 31*). This northeastward pinch-out of the Shaler Supergroup has been interpreted to record doming of the crust associated with the impingement of the Franklin LIP mantle plume (*31*). The Natkusiak Formation consists of basal rubbly flows, volcaniclastic units, and thick sheet flows of basalt (*26, 32*). Franklin sills intruded the basal Natkusiak Formation and have been linked stratigraphically with crosscutting dykes and geochemically with different extrusive flow types (*11, 26, 27*), providing coarse-grained equivalents to the extrusive units that can be more easily and reliably

dated. Evidence for glaciation has not been documented below or within the Natkusiak Formation, and the sub-Cambrian unconformity (*33*) precludes further stratigraphic constraints on the relationship between the Franklin LIP and the Sturtian glaciation. Gentle folding of the sub-Cambrian stratigraphy on Victoria Island (Figs. 1, 2) may be associated with plume emplacement, which can generate intraplate deformation and surface topography (*34*).

In the East Arm of Great Slave Lake, the ~50–250 m-thick Douglas Peninsula sill intrudes sedimentary and volcanic rocks of the Paleoproterozoic Great Slave Supergroup and Et-then Group (*19*) (Fig. 2). Three potential paths for how the Franklin LIP mantle plume could have fed the Douglas Peninsula sill on Great Slave Lake are shown on Figure 2: Path 1, a plume-fed mantle flow around the keel of the Slave craton at depth; Path 2, southward propagating dykes (parallel to the plane of the section) through the crust of the Slave craton; and Path 3, southward continuation of the original sill province in the Proterozoic cover of the Slave craton. In each of these scenarios, we assume these intrusions were linked to flows that mantled the surface with Franklin-age extrusive volcanic rocks, which were later removed by exhumation and erosion below the sub-Cambrian unconformity.

2. Geochemical classification of Franklin LIP rocks

Major and trace element signatures of mantle sources and crustal contamination distinguish emplacement of earliest plume head magmas from later stages of continental flood basalt magmatism (e.g., *15*, *35*). Similarly, the Franklin LIP has been categorized into Type 1 and Type 2 magmatic phases based on TiO_2 wt. % and light rare earth element (LREE) to heavy rare earth element (HREE) ratios (*25*, *36*). This classification and stratigraphy for the

Franklin LIP provides a framework for linking our dates with the spatial extent and relative ages of different magma types.

Most of the Franklin LIP has tholeiitic compositions with 45–51 wt. % SiO_2 and 6–11 wt. % MgO (*24, 27*). Low-Ti (<1.2 wt. % TiO_2; *36*) Type 1 intrusive and volcanic rocks are stratigraphically below or are crosscut by the younger, high-Ti Type 2 igneous rocks and tend to have incorporated more crustal material, resulting in relatively lower Nb/La ratios, enriched LREEs and steeper REE slopes, and lower initial ε_{Nd} (-6.1 to -0.8) and ε_{Hf} (-4.3 to +4.6) values (*27, 36*). Type 1 rocks also include olivine-rich cumulates and generally have higher wt. % MgO (*25, 27*).

Type 2 rocks are generally more differentiated, are dominated by clinopyroxene and plagioclase, and have lower Ce/Yb ratios, higher Nb/La ratios, and higher initial ε_{Nd} values (*27*). Type 2 Franklin sills and upper Natkusiak sheet flow basalts have values of ε_{Nd} = +1 to +8.8 and ε_{Hf} = +4.7 to +15.8, which indicate lesser degrees of contamination by continental crust (*27*).

Type 1 rocks have been associated with early and limited magmatism while the younger Type 2 rocks have been linked to voluminous melting and the main phase of flood volcanism (*26, 27*), making them the main targets of this study.

B. Results

1. Trace element and isotope geochemistry

Major element compositions along with minor and trace element concentrations are presented in Table S1. Normalized minor and trace element concentrations are plotted in Fig. S1. The 93JP-71 samples from Victoria Island and F1966 from Great Slave Lake show slightly

LREE-enriched, concave downward REE patterns with negative Eu anomalies (Fig. S1). Granitic sample 93JP-71JB shows an enrichment in total REEs relative to the gabbroic sample 93JP-71M, consistent with differentiation. Samples 93JP-93L from the Duke of York Inlier and 14RAT-513A from the Brock Inlier show similar REE patterns to the other 93JP samples and F1966 but are slightly LREE-enriched and more HREE depleted. In contrast, samples 17RAT-R35B1 from the Coppermine area, FA700408 from Baffin Island, and S8 from Victoria Island have steeper REE patterns and all show more LREE-enrichment than the other samples.

Values for $(Ce/Yb)_{CH}$ (normalized to chondrite) reflect the REE slopes and are lowest for F1966 (1.30) and the 93JP-71 samples (1.60–1.84). $(Ce/Yb)_{CH}$ values increase to 2.41 for 14RAT-513A and 2.97 for 93JP-93L. Values for S8, FA700408, and 17RAT-R35B1 range from 3.41–7.64.

Values of $(Nb/La)_{PM}$ (normalized to primitive mantle) for the 93JP-71 samples and F1966 are close to 1.0 (0.96–1.01 and 1.01, respectively). Sample 14RAT-513A has a slightly lower $(Nb/La)_{PM}$ value of 0.74 and FA700408 has a $(Nb/La)_{PM}$ of 0.68. Samples 17RAT-R35B1 and S8 have the lowest $(Nb/La)_{PM}$ values of 0.20 and 0.42, respectively.

The $\varepsilon_{Nd}(t)$ values calculated for an age of 719 Ma cover a wide isotopic range (Table S2). Samples 17RAT-R35B1 and S8 have similarly negative ε_{Nd} values, -4.87 and -5.10, while all other samples have positive ε_{Nd} values ranging from 1.72 (FA700408) to 6.59 (F1966). Fig. S2 plots $(Ce/Yb)_{CH}$ vs. $\varepsilon_{Nd}(719$ Ma) for the samples in this study compared to data from (*27*).

2. Geochronology

New high-precision U-Pb zircon geochronology yielded weighted mean $^{206}Pb/^{238}U$ dates for the samples from Coppermine area (17RAT-R35B1), Minto Inlier (93JP-71JB), Duke of York Inlier (93JP-93K, 93JP-93L), Brock Inlier (14RAT-513A), and Great Slave Lake (F1966) that range between 719.86 ± 0.21 to 718.61 ± 0.30 Ma (Figs. 3, 4; Tables S3, S5). Concordia plots for all zircon analyses are presented in Fig. 3 and plots for baddeleyite analyses are included in the Supplemental Materials (Fig. S3). Uncertainties for weighted mean dates in this study are reported as ± X/Y/Z, where X represents internal error only, Y includes tracer calibration uncertainties, and Z includes both tracer calibration and decay constant uncertainties for comparisons with different isotopic chronometers. For comparisons of analyses produced using the same isotopic tracers and techniques, only internal errors will be discussed. Tracer calibration uncertainties are included (Y error bounds) for interlaboratory comparisons with analyses that used different isotopic tracer solutions.

Nine fractions of 93JP-71JB yielded a weighted mean $^{206}Pb/^{238}U$ date of 719.04 ± 0.19/0.28/0.79 Ma (n = 9/13, MSWD = 0.41)—the four excluded dates overlap the other dates within uncertainty but have significantly larger uncertainties and did not meaningfully contribute to the weighted mean. Sample 93JP-93K yielded an array of concordant and discordant data that plot along a line defined by recent Pb-loss (Fig. 3). The weighted mean of the four oldest, most concordant analyses provided a $^{206}Pb/^{238}U$ date of 718.77 ± 0.30/0.36/0.82 Ma (n = 4/10, MSWD = 0.84). Sample 93JP-93L also showed evidence for Pb-loss. Excluding two younger analyses resulted in a single, statistically coherent population with a weighted mean $^{206}Pb/^{238}U$ date of 718.96 ± 0.21/0.29/0.79 Ma (n = 11/13, MSWD = 1.82). Sample 14RAT-513A had metamict zircon grains. A weighted mean of the nine oldest analyses produced a date of 718.61 ± 0.30/0.36/0.82 Ma (n = 9/10, MSWD = 3.71). Given the

metamict nature of the analyzed grains, the excluded younger analysis is likely impacted by Pb-loss.

Analyses for samples 17RAT-R35B1 and F1966 produced an array of dates along concordia and each had at least one significantly older analysis. No single weighted mean date could be determined from the data collected. Considering only the analyses that overlapped within uncertainty and produced an MSWD consistent with a single population, the older grains for the main data cluster for sample 17RAT-R35B had a weighted mean of 719.86 ± 0.21/0.30/0.79 Ma (n = 6/15, MSWD = 2.18) and the six older analyses that overlapped within uncertainty for F1966 produced a weighted mean of 719.08 ± 0.22/0.30/0.79 Ma (n = 6/18, MSWD = 1.41).

Baddeleyite analyses for sample FA700408 (Baffin Island) generally plotted below concordia, although two grains overlapped concordia within uncertainty (Fig. S3). The upper-intercept date for the three analyses constrained to a present-day Pb-loss line was 718.94 ± 1.60 Ma (95% CI, n = 3/4, MSWD = 1.1). A single zircon analysis from this sample was excluded for its large uncertainty. Finally, a date for sample S8 (Victoria Island) was previously published in (4) but was recalculated with updated spike calibrations and U blank estimates for Figure 4B, to be consistent with the data from the present study. The revised U-Pb baddeleyite $^{206}Pb/^{238}U$ date for the S8 sample is 715.19 ± 0.41 Ma (n = 5/7, MSWD = 1.99). The calculated upper-intercept date for S8 is 725.73 ± 3.55 Ma (95% CI, n = 7/7, MSWD = 1.1).

3. Thermochronology

New (U-Th)/He dates were obtained for sample F1966 in the southern part of the study region to investigate the post-emplacement thermal and exhumation history. A total of six zircon and six apatite (U-Th)/He (ZHe, AHe) dates were determined (Table S6). ZHe dates span from 42 ± 4 to 641 ± 24 Ma (date uncertainty is the propagated 2σ analytical uncertainty) and are negatively correlated with effective uranium concentration (eU), a radiation damage proxy (Fig. S5). AHe dates are Phanerozoic. Thermal histories able to explain these data were investigated with inverse thermal history modeling (see supplemental text, Fig. S5, Table S7).

C. Discussion

1. Geochemistry of Type 1 and Type 2 Franklin LIP rocks

The relatively high (Nb/La)$_{PM}$ and low (Ce/Yb)$_{CH}$ ratios for the 93JP-71, 93JP-93, F1966, and 14RAT-513A samples, coupled with positive initial $\varepsilon_{Nd}(t)$ values and their geographic location, suggests that these samples are from the Type 2 high-volume phase of Franklin magmas. Samples 17RAT-R35B1 and S8 are distinct from the other samples in their negative initial $\varepsilon_{Nd}(t)$ values. The two samples—along with FA700408—show steeper REE patterns (Fig. S1), with high (Ce/Yb)$_{CH}$ (3.41–7.64) and lower (Nb/La)$_{PM}$ values (0.20–0.42) reflecting more crustal contamination, which is consistent with a Type 1 classification. A plot of (Ce/Yb)$_{CH}$ vs. ε_{Nd} shows that samples 93JP-93, 93JP-71, 14RAT-513A, F1966 either plot close to or overlap with values for Type 2 rocks, while S8 and 17RAT-R35B1 are more similar to Type 1 rocks (Fig. S2). Sample FA700408 shows incorporation of more crustal material in terms of LREE enrichment and a higher $\varepsilon_{Nd}(t)$ value. These values could reflect a separate high ε_{Nd} mantle source like Southern Type 1 basalts (see supplementary text), but with considerably more crustal contamination.

2. Interpretation of the U-Pb dates

We interpret the weighted mean ^{206}Pb/^{238}U dates for samples 93JP-71JB, 93JP-93K, 93JP-93L, and 14RAT-513A to reflect the intrusion and crystallization age of Franklin sills between 719.04 ± 0.19 to 718.61 ± 0.30 Ma (Fig. 4A, Table S3). These are new, high-precision age constraints for the younger and more voluminous Type 2 set of Franklin LIP magmas. Samples 17RAT-R35B1 and F1966 yielded more ambiguous results, with a range of dates along concordia. In the context of the other dated samples, the oldest analyses seen in 17RAT-R35B1 and F1966 are taken to represent either antecrysts or possibly Pb implantation in the grain domains analyzed following annealing and chemical abrasion; the chemical abrasion process preferentially leaches away the more damaged, U-rich domains, and residual lower U domains could include implanted Pb, resulting in reversely discordant analyses in extreme cases (16, 37). These samples both have prismatic crystals that commonly have melt channels parallel to their c-axes and simple broad zoning in cathodoluminescence (CL) images, such that we consider it unlikely that most grains contain inclusions of older grains at their centers. However, some grains from F1966 have convolute and irregular zoning in CL that could point to metamictization and/or partial resorption of older, antecrystic zircon. Antecrystic zircon grains in mafic systems have been attributed to the fact that in dry and fast-cooling magmas, zircon is relatively difficult to dissolve and so the resulting dyke or sill may preserve older populations of zircon that do not record its emplacement age (38). We therefore interpret the weighted mean ^{206}Pb/^{238}U date of the oldest population of analyses with an MSWD representing a single population—excluding the older outliers as inherited antecrysts—in samples 17RAT-R35B1 and F1966 as the best estimate of the age of intrusion (719.86 ± 0.21

11

Ma and 719.08 ± 0.22 Ma, respectively). Following this interpretation, the younger analyses in these samples reflect pervasive Pb-loss. While the range of dates observed in these samples preclude a definitive age interpretation, our preferred weighted mean dates are consistent with the dates from the four samples with simpler U-Pb systematics and the stratigraphic order of the intrusive rocks (i.e., the date from Type 1 sample 17RAT-R35B1 is older than the dated Type 2 intrusive rocks).

There are several petrological and geochemical reasons to ascribe the majority of geological variance in the measured U-Pb dates to Pb-loss, including high uranium concentrations, age, accumulated radiation damage, and metamictization of the crystal lattice. These phenomena are directly confirmed in the unusually high solubility (>95% dissolution) of the zircon grains during chemical abrasion for most samples. As such our interpretation of the crystallization age of the sills as represented by the oldest major cluster of $^{206}Pb/^{238}U$ dates is necessarily distinct from strategies pursued in younger silicic tuffs or interbedded volcaniclastic strata within flood basalt lava piles, where Pb-loss can be minor and readily mitigated while crystal recycling and detrital inheritance are often profound (e.g., *3*).

We consider the new zircon dates from this study to provide the best estimate of the timing and duration of Franklin LIP magmatism because the data come from an internally consistent dataset of high precision, chemical abrasion analyses spanning a large portion of the Franklin LIP's geographic range. All of our zircon weighted mean dates—excluding the Type 1 17RAT-R35B1 sample—overlap within 2σ uncertainty, indicating broadly synchronous emplacement of the Franklin LIP Type 2 intrusions and volcanic rocks. The data capture a snapshot of emplacement for voluminous Type 2 rocks spanning 0.47 ± 0.37 Myr (2σ uncertainties added in quadrature). The interpreted older date from 17RAT-R35B1, which

has geochemistry more representative of Type 1 rocks, is consistent with the cross-cutting relationships constraining Type 1 to be older than Type 2 intrusions and volcanic rocks. Together with the Type 2 rocks dated in this study, the duration of emplacement captured is 1.25 ± 0.37 Myr (2σ uncertainties added in quadrature). If this range captures the main emplacement period of the Franklin LIP, the duration of emplacement would be similar in tempo with other well-dated LIPs (e.g., *3*, *15*).

Our new and previously published baddeleyite U-Pb results are somewhat more complex. The published baddeleyite date from sample S8 is based on single-grain baddeleyite measurements conducted in the same lab as this study. The geochemistry of sill S8—which we present here—is more consistent with the criteria for older Northern Type 1 rocks, but the recalculated weighted mean $^{206}Pb/^{238}U$ date for this sample (715.19 ± 0.41 Ma) is younger than our new zircon dates from other samples (719.86 ± 0.21 to 718.61 ± 0.30 Ma). We suspect this younger date may reflect more extensive Pb-loss, which can be difficult to distinguish from concordant analyses if uncertainties overlap with concordia. If the dates for S8 are discordant due to Pb-loss, the upper-intercept date would more accurately represent the age of crystallization; however, the calculated upper-intercept date for S8 is 725.73 ± 3.55 Ma, which overlaps in uncertainty with previous upper-intercept dates (*11*) but is older than the zircon dates obtained in this study. The offset between zircon and baddeleyite dates may reflect additional complexities in interpreting baddeleyite dates due to factors such as intra-grain Pb migration (*39*), excess ^{207}Pb due to ^{231}Pa enrichment or ^{222}Rn loss (*40*), and Pb-loss (*41*).

Baddeleyite separated from a sample (FA700408) from Baffin Island in this study produced largely discordant analyses, but the weighted mean $^{206}Pb/^{238}U$ value of the two

analyses closest to concordia would give a date closer to 712 Ma, which is similar to previous baddeleyite geochronology in the same area (e.g., *10*, *13*). If instead the dates were considered discordant due to Pb-loss and an upper-intercept age was calculated for the analyses, the date for the sample would be 718.94 ± 1.60 Ma, largely consistent with the dates obtained from zircon and more consistent with established timescales of emplacement for LIPs (*3*).

The range of zircon dates in our samples is significantly shorter than the ~40 Myr range in dates previously obtained on the Franklin LIP, which was a result of both higher uncertainties in most of the published data and a wider range of measured dates. Most of the existing dates are from single grain or bulk (multiple grains) baddeleyite analyses, and one analysis ("Lower Sill" sample from Victoria Island; *11*) involved both bulk zircon and bulk baddeleyite fractions. These analyses predate the development of the chemical abrasion method for addressing Pb-loss in zircon (*16*), and there is currently no chemical abrasion approach for treating Pb-loss in baddeleyite (cf. *41*). Previously published dates that are younger than the dates obtained in this study may therefore be impacted by post-crystallization Pb-loss. Inter-laboratory biases and systematic errors in different tracer calibrations further complicate direct comparisons between our new results and published data. We consider the zircon dates—which are based on a single, well understood mineral system—to provide the most robust estimate of the timing and duration of Franklin LIP magmatism.

3. Temporal relationship to onset of the Sturtian Snowball Earth

The new emplacement age of the Franklin LIP, between 719.86 ± 0.21 to 718.61 ± 0.30 Ma, is older than previous constraints for the onset of the Sturtian glaciation between 717.4 ± 0.2 Ma and 716.9 ± 0.4 Ma (also analyzed in the BSU Isotope Geology Laboratory

using the same tracer calibration; *14*) by 0.9–1.6 Myr (Figs. 4 and 5). Onset is constrained by dates on ca. 718.1–717.4 Ma rhyolite flows in member D of the Mt. Harper Volcanic Complex. These rhyolite flows underlie a basalt flow in member E with wrinkled and ropey textures (*42*) and are unconformably overlain by glacial diamictite of the Eagle Creek Formation, which has interbedded ca. 716.9–716.5 Ma volcanic tuffs (*14*). The ropey texture, hyaloclastic breccia, bulbous isolated pillow basalts, and lack of obvious subaqueous textures in member E were interpreted to record subaerial eruption (*42*), consistent with predating global glacial onset (*14*); however, similar tubular and bulbous structures, isolated pillows, and ropey textures have been described in subglacial settings (*43*, *44*), such that the subaerial and pre-glacial interpretation is non-unique, and member E alternatively may have been emplaced in a subglacial setting in an environment like Antarctica's dry valleys. Given these limitations, the interpreted constraint on the onset of the Sturtian glaciation based upon the ca. 717.4 Ma volcanic rocks should only be taken as a minimum age constraint on Sturtian onset. It could have taken up to several 100 kyr after the ocean froze over for continental ice sheets to thicken sufficiently to flow and produce glacial structures at their periphery (*45*, *46*).

Other strict age constraints on the maximum age for the initiation of the Sturtian glaciation come from Ethiopia, South China, and Arctic Alaska and have all yielded ages of ca. 719–720 Ma in pre-glacial strata (Fig. 5; *47–49*). Glacial onset ages have been extrapolated in Monte Carlo simulations estimating sedimentation rates to the base of the glacial diamictite using the maximum age constraints from Ethiopia and South China and have yielded ages of 717.1 +0.7/-0.9 Ma (95% confidence interval; *47*) and 717.61 ± 1.65 Ma (95% confidence interval; *48*). These estimates are consistent with onset between 717.4 ± 0.2 Ma and 716.9 ± 0.4 Ma based on constraints from the Mt. Harper Group. In comparing the maximum

constraint on onset (717.4 ± 0.2 Ma) and minimum age-bound on the younger, high-volume Type 2 magmas (14RAT-513A, 718.61 ± 0.30 Ma), Franklin LIP emplacement preceded the onset of glaciation by 1.21 ± 0.36 Myr (2σ uncertainties added in quadrature).

4. Initiation of Snowball Earth

Changes in weatherability and volcanic outgassing related to plate tectonics and paleogeography provide a first order control on Earth's long-term climate through the silicate weathering feedback (*50*). Snowball Earth represents a failure of this thermostat and is initiated once a critical threshold is reached for runaway ice-albedo feedback (*50*). The weathering of continental flood basalts in particular has been hypothesized as an important sink for CO_2 because of their large surface areas and highly reactive mafic lithologies (*51–53*). Furthermore, modern river data demonstrate that CO_2 consumption is highest in basaltic watersheds in the warm, wet tropics (*52, 54*). Models and proxy data for $p$$CO_2$ following LIP emplacement show that warming from the radiative effects of the initial input of CO_2 into the atmosphere can be counterbalanced by silicate weathering, with peaks of LIP-associated weatherability within ~1–2 Myr of emplacement (*2, 53, 55*), after which time the development of regolith and soil shielding will decrease weatherability (*54, 56*).

Despite the sink for CO_2 that LIPs provide on million-year timescales, many LIPs are not associated with glaciation. The Siberian Traps were comparable in size to the Franklin LIP and the preceding Mackenzie LIP may have been even larger, but neither resulted in a Snowball Earth episode. The lack of correlation between multimillion-year glacial events such as the Permo-Carboniferous glaciations and LIPs can be expected as a result of several factors, including the background climate state (e.g., *5*), the paleolatitude of the LIP (*55*), the

16

composition of the country rocks that the LIP is emplaced in (*2*), and even the paleogeography of the continents at the time of emplacement (e.g., *56*). The Siberian Traps and CAMP were emplaced during warm background climate conditions on an ice-free Earth (*5*, *57*), increasing the barrier to runaway glaciation. Weathering also proceeded slowly for the Siberian Traps due to its emplacement at high latitudes (*55*). The Mackenzie LIP was emplaced in an intracontinental setting in a subsiding basin (*18*, *58*), decreasing its topographic relief and weathering impact. In contrast to other LIPs, the emplacement of the Franklin LIP occurred in conjunction with several factors that increased global weatherability and allowed for runaway cooling on a 1–2 Myr timescale (*2*, *53*, *55*).

Paleogeography was likely an important factor contributing to increased weatherability and a cool Cryogenian climate due to an abundance of continents after supercontinent breakup (*8*, *56*, *59*), large igneous provinces with mafic lithologies (*6*, *53*), and arc terranes with high relief (e.g., *60–62*), all at low-latitudes in the equatorial rain belt (*63*). Additionally, it has been suggested that reduced continental volcanic arc activity during supercontinent breakup could have led to lower CO_2 outgassing (*64*), further decreasing global temperatures and the threshold for glaciation.

Critical to weatherability is the generation of topography (e.g., *55*, *61*, *62*); if a continental flood basalt province is emplaced at low relief, it will likely be buried and not significantly increase global weatherability, as happened with the burial of the CAMP during the rifting of the Atlantic. If, instead, a LIP is associated with uplift and exhumation and creates volcanic highlands, there is strong potential for a rapid increase in global weatherability (*53*, *55*). Studies of plume-head interactions with the lithosphere argue that as the plume head flattens due to impact with the lithosphere, early uplift at the plume axis is

followed by subsidence while the margins of the plume head, possibly out to distances of ~2000 km, should experience progressive uplift (*65*).

On Victoria Island, >500 km from the plume center, an unconformity below sub-areal basalt flows of the Natkusiak Formation has been interpreted to record the doming of the crust associated with the impingement of the Franklin LIP mantle plume (*31*), supporting the hypothesis that the Franklin LIP generated dynamic topography and created volcanic highlands rather than submerged lowlands associated with sedimentation and burial. The Natkusiak Formation exhibits prehnite-pumpellyite facies metamorphism attributed to an elevated geotherm and the presence of an overlying volcanic succession that was originally >2 km (*32*). The generation of topography due to emplacement of the Franklin LIP followed by its erosion is consistent with coupled Sr and Nd isotopes from carbonates and mudstones from the adjacent margins that document a Cryogenian flux of juvenile material (*7*).

At the southern edge of the study area, Douglas Peninsula sill sample F1966 gives Cryogenian (U-Th)/He zircon dates which alone do not require substantial exhumation immediately after Franklin LIP emplacement; both immediate exhumation from shallow emplacement and shallow burial to temperatures <150°C following emplacement are permissible (Fig. S5). However, the paucity of sedimentary Cryogenian to Ediacaran units across the wider study area lead us to conclude that the burial scenario is unlikely, and that broad volcanic highlands, much like modern Ethiopia, covered a significant area of tropical Laurentia (Fig. 2, S5).

Dynamic topography resulting from plume-head impact is expected to persist on the order of 10 Myr (*65*), and basaltic highlands associated with the Gunbarrel and Franklin LIPs would have contributed to high global weatherability at the Tonian-Cryogenian boundary

(e.g., *60, 62*). Coupled climate-weathering models predict that the removal of recent flood basalt provinces without any prescribed topographic change would change steady state pCO_2 by >100 ppm (*55*), demonstrating the potential for cooling associated with the weatherability of LIPs. Thus, the hypothesis that increased global weatherability associated with the tropical emplacement of the Franklin LIP contributed to the onset of the Sturtian snowball Earth predicts runaway ice-albedo feedback within ~1–2 Myr; this is consistent with the geochronology presented herein.

There have been multiple factors proposed for shorter-term changes of planetary albedo or radiative forcing that could have also pushed Earth's climate toward the threshold for a Snowball glaciation, including volcanic aerosols (*5*) or biogeochemical changes (e.g., *59, 66*). Albedo perturbations should initiate glaciation almost immediately because of the strong forcings but short residence times of aerosols (*5*), and biogeochemical changes would likely cause cooling on timescales of 10^3–10^4 years (*66*). The timeline presented herein is inconsistent with direct, short-term (<100 kyr) connections between peak magmatism of the Franklin LIP and the onset of the Sturtian glaciation.

The data presented provide the first high-precision ages on the main, high-volume phase of the Franklin LIP (Type 2 eruptions) between 719.08 ± 0.22 and 718.61 ± 0.30 Ma. Based on the approximate 10%-90% split between Type 1 and Type 2 rocks characterized in the Natkusiak Formation (*27*), the geochronology of the Type 2 phase is estimated to capture ≥90% of Franklin LIP magmatism. The best estimates on the onset of the Sturtian Snowball Earth glaciation suggest that it began ~0.9–1.6 Myr after peak Franklin LIP volcanism. Geology and thermochronology at the northern and southern edges of the study area, respectively, are compatible with post-emplacement exhumation corresponding to

development of Tonian-Cryogenian volcanic highlands in Cordilleran and Arctic Laurentia. The apparent lag time and generation of topography are consistent with an increase in global weatherability as a primary trigger for onset of glaciation. These results tighten the relationship between the largest Neoproterozoic episode of magmatism and one of the most extreme episodes of climate change in the geologic record.

D. Materials and Methods

Whole rock major element, trace element, and Sm-Nd isotope geochemistry were performed for all samples in addition to gabbro sample S8, the source of the most recent high-precision U-Pb baddeleyite date on the Franklin LIP (*4*). Major and trace element concentrations for samples FA700408 and F1966 were measured at California Institute of Technology following the procedure in (*67*). A Retsch planetary ball mill (PM 100) with agate grinding containers was used for powdering whole rock samples and a Claise Eagon 2 fluxer was used for fusing the powders into glass beads using lithium tetraborate as a flux. Major elements were measured on the glass beads using a 4 kW Zetium Panalytical X-ray fluorescence analyzer. Trace elements were measured using solution-ICPMS following the methods in (*68*).

The other six samples (93JP-71JB, 93JP-71M, 93JP-93L, S8, 14RAT-513A, 17RAT-R35B1) were powdered and analyzed at Hamilton College following the procedure in (*69*). Rocks were cut with a diamond saw and powdered in a SPEX 8530 ShatterBox® using an alumina ceramic dish at University of California, Santa Barbara (UCSB) and then re-powdered at Hamilton College using a Rocklabs alumina ring mill. The powders were doubly fused to homogenize the sample and then analyzed using a Thermo ARL Perform'X X-ray

fluorescence spectrometer. Trace elements were measured using LA-ICPMS on the fused glass beads following the procedures by (*70*).

Mineral separation for the U-Pb analyses was done at Harvard University and UCSB. Since most samples were only hand samples from archive, mineral separation procedures were tailored to maximize potential yield of zircon and baddeleyite grains. All samples were hand-sledged into chips that were ≤ 1 cm^3 and then pulsed in 1–2 s intervals in a SPEX 8530 ShatterBox® followed by sieving for the <500 μm fraction. The <500 μm fraction for each sample was handwashed in 5 L beakers to remove fine material and dried under heat lamps or in low-temperature ovens before being run on the Frantz magnetic separator. Highly magnetic minerals were initially screened for and removed using a hand magnet and then samples were typically run twice, first at 0.3 A and 20° tilt and the second time at 0.6 A and 20° tilt. If less than 2 oz. of sample were left after the first run on the Frantz, the sample was not run a second time. If the sample was mostly magnetic, the tilt angle was increased by 5–10° to ensure that no non-magnetic grains were carried by the flow of magnetic grains. Heavy liquid density separation using methylene iodide was the last step for isolating the dense mineral fraction of zircon and baddeleyite. Zircon and baddeleyite grains were hand-picked for each sample from this final fraction.

Geochronological analyses were done at Boise State University. Zircon crystals were mounted in epoxy, polished to expose grain cores, and imaged using a cathodoluminescence (CL) detector. U-Pb dates were obtained using the CA-ID-TIMS procedure developed by (*16*). Dissolution, spiking, and column chemistry procedures are described in more detail in the supplement. Baddeleyite geochronology followed the same procedure except grains were not subjected to chemical abrasion and were instead fluxed in 3.5 M HNO_3 for 20–30 min on a

21

hot plate and then sonicated for the same amount of time before being rinsed and loaded into microcapsules for dissolution with spike. Concordia and upper-intercept dates were plotted using IsoplotR (*71*).

Sm and Nd isotope geochemistry was done at the Isotope Geology Laboratory at Boise State University. Powdered samples were spiked and dissolved at 220°C for 18 hrs. Detailed column chemistry procedures are described in the supplement. Samples were analyzed on the IsotopX Phoenix X62 TIMS.

(U-Th)/He analysis was done at the Thermochronology Research and Instrumentation Lab at the University of Colorado Boulder following methods described in the supplement.

E. References

1. P. F. Hoffman, D. S. Abbot, Y. Ashkenazy, D. I. Benn, J. J. Brocks, P. A. Cohen, G. M. Cox, J. R. Creveling, Y. Donnadieu, D. H. Erwin, I. J. Fairchild, D. Ferreira, J. C. Goodman, G. P. Halverson, M. F. Jansen, G. Le Hir, G. D. Love, F. A. Macdonald, A. C. Maloof, C. A. Partin, G. Ramstein, B. E. J. Rose, C. V. Rose, P. M. Sadler, E. Tziperman, A. Voigt, S. G. Warren, Snowball Earth climate dynamics and Cryogenian geology-geobiology. *Sci. Adv.* **3**, 43 (2017).

2. M. T. Jones, D. A. Jerram, H. H. Svensen, C. Grove, The effects of large igneous provinces on the global carbon and sulphur cycles. *Palaeogeogr. Palaeoclimatol. Palaeoecol.* **441**, 4–21 (2015).

3. J. Kasbohm, B. Schoene, S. Burgess, "Radiometric Constraints on the Timing, Tempo, and Effects of Large Igneous Province Emplacement" in *Large Igneous Provinces: A Driver of Global Environmental and Biotic Changes*, R. E. Ernst, A. J. Dickson, A. Bekker, Eds. (Geophysical Monograph 255, AGU and Wiley, First Edit., 2021), pp. 27–82.

4. F. A. Macdonald, M. D. Schmitz, J. L. Crowley, C. F. Roots, D. S. Jones, A. C. Maloof, J. V. Strauss, P. A. Cohen, D. T. Johnston, D. P. Schrag, Calibrating the Cryogenian. *Science*. **327**, 1241–1243 (2010).

5. F. A. Macdonald, R. Wordsworth, Initiation of Snowball Earth with volcanic sulfur aerosol emissions. *Geophys. Res. Lett.* **44**, 1938–1946 (2017).

6. Y. Goddéris, Y. Donnadieu, A. Nédélec, B. Dupré, C. Dessert, A. Grard, G. Ramstein, L. M. François, The Sturtian "snowball" glaciation: Fire and ice. *Earth Planet. Sci.*

Lett. **211**, 1–12 (2003).

7.   G. M. Cox, G. P. Halverson, R. K. Stevenson, M. Vokaty, A. Poirier, M. Kunzmann, Z. X. Li, S. W. Denyszyn, J. V. Strauss, F. A. Macdonald, Continental flood basalt weathering as a trigger for Neoproterozoic Snowball Earth. *Earth Planet. Sci. Lett.* **446**, 89–99 (2016).

8.   Y. Donnadieu, Y. Goddéris, G. Ramstein, A. Nédélec, J. Meert, A "snowball Earth" climate triggered by continental break-up through changes in runoff. *Nature.* **428**, 303–306 (2004).

9.   W. F. Fahrig, E. Irving, G. D. Jackson, Paleomagnetism of the Franklin Diabases. *Can. J. Earth Sci.* **8**, 455–467 (1971).

10.   S. W. Denyszyn, H. C. Halls, D. W. Davis, D. A. D. Evans, Paleomagnetism and U-Pb geochronology of Franklin dykes in high arctic Canada and Greenland: A revised age and paleomagnetic pole constraining block rotations in the Nares Strait region. *Can. J. Earth Sci.* **46**, 689–705 (2009).

11.   L. M. Heaman, A. N. LeCheminant, R. H. Rainbird, Nature and timing of Franklin igneous events, Canada: Implications for a Late Proterozoic mantle plume and the break-up of Laurentia. *Earth Planet. Sci. Lett.* **109**, 117–131 (1992).

12.   S. J. Pehrsson, K. L. Buchan, Borden dykes of Baffin Island, Northwest Territories: A Franklin U-Pb baddeleyite age and a paleomagnetic reinterpretation. *Can. J. Earth Sci.* **36**, 65–73 (1999).

13.   S. W. Denyszyn, D. W. Davis, H. C. Halls, Paleomagnetism and U-Pb geochronology of the Clarence Head dykes, Arctic Canada: orthogonal emplacement of mafic dykes in a large igneous province. *Can. J. Earth Sci.* **46**, 155–167 (2009).

14.   F. A. Macdonald, M. D. Schmitz, J. V. Strauss, G. P. Halverson, T. M. Gibson, A. Eyster, G. Cox, P. Mamrol, J. L. Crowley, Cryogenian of Yukon. *Precambrian Res.* **319**, 114–143 (2017).

15.   S. E. Bryan, R. E. Ernst, Revised definition of Large Igneous Provinces (LIPs). *Earth-Science Rev.* **86**, 175–202 (2008).

16.   J. M. Mattinson, Zircon U-Pb chemical abrasion ("CA-TIMS") method: Combined annealing and multi-step partial dissolution analysis for improved precision and accuracy of zircon ages. *Chem. Geol.* **220**, 47–66 (2005).

17.   R. E. Ernst, D. P. G. Bond, S. Zhang, K. L. Buchan, S. E. Grasby, N. Youbi, H. El Bilali, A. Bekker, L. S. Doucet, "Large Igneous Province Record Through Time and Implications for Secular Environmental Changes and Geological Time-Scale Boundaries" in *Large Igneous Provinces: A Driver of Global Environmental and Biotic Changes,* R. E. Ernst, A. J. Dickson, A. Bekker, Eds. (Geophysical Monograph 255, AGU and Wiley, First Edit., 2021), pp. 1–26.

18.   A. N. LeCheminant, L. M. Heaman, Mackenzie igneous events, Canada: Middle Proterozoic hotspot magmatism associated with ocean opening. *Earth Planet. Sci. Lett.* **96**, 38–48 (1989).

19.   W. Bleeker, M. A. Hamilton, U. Söderlund, "A Franklin age (716 Ma) for a large

gabbro sill on Great Slave Lake, Northwest Territories, Canada" (Rep. No. A149, www.supercontinent.org, 2013).

20. R. E. Ernst, M. A. Hamilton, U. Söderlund, J. A. Hanes, D. P. Gladkochub, A. V. Okrugin, T. Kolotilina, A. S. Mekhonoshin, W. Bleeker, A. N. LeCheminant, K. L. Buchan, K. R. Chamberlain, A. N. Didenko, Long-lived connection between southern Siberia and northern Laurentia in the Proterozoic. *Nat. Geosci.* **9**, 464–469 (2016).

21. J. Ding, S. Zhang, D. A. D. Evans, T. Yang, H. Li, H. Wu, J. Chen, North China craton: The conjugate margin for northwestern Laurentia in Rodinia. *Geology*. **49**, 773–778 (2021).

22. S. S. Harlan, L. Heaman, A. N. LeCheminant, W. R. Premo, Gunbarrel mafic magmatic event: A key 780 Ma time marker for Rodinia plate reconstructions. *Geology*. **31**, 1053–1056 (2003).

23. W. Baragar, "The Natkusiak Basalts, Victoria Island, District of Franklin" (Paper 76-1A, Geol. Surv. Canada, 1976), pp. 347–352.

24. J. Dostal, W. R. A. Baragar, C. Dupuy, Petrogenesis of the Natkusiak continental basalts, Victoria Island, Northwest Territories, Canada. *Can. J. Earth Sci.* **23**, 622–632 (1986).

25. J. H. Bédard, B. Hayes, M. Hryciuk, C. Beard, N. Williamson, T. A. Dell'Oro, R. H. Rainbird, J. Prince, W. R. A. Baragar, P. Nabelek, D. Weis, B. Wing, J. S. Scoates, H. R. Naslund, B. Cousens, M.-C. Williamson, L. J. Hulbert, R. Montjoie, É. Girard, R. Ernst, C. J. Lissenberg, "Geochemical database of Franklin sills, Natkusiak Basalts and Shaler Supergroup rocks, Victoria Island, Northwest Territories, and correlatives from Nunavut and the mainland" (Open File Rep. 8009, Geol. Surv. Canada, 2016; 1 .zip file, doi:10.4095/297842).

26. N. M. B. Williamson, L. Ootes, R. H. Rainbird, J. H. Bédard, B. Cousens, Initiation and early evolution of the Franklin magmatic event preserved in the 720 Ma Natkusiak Formation, Victoria Island, Canadian Arctic. *Bull. Volcanol.* **78**, 1–19 (2016).

27. C. D. Beard, J. S. Scoates, D. Weis, J. H. Bédard, T. A. Dell'Oro, Geochemistry and origin of the Neoproterozoic Natkusiak flood basalts and related Franklin sills, Victoria Island, Arctic Canada. *J. Petrol.* **58**, 2191–2220 (2018).

28. G. M. Young, "The Amundsen Embayment, Northwest Territories; Relevance to the upper Proterozoic evolution of North America" in *Proterozoic Basins of Canada*, F. H. A. Campbell, Ed. (Geological Survey of Canada, 1981), Paper 81-10, pp. 203–218.

29. R. H. Rainbird, C. W. Jefferson, G. M. Young, The early Neoproterozoic sedimentary Succession B of northwestern Laurentia: Correlations and paleogeographic significance. *Bull. Geol. Soc. Am.* **108**, 454–470 (1996).

30. R. Thorsteinsson, E. T. Tozer, *Banks, Victoria, and Stefansson Islands, Arctic Archipelago* (Memoir 330, Geol. Surv. Canada, 1962), 85 p.

31. R. H. Rainbird, The sedimentary record of mantle plume uplift preceding eruption of the Neoproterozoic Natkusiak flood basalt. *J. Geol.* **101**, 305–318 (1993).

32. C. W. Jefferson, W. E. Nelson, R. V. Kirkham, J. H. Reedman, R. F. J. Scoates,

"Geology and copper occurrences of the Natkusiak basalts, Victoria Island, District of Franklin" in *Current Research, Part* A (Geol. Surv. Canada, 1985), Paper 85–1A, pp. 203–214.

33. A. M. Durbano, B. R. Pratt, T. Hadlari, K. Dewing, Sedimentology of an early Cambrian tide-dominated embayment: Quyuk formation, Victoria Island, Arctic Canada. *Sediment. Geol.* **320**, 1–18 (2015).

34. E. Burov, S. Cloetingh, Controls of mantle plumes and lithospheric folding on modes of intraplate continental tectonics: Differences and similarities. *Geophys. J. Int.* **178**, 1691–1722 (2009).

35. R. W. Carlson, Physical and chemical evidence on the cause and source characteristics of flood basalt volcanism. *Aust. J. Earth Sci.* **38**, 525–544 (1991).

36. T. A. Dell'Oro, "Sr-Nd-Hf-Pb isotope and trace element geochemistry of the Natkusiak Formation continental flood basalts of the Neoproterozoic Franklin large igneous province, Victoria Island, Canada," thesis, University of British Columbia, Vancouver, Canada (2012).

37. J. M. Mattinson, C. M. Graubard, D. L. Parkinson, W. C. McClelland, "U-Pb Reverse Discordance in Zircons: the Role of Fine-Scale Oscillatory Zoning and Sub-Micron Transport of Pb" in *Earth Processes: Reading the Isotopic Code* (Geophysical Monograph Series, AGU, 1996), vol. 95, pp. 355–370.

38. L. P. Black, P. D. Kinny, J. W. Sheraton, The difficulties of dating mafic dykes: an Antarctic example. *Contrib. to Mineral. Petrol.* **109**, 183–194 (1991).

39. M. Ibanez-Mejia, G. E. Gehrels, J. Ruiz, J. D. Vervoort, M. E. Eddy, C. Li, Small-volume baddeleyite (ZrO_2) U-Pb geochronology and Lu-Hf isotope geochemistry by LA-ICP-MS. Techniques and applications. *Chem. Geol.* **384**, 149–167 (2014).

40. L. M. Heaman, A. N. LeCheminant, Anomalous U-Pb systematics in mantle-derived baddeleyite xenocrysts from Île Bizard: Evidence for high temperature radon diffusion? *Chem. Geol.* **172**, 77–93 (2000).

41. M. Rioux, S. Bowring, F. Dudás, R. Hanson, Characterizing the U-Pb systematics of baddeleyite through chemical abrasion: Application of multi-step digestion methods to baddeleyite geochronology. *Contrib. to Mineral. Petrol.* **160**, 777–801 (2010).

42. P. S. Mustard, C. F. Roots, Rift-Related Volcanism, Sedimentation, and Tectonic Setting of the Mount Harper Group, Ogilvie Mountains, Yukon Territory. *Geol. Surv. Canada Bull.* **492**, 92 (1997).

43. J. A. Stevenson, J. L. Smellie, D. W. McGarvie, J. S. Gilbert, B. I. Cameron, Subglacial intermediate volcanism at Kerlingarfjöll, Iceland: Magma-water interactions beneath thick ice. *J. Volcanol. Geotherm. Res.* **185**, 337–351 (2009).

44. J. L. Smellie, Terrestrial subice volcanism: Landform morphology, sequence characteristics, environmental influences, and implications for candidate Mars examples. *Spec. Pap. Geol. Soc. Am.* **453**, 55–76 (2009).

45. Y. Donnadieu, F. Fluteau, G. Ramstein, C. Ritz, J. Besse, Is there a conflict between the Neoproterozoic glacial deposits and the snowball Earth interpretation: An improved

understanding with numerical modeling. *Earth Planet. Sci. Lett.* **208**, 101–112 (2003).

46. D. Pollard, J. F. Kasting, "Climate-Ice Sheet Simulations of Neoproterozoic Glaciation Before and After Collapse to Snowball Earth" in *The Extreme Proterozoic: Geology, Geochemistry, and Climate* (Geophysical Monograph Series, AGU, 2004), vol. 146, pp. 91–105.

47. S. MacLennan, Y. Park, N. Swanson-Hysell, A. Maloof, B. Schoene, M. Gebreslassie, E. Antilla, T. Tesema, M. Alene, B. Haileab, The arc of the Snowball: U-Pb dates constrain the Islay anomaly and the initiation of the Sturtian glaciation. *Geology.* **46**, 539–542 (2018).

48. Z. Lan, M. H. Huyskens, K. Lu, X. H. Li, G. Zhang, D. Lu, Q. Z. Yin, Toward refining the onset age of Sturtian glaciation in South China. *Precambrian Res.* **338**, 105555 (2020).

49. G. M. Cox, J. V. Strauss, G. P. Halverson, M. D. Schmitz, W. C. McClelland, R. S. Stevenson, F. A. Macdonald, Kikiktat volcanics of Arctic Alaska-Melting of harzburgitic mantle associated with the Franklin large igneous province. *Lithosphere.* **7**, 275–295 (2015).

50. J. C. G. Walker, P. B. Hays, J. F. Kasting, A negative feedback mechanism for the long-term stabilization of Earth's surface temperature. *J. Geophys. Res.* **86**, 9776–9782 (1981).

51. G. Li, J. Hartmann, L. A. Derry, A. J. West, C. F. You, X. Long, T. Zhan, L. Li, G. Li, W. Qiu, T. Li, L. Liu, Y. Chen, J. Ji, L. Zhao, J. Chen, Temperature dependence of basalt weathering. *Earth Planet. Sci. Lett.* **443**, 59–69 (2016).

52. C. Dessert, B. Dupré, J. Gaillardet, L. M. François, C. J. Allègre, Basalt weathering laws and the impact of basalt weathering on the global carbon cycle. *Chem. Geol.* **202**, 257–273 (2003).

53. C. Dessert, B. Dupré, L. M. François, J. Schott, J. Gaillardet, G. Chakrapani, S. Bajpai, Erosion of Deccan Traps determined by river geochemistry: Impact on the global climate and the 87Sr/86Sr ratio of seawater. *Earth Planet. Sci. Lett.* **188**, 459–474 (2001).

54. J. Hartmann, N. Moosdorf, R. Lauerwald, M. Hinderer, A. J. West, Global chemical weathering and associated P-release—The role of lithology, temperature and soil properties. *Chem. Geol.* **363**, 145–163 (2014).

55. Y. Park, N. L. Swanson-Hysell, L. E. Lisiecki, F. A. Macdonald, "Evaluating the Relationship Between the Area and Latitude of Large Igneous Provinces and Earth's Long-Term Climate State" in *Large Igneous Provinces: A Driver of Global Environmental and Biotic Changes*, R. E. Ernst, A. J. Dickson, A. Bekker, Eds. (Geophysical Monograph 255, AGU and Wiley, First Edit., 2021), pp. 153–168.

56. Y. Goddéris, G. Le Hir, M. Macouin, Y. Donnadieu, L. Hubert-Théou, G. Dera, M. Aretz, F. Fluteau, Z. X. Li, G. P. Halverson, Paleogeographic forcing of the strontium isotopic cycle in the Neoproterozoic. *Gondwana Res.* **42**, 151–162 (2017).

57. E. L. Taylor, T. N. Taylor, N. R. Cúneo, The Present Is Not the Key to the Past: A Polar

Forest from the Permian of Antarctica. *Science*. **257**, 1675–1677 (1992).

58. R. H. Rainbird, R. E. Ernst, The sedimentary record of mantle-plume uplift. *Geol. Soc. Am. Spec. Pap.* **352**, 227–245 (2001).

59. D. P. Schrag, R. A. Berner, P. F. Hoffman, G. P. Halverson, On the initiation of a snowball Earth. *Geochemistry, Geophys. Geosystems*. **3**, 1–21 (2002).

60. Y. Park, N. L. Swanson-Hysell, S. A. MacLennan, A. C. Maloof, M. Gebreslassie, M. M. Tremblay, B. Schoene, M. Alene, E. S. C. Anttila, T. Tesema, B. Haileab, The lead-up to the Sturtian Snowball Earth: Neoproterozoic chemostratigraphy time-calibrated by the Tambien Group of Ethiopia. *GSA Bull.* **132**, 1119–1149 (2019).

61. F. A. Macdonald, N. L. Swanson-Hysell, Y. Park, L. Lisiecki, O. Jagoutz, Arc-continent collisions in the tropics set Earth's climate state. *Science*. **364**, 181–184 (2019).

62. Y. Park, P. Maffre, Y. Goddéris, F. A. MacDonald, E. S. C. Anttila, N. L. Swanson-Hysell, Emergence of the Southeast Asian islands as a driver for Neogene cooling. *Proc. Natl. Acad. Sci. U. S. A.* **117**, 25319–25326 (2020).

63. Z. X. Li, D. A. D. Evans, G. P. Halverson, Neoproterozoic glaciations in a revised global palaeogeography from the breakup of Rodinia to the assembly of Gondwanaland. *Sediment. Geol.* **294**, 219–232 (2013).

64. N. R. McKenzie, B. K. Horton, S. E. Loomis, D. F. Stockli, N. J. Planavsky, C. T. A. Lee, Continental arc volcanism as the principal driver of icehouse-greenhouse variability. *Science*. **352**, 444–447 (2016).

65. A. M. Friedrich, H. P. Bunge, S. M. Rieger, L. Colli, S. Ghelichkhan, R. Nerlich, Stratigraphic framework for the plume mode of mantle convection and the analysis of interregional unconformities on geological maps. *Gondwana Res.* **53**, 159–188 (2018).

66. E. Tziperman, I. Halevy, D. T. Johnston, A. H. Knoll, D. P. Schrag, Biologically induced initiation of neoproterozoic snowball-earth events. *Proc. Natl. Acad. Sci.* **108**, 15091–15096 (2011).

67. C. E. Bucholz, C. J. Spencer, Strongly Peraluminous Granites across the Archean-Proterozoic Transition. *J. Petrol.* **60**, 1299–1348 (2019).

68. M. J. Lewis, C. E. Bucholz, O. E. Jagoutz, Evidence for polybaric fractional crystallization in a continental arc: Hidden Lakes mafic complex, Sierra Nevada batholith, California. *Contrib. to Mineral. Petrol.* **176**, 1–27 (2021).

69. D. M. Johnson, P. R. Hooper, R. M. Conrey, XRF Analysis of Rocks and Minerals for Major and Trace Elements on a Single Low Dilution Li-tetraborate Fused Bead: JCPDS-International Center for Diffraction Data. *Adv. X-Ray Anal.* **41**, 843–867 (1999).

70. R. M. Conrey, D. G. Bailey, J. W. Singer, L. Wagoner, B. Parfitt, J. Hay, O. Keh, "Combined Use of Multiple Internal and External Standards in LA-ICPMS Analysis of Geologic Samples Using Lithium Borate Fused Glass," poster presented at the AGU Fall Meeting, San Francisco, CA, 9 December 2019.

71. P. Vermeesch, IsoplotR: A free and open toolbox for geochronology. *Geosci. Front.* **9**, 1479–1493 (2018).

72. K. L. Buchan, R. Ernst, E, "Diabase dyke swarms of Nunavut, Northwest Territories and Yukon, Canada" (Open File 7464, Geol. Surv. Canada, 2013), doi:10.4095/293149.

73. J. C. Harrison, M. R. St-Onge, O. V Petrov, S. I. Strelnikov, B. G. Lopatin, F. H. Wilson, S. Tella, D. Paul, T. Lynds, S. P. Shokalsky, C. K. Hults, S. Bergman, H. F. Jepsen, A. Solli, "Geological map of the Arctic / Carte géologique de l'Arctique" (Map 2159A, Geol. Surv. Canada, 2011) scale 1:5 000 000.

74. L. J. Hulbert, R. H. Rainbird, C. W. Jefferson, P. Friske, "Map of Mafic and Ultramafic Bodies Related to the Franklin Magmatic Event, Minto Inlier, Victoria Island, NWT" (Open File 4928, Geol. Surv. Canada, 2005), scale 1:500 000.

75. J. Hiess, D. J. Condon, N. McLean, S. R. Noble, ^{238}U/^{235}U systematics in terrestrial uranium-bearing minerals. *Science*. **335**, 1610–1614 (2012).

76. M. R. St-Onge, D. Scott, J, N. Rayner, M. Sanborn-Barrie, D. R. Skipton, B. M. Saumur, N. Wodicka, O. M. Weller, "Archean and Paleoproterozoic cratonic rocks of Baffin Island" in *Geological synthesis of Baffin Island (Nunavut) and the Labrador-Baffin Seaway*, L. T. Dafoe and N. Bingham-Koslowski, Eds. (Bulletin 608, Geol. Surv. Canada, 2020), 29 p., https://doi.org/10.4095/321824.

77. D. J. Condon, B. Schoene, N. M. McLean, S. A. Bowring, R. R. Parrish, Metrology and traceability of U-Pb isotope dilution geochronology (EARTHTIME Tracer Calibration Part I). *Geochim. Cosmochim. Acta*. **164**, 464–480 (2015).

78. T. E. Krogh, A low-contamination method for hydrothermal decomposition of zircon and extraction of U and Pb for isotopic age determinations. *Geochim. Cosmochim. Acta*. **37**, 485–494 (1973).

79. M. D. Schmitz, B. Schoene, Derivation of isotope ratios, errors, and error correlations for U-Pb geochronology using ^{205}Pb-^{235}U-(^{233}U)-spiked isotope dilution thermal ionization mass spectrometric data. *Geochemistry, Geophys. Geosystems*. **8**, 1–20 (2007).

80. J. S. Stacey, J. D. Kramers, Approximation of terrestrial lead isotope evolution by a two-stage model. *Earth Planet. Sci. Lett.* **26**, 207–221 (1975).

81. C. Pin, J. S. Zalduegui, Sequential separation of light rare-earth elements, thorium and uranium by miniaturized extraction chromatography: Application to isotopic analyses of silicate rocks. *Anal. Chim. Acta*. **339**, 79–89 (1997).

82. R. M. Flowers, P. K. Zeitler, M. Danišík, P. W. Reiners, C. Gautheron, R. A. Ketcham, J. R. Metcalf, D. F. Stockli, E. Enkelmann, R. W. Brown, (U-Th)/He chronology: Part 1. Data, uncertainty, and reporting. *GSA Bull.* (2022).

83. R. M. Flowers, R. A. Ketcham, D. L. Shuster, K. A. Farley, Apatite (U-Th)/He thermochronometry using a radiation damage accumulation and annealing model. *Geochim. Cosmochim. Acta*. **73**, 2347–2365 (2009).

84. W. R. Guenthner, P. W. Reiners, R. A. Ketcham, L. Nasdala, G. Giester, Helium

diffusion in natural zircon: radiation damage, anisotropy, and the interpretation of zircon (U-TH)/He thermochronology. *Am. J. Sci.* **313**, 145–198 (2013).

85. A. K. Ault, R. M. Flowers, S. A. Bowring, Phanerozoic surface history of the Slave craton. *Tectonics*. **32**, 1066–1083 (2013).

86. C. P. Sturrock, R. M. Flowers, F. A. Macdonald, The Late Great Unconformity of the Central Canadian Shield. *Geochemistry, Geophys. Geosystems*. **22**, 1–22 (2021).

87. B. A. Peak, R. M. Flowers, F. A. Macdonald, J. M. Cottle, Zircon (U-Th)/He thermochronology reveals pre-Great Unconformity paleotopography in the Grand Canyon region, USA. *Geology*. **49**, 1462–1466 (2021).

88. R. A. Ketcham, C. Gautheron, L. Tassan-Got, Accounting for long alpha-particle stopping distances in (U-Th-Sm)/He geochronology: Refinement of the baseline case. *Geochim. Cosmochim. Acta*. **75**, 7779–7791 (2011).

89. R. A. Ketcham, Forward and inverse modeling of low-temperature thermochronometry data. *Rev. Mineral. Geochemistry*. **58**, 275–314 (2005).

90. R. M. Flowers, R. A. Ketcham, E. Enkelmann, C. Gautheron, P. W. Reiners, J. R. Metcalf, M. Danišík, D. F. Stockli, R. W. Brown, (U-Th)/He chronology: Part 2. Considerations for evaluating, integrating, and interpreting conventional individual aliquot data. *GSA Bull.* (2022).

91. U. Ginster, P. W. Reiners, L. Nasdala, C. Chanmuang N., Annealing kinetics of radiation damage in zircon. *Geochim. Cosmochim. Acta*. **249**, 225–246 (2019).

92. W. R. Guenthner, Implementation of an Alpha Damage Annealing Model for Zircon (U-Th)/He Thermochronology With Comparison to a Zircon Fission Track Annealing Model. *Geochemistry, Geophys. Geosystems*. **22** (2021), doi:10.1029/2019GC008757.

93. R. A. Ketcham, HeFTy Version 1.9.0 (2015).

94. P. F. Hoffman, "Geology and tectonics, East Arm of Great Slave Lake, Northwest Territories" (Map 1628A, Geol. Surv. Canada, 1988), sheet 1 of 2, scale 1:250000 and 1:500000.

95. S. Polteau, A. Mazzini, O. Galland, S. Planke, A. Malthe-Sørenssen, Saucer-shaped intrusions: Occurrences, emplacement and implications. *Earth Planet. Sci. Lett.* **266**, 195–204 (2008).

96. A. K. Ault, R. M. Flowers, S. A. Bowring, Phanerozoic burial and unroofing history of the western Slave craton and Wopmay orogen from apatite (U-Th)/He thermochronometry. *Earth Planet. Sci. Lett.* **284**, 1–11 (2009).

97. A. K. Ault, R. M. Flowers, S. A. Bowring, Synchroneity of cratonic burial phases and gaps in the kimberlite record: Episodic magmatism or preservational bias? *Earth Planet. Sci. Lett.* **410**, 97–104 (2015).

98. W. F. McDonough, S.-s. Sun, The composition of the Earth. *Chem. Geol.* **120**, 223–253 (1995).

99. S.-s. Sun, W. F. McDonough, Chemical and isotopic systematics of oceanic basalts: Implications for mantle composition and processes. *Geol. Soc. Spec. Publ.* **42**, 313–345

(1989).

100. A. H. Jaffey, K. F. Flynn, L. E. Glendenin, W. C. Bentley, A. M. Essling, Precision measurement of half-lives and specific activities of ^{235}U and ^{238}U. *Phys. Rev. C.* **4**, 1889–1906 (1971).

101. E. H. G. Cooperdock, R. A. Ketcham, D. F. Stockli, Resolving the effects of 2-D versus 3-D grain measurements on apatite (U-Th)/He age data and reproducibility. *Geochronology.* **1**, 17–41 (2019).

102. R. A. Wolf, K. A. Farley, D. M. Kass, Modeling of the temperature sensitivity of the apatite (U-Th)/He thermochronometer. *Chem. Geol.* **148**, 105–114 (1998).

103. P. Martin, HeCalc (0.4.1). *Zenodo*. (2022; https://doi.org/10.5281/zenodo.5672830).

F. Acknowledgments

G. Figures
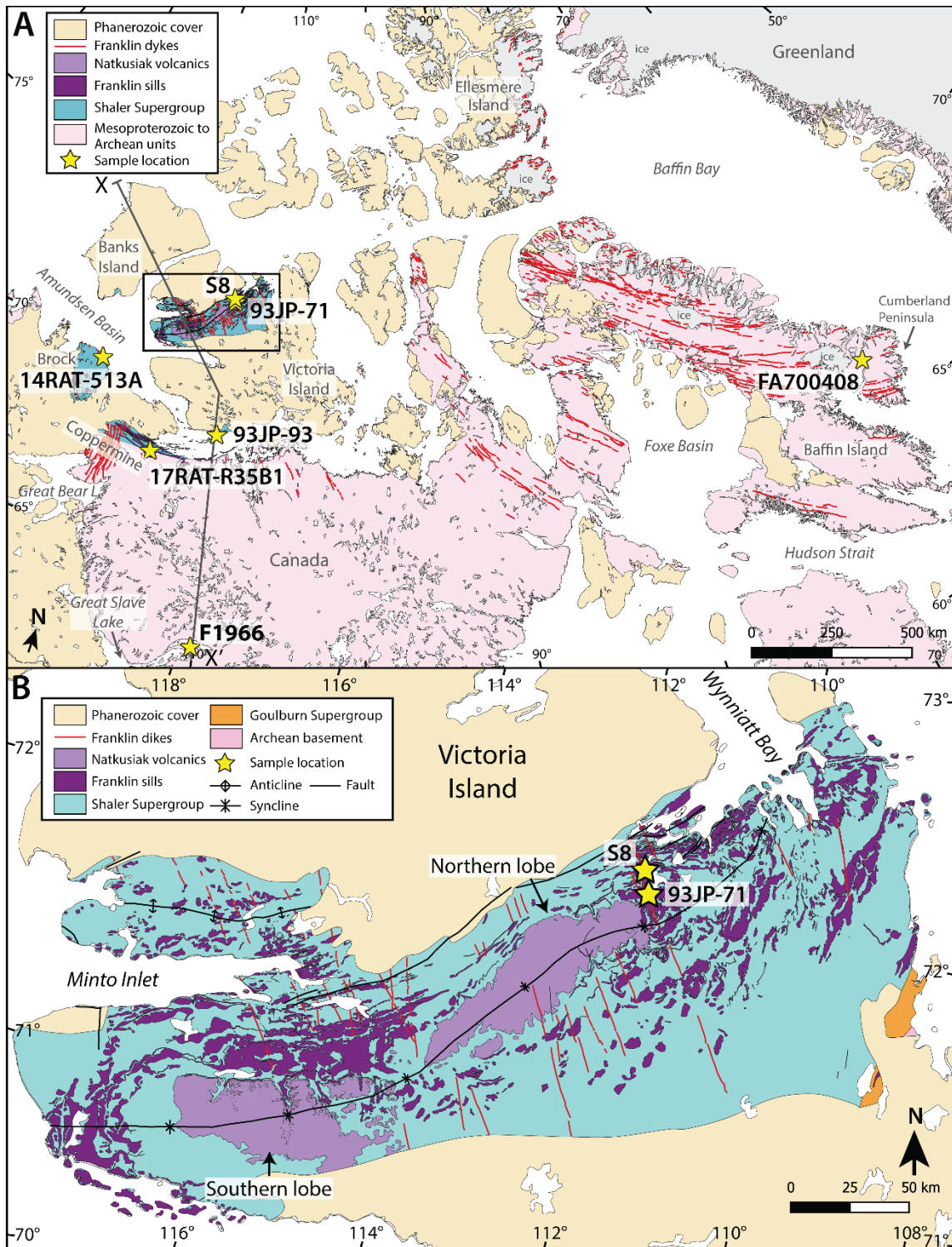
Fig. 1. Franklin LIP and sample map. Maps were modified from QGIS shape files from

(*72*), (*73*), and (*74*). A Canada polar stereographic projection based on WGS 1984 was used

(EPSG: 5937). **A.** Northern Canada geology highlighting the regional extent and location of rocks considered to be part of the Franklin LIP. The box on Victoria Island indicates the location of B. **B.** Detailed geology of the Minto Inlier on Victoria Island highlighting the location and distribution of Franklin LIP rocks and sample collection locations.
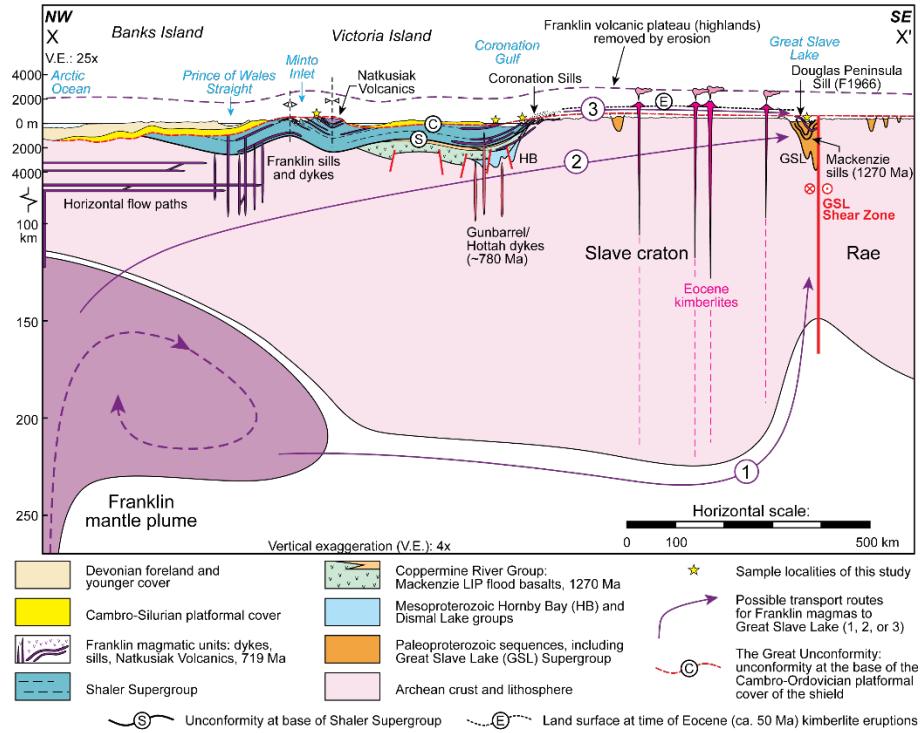
Fig. 2. Schematic cross-section of the Franklin LIP and starting plume head, and surrounding geological units. The section illustrates the emplacement of the Franklin LIP and three possible paths for sill emplacement in the Great Slave Lake area. Victoria Island sills and dykes may have similarly been emplaced via horizontal flow paths through the lithosphere. Location of cross-section X-X' is indicated in Fig. 1A. Dashed purple line depicts an estimate of the original Franklin LIP volcanic plateau thickness prior to erosion. Modern elevation on y-axis. Reconstructed paleosurfaces are positioned relative to the modern topography, and do not indicate absolute paleo-elevations at past times.

33
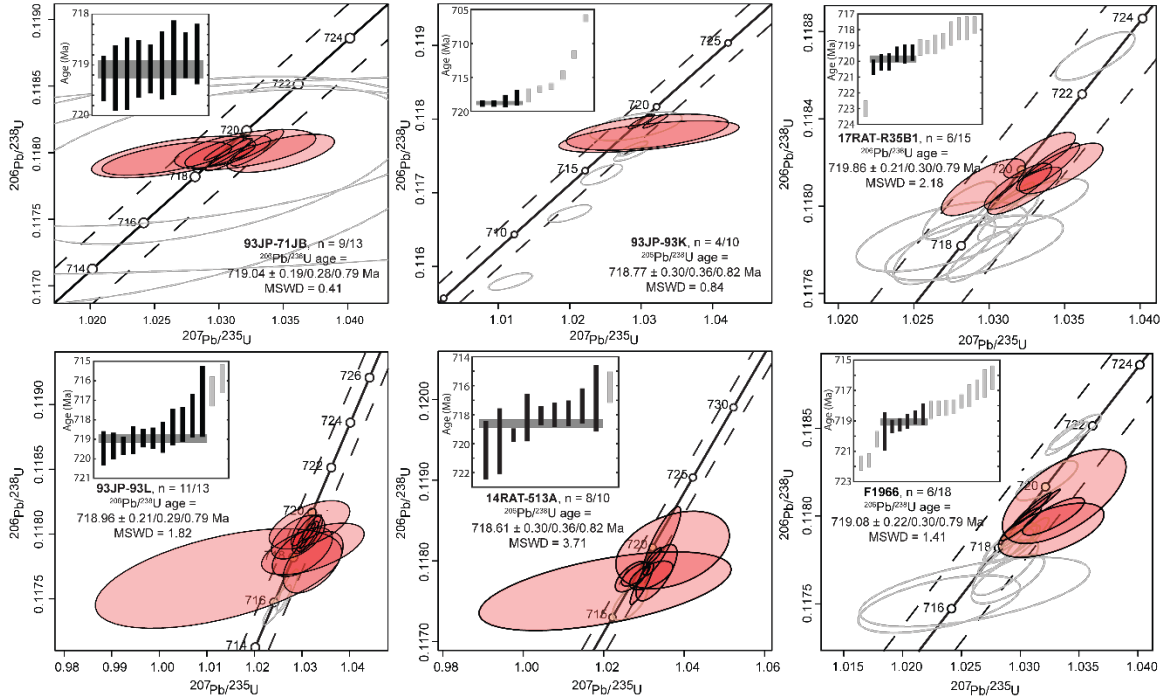
Fig. 3. Concordia plots for zircon analyses. Analyses are shown for samples 93JP-71JB, 93JP-93K, 17RAT-R35B1, F1966, 14RAT-513A, and 93JP-93L (clockwise from the top left). The baddeleyite analyses for samples S8 and FA700408 are included in the Supplemental Materials (Fig. S3). Concordia plots were modified from IsoplotR (*71*). Gray data ellipses are excluded from the weighted mean dates. All uncertainties are 2σ. Uncertainties for weighted mean dates in this study are reported as ± X/Y/Z, where X represents internal error only, Y includes tracer calibration uncertainties, and Z includes both tracer calibration and decay constant uncertainties for comparisons with different isotopic chronometers. Four low precision analyses are excluded from the plots for 93JP-71JB—the excluded data overlap the plotted analyses within uncertainty (Fig. 4A).

34
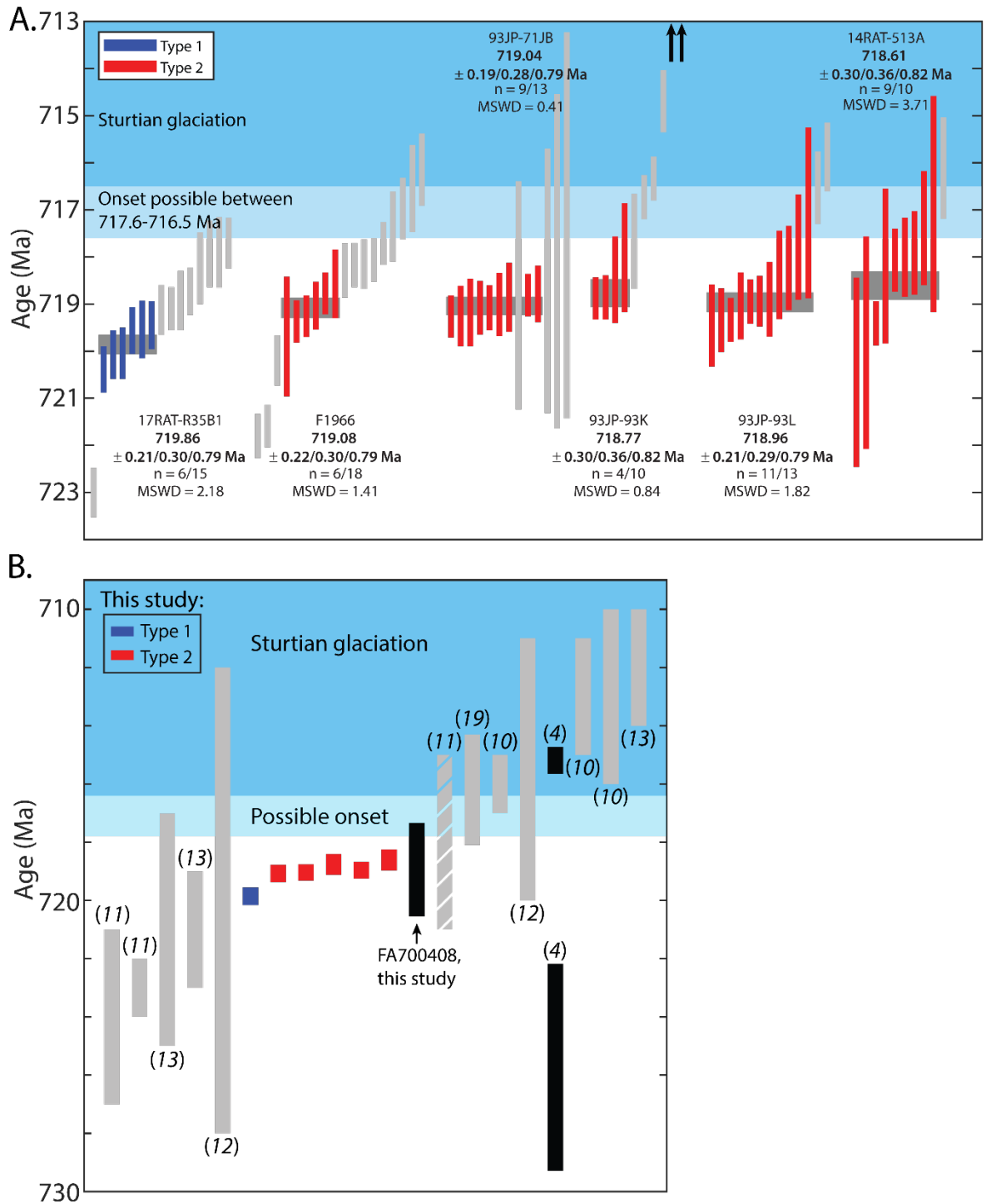
Fig. 4. Geochronology of the Franklin LIP. A. Ranked plots of the zircon ^{206}Pb/^{238}U dates for this study. Uncertainties presented are internal errors only (2σ). Gray data points are excluded from the weighted mean dates. Up arrows for sample 93JP-93K indicate analyses

35

with Pb-loss that plot younger than 713 Ma. **B.** Previous geochronology on the Franklin LIP yielded weighted mean or upper-intercept dates that range from 750–710 Ma; analyses from 735–710 Ma are plotted (*4, 10–13*, *19*). Previous upper-intercept dates were recalculated with the updated $^{238}U/^{235}U$ ratio for terrestrial zircon of 137.818 (*75*) using IsoplotR (*71*). Neoproterozoic $^{206}Pb/^{238}U$ dates would not change within uncertainty and were not recalculated from their original references. Details for the dates can be found in the Supplementary Materials (Table S4). Light grey coloration indicates either single or bulk baddeleyite analyses; the single diagonally striped sample (*11*) included both bulk zircon and bulk baddeleyite analyses. Black filled rectangles indicate results for S8 and FA700408, both consisting of single-grain baddeleyite analyses. The two rectangles for S8 show the older upper-intercept and younger $^{206}Pb/^{238}U$ dates calculated from single-grain baddeleyite analyses in (*4*), while the rectangle shown for FA700408 is the calculated upper-intercept date (95% CI shown). Other results from this study are red or blue, indicating Franklin LIP magma type, and follow the same sample order as in **A**. The 2σ uncertainties include internal and tracer calibration errors for interlaboratory comparison. The light blue bar across the plot represents the most precise age constraints on the onset of the Sturtian glaciation between 717.4 ± 0.4 Ma and 716.9 ± 0.5 Ma (including tracer calibration errors; *14*).
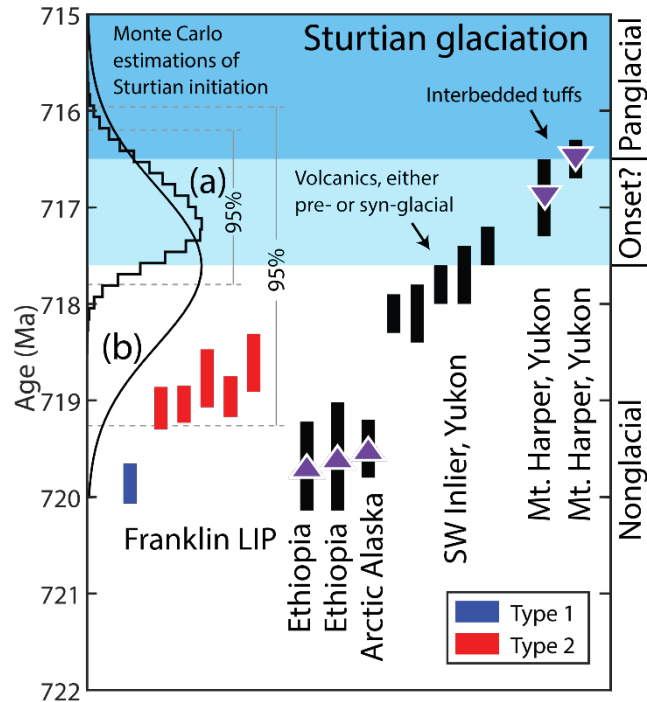
Fig. 5. Stratigraphic constraints on the onset of the Sturtian glaciation. Franklin LIP data from this study compared to existing constraints on the onset of the Sturtian glaciation (*14*, *47*, *48*, *76*). Since all analyses used the same technique and same isotopic tracer, only internal uncertainties were plotted for comparison. Purple arrows pointing up indicate dates that provide maximum constraints on the age of onset (i.e., glaciation onset must have occurred at a younger date) and arrows pointing down indicate minimum age constraints on onset. The ages of volcanic tuffs interbedded with glacial diamictite provide a definitive age by which glaciation must have been initiated. The maximum age bound on onset is still uncertain; the shown analyses bracketing onset are from volcanic sequences that could be subaerial or subglacial, with the possibility of onset being up to several 100 kyr before. Previous studies have used Monte Carlo models to estimate onset ages of (a) 717.1 +0.7/-0.9 Ma (*47*) and (b) 717.61 ± 1.65 Ma (*48*).

II. Tonian basins record rifting of Kalahari from Rodinia and no evidence of a Kaigas glaciation

A. Introduction

Three global climate states emerge from energy balance models: an ice-free state, a climate with high-latitude ice like today, and a Snowball state in which the Earth is entombed in ice (Hoffman, 2009; Ferreira et al., 2011). At least twice during the Cryogenian Period of the Neoproterozoic Era, ice extended to the equator, consistent with Earth entering a Snowball state. The Snowball Earth hypothesis predicts that glaciation associated with this climate state should be global in extent, begin synchronously, last millions of years, and end synchronously (Hoffman and Schrag, 2002), which has been borne out by geochronology studies (Rooney et al., 2015).

A ca. 750 Ma, pre-Sturtian glaciation, referred to as the Kaigas glaciation, has also been proposed (Frimmel et al., 1996a; Key et al., 2001; Xu et al., 2009), and used to argue that the Neoproterozoic glaciations were Quaternary-like with a number of ice-advances separated by inter-glacial periods (Allen and Etienne, 2008). Proposed pre-Sturtian glacial deposits include the Kaigas Formation (Fm) of the Gariep belt on the Kalahari craton (Von Veh, 1988; Frimmel et al., 1996a; Frimmel, 2008), the Bayisi diamictite on the Tarim craton (Xu et al., 2009), the Grand Conglomerate from the Kundelungu Basin of the Congo craton (Key et al., 2001), and the Konnarock Fm in the southern Appalachians of Laurentia (MacLennan et al., 2020). However, Rooney et al. (2015) demonstrated that the Grand Conglomerate of the Congo was instead <727 Ma, consistent with a Sturtian age, and that ca. 750 Ma strata were deposited on

western Laurentia without direct evidence of glaciation. Non-glacial strata were also deposited at this time in the Arabian-Nubian Shield (Park et al., 2020), which together with the Laurentia data preclude the occurrence of a global, low-latitude glaciation ca. 750 Ma. Additionally, no definitive evidence for Tonian glacial sedimentation has been demonstrated on the Tarim block given that the poorly-sorted conglomerates of the Bayisi diamictite formed in a volcanic rift (Xu et al., 2009). The interpretation of a 740 ± 7 Ma U-Pb age using a sensitive high-resolution ion microprobe (SHRIMP) on zircon in the Bayisi diamictite is complicated by possible inheritance from underlying ca. 750 Ma volcanic rocks (Xu et al., 2009). The remaining evidence for a low-latitude Tonian glaciation relies on studies from the Kalahari craton (Hofmann et al., 2015; Frimmel, 2018; Gaschnig et al., 2022; Zieger-Hofmann et al., 2022) and eastern Laurentia (MacLennan et al., 2020). Constraining the age and extent of these Tonian deposits is important not only for establishing a chronology for glaciations, but also for understanding the stability of climate states and the background climate during initiation of Snowball Earth. Did the Sturtian Snowball Earth follow a period of high-latitude ice and significant ice advances, or did the start of the Sturtian mark a more abrupt change in climate state from an ice-free period?

B. Geological background

Neoproterozoic strata are preserved in the Gariep Belt in N-S trending exposures straddling the Orange River along the border between Namibia and South Africa (Fig. 1; e.g., Frimmel, 2008; Macdonald et al., 2010). The Gariep Belt can be split into two parts: the autochthonous and parautochthonous Port Nolloth Group and the allochthonous, oceanic

Marmora Terrane west of the Schakalsberge Thrust (Kröner, 1975; Von Veh, 1988; Jasper et al., 1992). The Port Nolloth Group consists of a Neoproterozoic terrestrial to marginal marine sedimentary succession deposited on Namaquan basement and intercalated with rift-related, bimodal volcanic rocks (Frimmel et al., 1996a). Rift-related magmatism continued through 751.9 ± 5.5 Ma (Borg et al., 2003), before Cryogenian to early Ediacaran passive margin deposition (Macdonald et al., 2010). The passive margin deposits of the Port Nolloth Group are followed by foreland basin deposits of the Nama Group, which, near its base, has a syn-depositional U-Pb CA-ID-TIMS age constraint of 547.36 ± 0.91 Ma (Grotzinger et al., 1995; Bowring et al., 2007).

The Gariep Belt was deformed from the Ediacaran to Cambrian (Von Veh, 1988; Jasper et al., 1994) with prominent N-S to NW-SE striking folds and thrust faults dipping to the W or WSW (Fig. 1). These thrust faults reactivated and inverted Tonian to Cryogenian normal faults that had originally created accommodation space in the basin (Jasper et al., 1994, 2000).

From oldest to youngest, the Port Nolloth Group consists of the Stinkfontein Subgroup (including the Kaigas Fm), Hilda Subgroup, Numees Fm, and Holgat Fm (Fig. 2; Von Veh, 1988; Jasper et al., 1992; Frimmel, 2008; Macdonald et al., 2010). The basal Stinkfontein Subgroup is divided into conglomerates and sandstones of the Lekkersing and Vredefontein formations (Von Veh, 1988; Frimmel, 2008). The Stinkfontein Subgroup is intruded by the 793 +1.7/-1.5 Ma Gannakouriep dikes (Rioux et al., 2010), providing a minimum age constraint on the deposition of the Port Nolloth Group.

At the type locality in the Richtersveld of South Africa, the Kaigas Fm conformably and gradationally overlies quartzite of the Stinkfontein Subgroup (Kröner, 1975; Von Veh, 1988). Elsewhere, this contact has been portrayed as unconformable (Frimmel, 2018), but this could be due to miscorrelation with the Numees Fm (*cf.* Jasper et al., 2000; Macdonald et al., 2010; Zieger-Hofmann et al., 2022). The Kaigas Fm generally consists of laterally discontinuous conglomerate and sedimentary breccia with subangular to subrounded clasts composed dominantly of local basement. It includes graded beds of coarse-grained arenite and pelite, which have been interpreted as turbidites (Von Veh, 1988). The Kaigas Fm was considered a unit in the Stinkfontein Subgroup by Kröner (1975) and Von Veh (1988), but it was subsequently moved to the Hilda Subgroup by Frimmel (2008, 2018). Our observations of the Kaigas Fm on farm Trekpoort 96 are consistent with the earlier descriptions of its discontinuous nature (e.g., Jasper et al., 2000), and we have chosen to follow the original position of the Kaigas Fm as a formation within the Stinkfontein Subgroup (Fig. 2).

Carbonate strata mark the base of the overlying Picklehaube Fm of the Hilda Subgroup (Von Veh, 1988). The Picklehaube Fm consists of laminated carbonate interbedded with pelite and feldspathic quartz arenite (Frimmel, 2008). In deeper-water sections, the Picklehaube Fm consists of >200 m of carbonate (Von Veh, 1988; Macdonald et al., 2010). The Picklehaube Fm interfingers with and is overlain by volcanic and volcaniclastic rocks of the Rosh Pinah Fm (Alchin et al., 2005; Frimmel, 2008, 2018). The inferred volcanic center is on farm Spitzkop 111 where rhyolites and volcaniclastic units form the Spitzkop Suite (Frimmel et al., 1996b; Alchin et al., 2005). The Rosh Pinah Fm also includes planar-laminated allodapic limestone and mudstone, platform carbonates, breccias, and olistostromes (Alchin et al., 2005;

Frimmel, 2008). The Rosh Pinah Fm culminates in >100 m of graded sandstone and pelite, which also have been mapped as the Wallekraal Fm (Alchin et al., 2005; Frimmel, 2018). Age constraints on the Rosh Pinah Fm include a SHRIMP U-Pb zircon age of 751.9 ± 5.5 Ma from a felsic volcanic rock by the Skorpion Mine (Borg et al., 2003) and a Pb-Pb zircon evaporation age of ~742 Ma from an isolated outcrop (Frimmel et al., 1996b). Stratigraphic context for these ages is lacking.

The Picklehaube and Rosh Pinah formations of the Hilda Subgroup are succeeded by the overlying Numees Fm, a glaciogenic diamictite with banded iron formation (Jakkalsberg Member). The transgression above the Numees starts with the Bloeddrif Member, the Sturtian cap limestone, and deeper-water clastic units and carbonate of the lower Holgat Fm (Von Veh, 1988; Macdonald et al., 2010; Frimmel, 2018). These are overlain by the Marinoan-age Namaskluft diamictite and the 635 Ma Dreigratberg cap dolostone of the upper Holgat Fm (Macdonald et al., 2010). Previous workers have included the Dabie River and Wallekraal formations in the stratigraphy of the Port Nolloth Group, but these formations have been variably assigned to both the Hilda Subgroup and the Holgat Fm and have lost their stratigraphic utility (*cf*. Von Veh, 1988; Macdonald et al., 2010; Frimmel, 2018; Zieger-Hofmann et al., 2022). We do not refer to them herein.

Below, we describe stratigraphy, map relationships, and geochronology at farm Trekpoort 96 (Fig. 1B), which is located between Skorpion mine, the location of previous age constraints for the Kaigas Fm (Frimmel et al., 1996b; Borg et al., 2003), and the volcanic center at Spitzkop 111 (Alchin et al., 2005). We also report stratigraphy, map relationships, and geochronology from exposures along the Orange River (Fig. 1B), where glacial deposits have

been associated with a putative Tonian Kaigas glaciation (e.g., Frimmel, 2008; Zieger-Hofmann et al., 2022).

C. Methods

Field work was conducted in 2017 and 2018. Geologic maps were created by drafting on paper maps (1:7540 scale) and by mapping at variable scales using the FieldMove mapping application on an iPad. Stratigraphic sections were measured using a folding meter stick. In places where units are truncated or fault repeated, multiple shorter sections were measured to piece together composite sections. Samples for U-Pb geochronological analyses were collected while measuring stratigraphic sections. Coordinates for sample locations and sample lithologies are listed in Table S1.

Zircon grains were annealed at 900°C before being mounted in epoxy, polished, and imaged by cathodoluminescence (CL) to observe zircon zoning with the goal of identifying xenocrystic or metamict grains. They were then analyzed for U and Pb isotopes by laser ablation split stream (LASS) analyses using a Nu Instruments multi-collector inductively coupled plasma mass spectrometer (MC-ICPMS) and Agilent 7700X quadrupole ICPMS at UC Santa Barbara, following the procedures in Kylander-Clark et al. (2013) and Kylander-Clark (2017). Data were reduced using iolite4 software (Paton et al., 2010, 2011) and IsoplotR (Vermeesch, 2018). Standard error was propagated using methods described in Paton et al. (2010) and Horstwood et al. (2016). To compare data between analytical sessions and different U-Pb techniques, long-term excess variance (2% 2σ on $^{206}Pb/^{238}U$ ratios) was included in the error calculations on each ratio and also applied to weighted mean ratios to

propagate the uncertainty on the date (see Horstwood et al., 2016). These errors incorporating systematic uncertainties are reported using an "s" instead of σ to indicate the added dispersion.

A subset of the grains from samples ES1772-8 and ES1772-52 analyzed using LASS were selected for chemical abrasion-isotope dilution-thermal ionization mass spectrometry (CA-ID-TIMS) analyses at the MIT Isotope Laboratory, following the procedures outlined in Ramezani et al. (2022).

Detailed analytical methods for LASS and CA-ID-TIMS analyses are available in the Supplementary Materials. Complete Pb and U isotopic data are given in tables S2 and S3. Uncertainties on the weighted mean dates are given as 2σ and in the ± X/Y/Z Ma format, where X is the internal error based on analytical uncertainties only, Y includes X and the tracer calibration uncertainty, and Z includes Y plus the ^{238}U decay constant uncertainty of Jaffey et al. (1971). Y should be considered when comparing U-Pb dates with those obtained by different analytical methods or ID-TIMS dates using different isotopic tracers.

D. Results

1. Stratigraphy of the Trekpoort Syncline

Section JP1801 on farm Trekpoort 96 is the most complete section from the upper Stinkfontein Subgroup to the lowermost Numees Fm and represents the general stratigraphy in the area (Fig. 3). The unit descriptions below refer to the lithologic and stratigraphic changes recorded in this section but also incorporate observed facies changes from correlative units in other lateral sections.

1.1 Stinkfontein Group/Kaigas Formation

The Stinkfontein Subgroup locally onlaps basement with conglomerate but is in fault contact with the basement along much of the outcrop belt (Fig. 1, detailed map in Fig. 3). The lower Stinkfontein consists of medium- to coarse-grained quartz sandstone with <5-20% metamorphic mica. Within 20 m of the base, there are lenses of arkose and conglomerate with subrounded to rounded, cm-scale granitic pebbles. Decimeter- to meter-scale trough and tabular cross-stratification is common (Fig. 4A). These coarse-grained units fine up-section into thin interbeds of recrystallized carbonate beds and fine-grained green and white sandstone, with the dark green coloration due to increased mica content (i.e., biotite and chlorite).

To the northwest, in sections F1811, F1810, and F1814, weakly-bedded basement clast-supported sedimentary breccia of the Kaigas Fm is preserved as growth strata against basement. These relationships are preserved in slivers where a Tonian syn-sedimentary normal fault was inverted by multiple strands of a Cambrian thrust fault zone (Fig. 3). Southwest of the faults, section F1814 consists of channelized arkosic sandstone and conglomerate with meter-scale tabular and trough cross-beds. A second syn-sedimentary fault is preserved along a basement high between section F1811 and F1810. In these sections, conglomerate and sedimentary breccias consisting of basement clasts dominate the lower 10s of meters of the section (Fig. 4B), which are succeeded by arkosic sandstone and minor carbonate.

1.2. Picklehaube and Rosh Pinah formations

A road passes between the Kaigas and overlying Picklehaube and Rosh Pinah formations of the Hilda Subgroup on Trekpoort 96 and the contact is covered by ~150 m

of non-exposure in section JP1801. Above the cover, the lowest units consist of interbedded recrystallized carbonate and green phyllite. This strata is succeeded by planar bedded fine- to medium-grained sandstone with minor cross-bedding and interbedded dolomite and calcisiltite. Blue recrystallized dolomite with bands of dark brown silicification serve as marker beds and locally preserve microbial laminations and rip-up clasts. These sandstone and calcisiltite interbeds continue upwards in the stratigraphy for ~150 m before the first conglomerate beds with boulder clasts appear. The conglomerates are poorly sorted, clast-supported deposits with grain size ranging from very fine gravel to cobbles and boulders. The clasts are all granitic in composition in the first gravel bed, but subsequent gravel beds contain a variety of clast compositions including granite, quartzite, siltstone, and carbonate. The conglomerates have poorly-defined bedding but locally contain fining-up sequences. At ~450 m above the base of the section, m-scale normal grading becomes well-defined with conglomerate and coarse-grained sandstone beds fining upward to grey shale beds.

Above the first shale beds, the Rosh Pinah Fm includes fine-grained, porphyritic meta-rhyolite flows with quartz and alkali feldspar phenocrysts (Frimmel et al., 1996b), which were collected for U-Pb zircon geochronology (ES1772-8, ES1772-52; Fig. 3). The rhyolites host K-feldspar phenocrysts rimmed by biotite porphyroblasts. Up-section from the rhyolite flows, carbonate beds decrease in frequency and are succeeded by finer-grained siliciclastic, downslope facies.

1.3. Numees Formation

On farm Trekpoort 96, the base of the Numees Fm is gradational and begins with lonestones in a siltstone to sandstone matrix (Fig. 4C). The background sedimentation coarsens just below the appearance of dropstones and includes well-sorted, fine- to medium-grained quartz-arenite beds that transition into a stratified diamictite. The lower stratified diamictite is ~60 m thick with pebble- to cobble-sized granite and carbonate clasts. The stratified diamictite is interbedded with well-laminated siltstone and shale and fine- to medium-grained sandstone with both planar lamination and cross-stratification. The stratified diamictites are interbedded with, and succeeded by, tens of meters of graded beds of conglomerate with irregular bases that fine upward to sandstone. These are succeeded by meter-thick beds of massive diamictite that are poorly sorted and clast-rich, with granite and carbonate clasts. The Numees Fm is the uppermost unit exposed in the core of the Trekpoort syncline.

2. Spitzkop Suite

Rhyolites in the Rosh Pinah Fm have been correlated with the Spitzkop Suite exposed on farm Spitzkop 111 (Alchin et al., 2005). At Spitzkop 111, the volcanics consist of massive to flow-banded quartz-alkali feldspar meta-rhyolites to rhyodacites and locally reworked lapilli tuff breccias (Frimmel et al., 1996b). A sample of the quartz-feldspar rhyolite was collected for U-Pb zircon geochronology (sample JP1710; Fig. 3). The volcaniclastics include tuffaceous siltstones and sandstones that have been metamorphosed to biotite-chlorite-sericite schists with minor calcite and clinozoisite (Frimmel et al., 1996b; Frimmel, 2008). The tuffaceous units preserve sanidine phenocrysts and subrounded to rounded detrital quartz and

feldspar grains, suggesting reworking (Frimmel et al., 1996b; Alchin et al., 2005; Frimmel, 2018).

3. Stratigraphy along the Orange River

The Port Nolloth Group stratigraphy and map relationships along the Orange River are central to previous interpretations of a glacial origin for the Kaigas Fm and to the interpretations of this study. Von Veh (1988) and Frimmel (2018) mapped the southeasternmost diamictite exposure (Fig. 5) as the Kaigas Fm and extended these units south of the Orange River. In contrast, Macdonald et al. (2010) mapped all of these exposures as the Numees Fm with lithofacies differences between outcrops due to lateral facies changes. More recently, Zieger-Hofmann et al. (2022) suggested that all exposures of the Kaigas Fm south of the Orange River are Numees Fm, but that the diamictite along the Orange River on the Namibian side of the border is part of the Kaigas Fm. A complication and difficulty in interpreting the stratigraphic affinity of these outcrops is that they are situated along the southern extension of the Rosh Pinah thrust fault, which marks the boundary between the autochthon and parautochthon (Fig 1; Jasper et al., 1994, 2000).

Detailed mapping and logging of stratigraphic sections along the Orange River clarify the structural and stratigraphic relationships of what was previously interpreted as the Kaigas Fm by Von Veh (1988) and followed by others (Frimmel, 2018; Zieger-Hofmann et al., 2022). Depositional contacts between diamictite on basement are exposed on the eastern margin of the belt, where isoclinally folded diamictite is overlain by the Sturtian Bloeddriff cap carbonate (Fig. 5, zoomed-in map). The Bloeddriff Member is structurally below exposures

of the Hilda Subgroup along a major thrust fault that can be followed north into the Rosh Pinah thrust, which places the Hilda Subgroup and Numees Fm structurally above the Nama Group (Fig. 5). These structural relationships demonstrate that the diamictite along the Orange River is to the east of the Rosh Pinah thrust fault and is attached to the autochthon. This diamictite and overlying Bloeddriff Member can be traced north where they are overlain by the Namaskluft diamictite, Dreigratberg cap carbonate, upper Holgat Fm, and sandstone of the Dabis Fm of the Nama Group (Fig. 1). The stratigraphic implication of these mapping results confirms the previous interpretation of Macdonald et al. (2010) that the easternmost diamictite exposures adjacent to basement should be interpreted as the Sturtian Numees Fm rather than the Kaigas Fm.

The units overlying the lower diamictites in both the eastern belt and at Dreigratberg were previously mapped as part of the Picklehaube Fm (Von Veh, 1988; Frimmel, 2018). However, there are additional glacial diamictites in these belts that are overlain by distinctive marker beds with tubestone stromatolites and sheet-crack cements at their base that were assigned to the ca. 635 Ma Dreigratberg cap carbonate (Fig. 5; Macdonald et al., 2010). In the northeast exposure of the Orange River map area (Fig. 5), sections F819, F820, JP1803, JP1804, and JP1805 capture the stratigraphic transition from basement to the Bloeddrif Member through the Cryogenian portion of the Holgat Fm and end with the basal Ediacaran Dreigratberg cap dolostone. In the southwestern exposure of the Orange River map area by Dreigratberg, sections F816, F912, and JP1806 are measured through the Namaskluft diamictite (Fig. 5); here, it is 1-25 m thick, clast-poor diamictite with a medium to coarse-grained sandstone matrix and contains pebble- to cobble-sized clasts of dolostone and granite.

At both localities, the Dreigratberg cap carbonate and upper Holgat Fm are overlain by sandstone of the Dabis Fm of the Nama Group.

4. U-Pb LASS and CA-ID-TIMS geochronology

Samples ES1772-8 and ES1772-52 were collected from rhyolite units in the Rosh Pinah Fm within a measured section (ES1772) on Trekpoort 96 (Fig. 3) and analyzed by LASS (Fig. 6A and 6B). Analyses that were more than 10% discordant between their $^{207}Pb/^{206}Pb$ and $^{206}Pb/^{238}U$ dates were excluded from weighted mean calculations for LASS. Additional outliers were excluded using Chauvenet's criterion in IsoplotR (Vermeesch, 2018). LASS analyses of sample ES1772-52 produced a $^{206}Pb/^{238}U$ weighted mean date of 740 ± 14 Ma (2s, n = 105/110) and ES1772-8 produced a $^{206}Pb/^{238}U$ weighted mean date of 744 ± 14 Ma (2s, n = 112/116). The two samples were then analyzed using CA-ID-TIMS for higher precision. Nine grains were analyzed from sample ES1772-52 and ranged in $^{206}Pb/^{238}U$ dates from 753.08 ± 0.76 Ma to 748.3 ± 1.6 Ma (Fig. 6A). Two analyses had much larger uncertainties due to their low U contents (<30 pg) and were excluded from weighted mean date calculations. The youngest group of remaining analyses with an MSWD consistent with a single population produced a weighted mean $^{206}Pb/^{238}U$ date of $751.82 \pm 0.32/0.46/0.93$ Ma (2σ, n = 5/9, MSWD = 1.7). Six grains were analyzed from sample ES1772-8 and produced a weighted mean $^{206}Pb/^{238}U$ date of $752.38 \pm 0.26/0.41/0.90$ Ma (2σ uncertainty, MSWD = 1.2; Fig. 6B) without any outliers. The CA-ID-TIMS dates are interpreted as the crystallization ages of the volcanics.

Sample JP1710 was taken from a rhyolite unit in the Spitzkop Suite, which has been attributed as the source of the Rosh Pinah volcanics (Alchin et al., 2005). The sample is a fine-grained quartz rhyolite with welded clasts. LASS analyses for JP1710 provided a $^{206}Pb/^{238}U$ weighted mean date of 740 ± 14 Ma (2s, n = 26/26; Fig. 6C).

Nine samples from various units in the Stinkfontein Subgroup, Rosh Pinah Fm, and Holgat Fm were collected for detrital zircon analyses (Fig. 7). Kernel density estimates (KDEs) for the detrital dates in each sample are plotted in Fig. 7 along with a sample from the Numees Fm from Hofmann et al. (2015). The lowest samples in the section (JP1801C-26.9, F1814-366.0) within the Stinkfontein Subgroup were collected from interbedded, fine-grained, green and white sandstone beds and show a prominent date peak at ~1.9 Ga and a subsidiary peak at 1.1 Ga. No zircon grains in these samples were younger than 790 Ma. The next highest sample in the section, JP1801-51.3, is a schistose, blue-green pelite from the lowest exposures of the Rosh Pinah Fm with a similar dominant peak at ~1.9 Ga and secondary peaks at ~1.3, 1.2, and 1.1 Ga. In the Rosh Pinah Fm, the dominant peak shifts from ~1.9 Ga to 1.3 and 1.1 Ga. Up-section, there is a persistent population of ~1.9 Ga zircon, but it is a much smaller peak than in the samples at the base of the section. The older ~1.9-1.8 Ga peak becomes prominent again in the sample from the Numees Fm (Nam 79 from Hofmann et al., 2015) and the samples from the lower Holgat Fm and Namaskluft diamictite, but all samples maintain a significant portion of ~1.1 Ga zircon. The only sample that contains zircon grains that are Cryogenian in age is JP1805-0.8, taken from the Namaskluft diamictite just below the Marinoan cap carbonate. The two youngest grains have $^{206}Pb/^{238}U$ dates of 630 ± 22 Ma and 645 ± 23 Ma (2s).

E. Discussion

1. Depositional environments

    1.1. Stinkfontein Subgroup/Kaigas Formation

        The sedimentary facies observed in the Stinkfontein Subgroup in the Trekpoort Syncline are consistent with previous descriptions of conglomeratic alluvial fan to fan delta deposits that transition up-section to near-shore marine deposits, which formed off of an active fault scarp (Jasper et al., 2000). Particularly, on farm Trekpoort 96, wedge-shaped bodies of sedimentary breccia of the Kaigas Fm abut basement and are interpreted as proximal fan deposits near the base of topographic relief (e.g., see section F1814 in Fig. 3; Blair and McPherson, 2009). The sedimentary breccias are overlain by coarse-grained sandstone with meter-scale cross-stratification and foresets dipping to the west, northwest, and southeast (Fig. 3). These coarse-grained sandstone beds with variable foresets are interpreted to have formed as sand bars in a transitional fluvial to nearshore marine environment (e.g., Blair and McPherson, 2009).

        In our mapping, all deposits previously mapped as the Kaigas Fm by the Orange River have been reinterpreted as the Numees Fm (Fig. 5). On the autochthonous exposures, the Numees Fm consists of matrix-supported diamictite and sandstone that overlies basement, unlike at Trekpoort 96 where the Kaigas Fm consists of clast-supported sedimentary breccia that abuts basement along syn-sedimentary faults (Fig. 8). The Kaigas Fm is closely associated with the Rosh Pinah thrust fault, which was originally a west-dipping normal fault that created the accommodation space for rift-related deposits of the

Port Nolloth Group (Jasper et al., 1994). The Kaigas Fm is only observed near the Rosh Pinah Fault, indicating that Tonian displacement along the fault was a key factor in creating the basement topographic highs that shed the proximal fan deposits onto the hanging-wall parautochthonous blocks (Fig. 8).

1.2. Picklehaube and Rosh Pinah formations

The interbedded siliciclastic and carbonate rocks of the Picklehaube and Rosh Pinah formations capture the transition from terrestrial alluvial fan to shallow marine environments (Von Veh, 1988). Cross-stratification, soft-sediment deformation, coarse-grained calcarenites and microbial mats with rip-up clasts suggest a high-energy, near-shore environment. The repeated occurrences of gravel beds with cobble and boulder clasts are interpreted as subaqueous sediment gravity flows from a fan delta that experienced syndepositional tectonism during continued rifting. Similar matrix- and clast-supported conglomerates interbedded with sandstones and mudstones have been described in Miocene rift basins in the North American Basin and Range province and interpreted to define the intersection between subaqueous fan delta and nearshore environments (e.g., Horton and Schmitt, 1996). Deepening of the basin over time is indicated by the fining-up sequences of the siliciclastic rocks from conglomerates and sandstones to siltstones and dark grey shales. Graded beds in the upper portion of the sequence, previously assigned to the Wallekraal Fm (Frimmel, 2018) and now assigned to the Tonian Rosh Pinah Fm, are interpreted as turbidites that indicate a transition to an offshore slope to basin environment.

53

1.3. Numees Formation

The turbidites of the upper Hilda Subgroup coarsen to fine- to medium-grained sandstone beds before the first appearance of dropstones, consistent with shallowing at the onset of Cryogenian glaciation (Hoffman et al., 2017). The gradational contact suggests existing accommodation space and/or tectonically-driven subsidence outpaced glacioeustatic sea level fall. The stratigraphic progression of the Numees Fm at Trekpoort 96 from turbidites interbedded with stratified diamictite to crudely bedded and weakly sorted massive diamictites is interpreted to record progradation from ice-rafted debris to flow tills that formed directly offboard of the ice-grounding line (e.g., Domack and Hoffman, 2011).

2. Detrital zircon geochronology and stratigraphic correlations

Previous detrital zircon studies that have been conducted on sandstone and diamictite samples from Namaskluft farm, Dreigratberg, and Trekpoort 96 show peaks in dates at 1.9, 1.3, 1.2, and 1.1 Ga, with no late Tonian to Cryogenian ages (Hofmann et al., 2014; Foster et al., 2015; Gaschnig et al., 2022; Zieger-Hofmann et al., 2022). The absence of Cryogenian-aged detrital zircon can be explained by a late Tonian to early Cryogenian rift-drift transition (Macdonald et al., 2010) and rapid burial by older cratonic material during rifting due to rift-generated topography (e.g., Jasper et al., 1994).

Due to the rarity of syndepositional zircon, Hofmann et al. (2014) proposed using ratios of the number of Paleoproterozoic and Mesoproterozoic grains (P/M) in each sample to

distinguish their stratigraphic positions and correlations, with the older samples having distinctly higher P/M values. As a result, they interpreted the diamictite exposures nonconformably overlying the basement gneisses just north of the Orange River as the Kaigas Fm based on clast composition, detrital zircon spectra, and the assignment of the overlying carbonate units to the Picklehaube Fm (Gaschnig et al., 2022; Zieger-Hofmann et al., 2022). However, clast composition and detrital zircon spectra are non-unique characteristics of the diamictites; for example, in the compilation by Zieger-Hofmann et al. (2022), the detrital spectra for the Kaigas and Numees formations from Namaskluft, Orange River, and Dreigratberg are indistinguishable because they reflect deposition in similar environments on the autochthon next to the same basement sources. The P/M ratio of each sample could instead be interpreted to reflect the local sources and basin geometry rather than the timing of deposition and cannot be used diagnostically to determine the identity of the formation.

Despite the rarity of young grains, a few Cryogenian detrital zircon dates were identified in the sample taken from the Namaskluft diamictite 20 cm below the Dreigratberg cap carbonate at the northeastern exposure by Orange River (sample JP1805-0.8; Fig. 5). The two youngest detrital zircon grains constrain the age of this diamictite to $<645 \pm 23$ Ma and $<630 \pm 22$ Ma. These dates preclude correlation with the 717-660 Ma Sturtian diamictite and overlap within uncertainty with the >639-635 Ma Marinoan glaciation (Prave et al., 2016), supporting the stratigraphic interpretation that the autochthonous units are the Cryogenian to Ediacaran Holgat Fm (Macdonald et al., 2010) rather than the Tonian Picklehaube Fm.

Jasper et al. (1994, 2000) previously identified the Rosh Pinah thrust fault (Figs. 1, 3) as a major structural and stratigraphic boundary in the Port Nolloth Group. The Rosh Pinah

thrust fault was originally a west-dipping normal fault that created accommodation space for the syn-rift deposits of the Port Nolloth Group (Jasper et al., 1994; Fig. 8). Stratigraphic sections to the east of the fault are autochthonous, typically truncated and deposited nonconformably on basement (Fig. 5), while to the west, thrust slices preserve thicker and deeper-water parautochthonous rift sequences (Fig. 3; Jasper et al., 1994). Contraction during Ediacaran to Cambrian orogenic events reactivated some of the extensional fault planes as thrust faults, and syn-rift sequences were inverted and folded (Jasper et al., 1994, 2000). Our mapping and stratigraphy results (Fig. 5) demonstrate that north of the Orange River, there is a conformable contact between the diamictite nonconformably overlying basement and the Bloeddrif Member above. These units are to the east of the Rosh Pinah Fault, which can be traced north into younger Cryogenian and Ediacaran units (Fig. 1, Fig. 5). Thus, along the Orange River and in autochthonous sections at Namasberg and in South Africa (Fig. 8; Macdonald et al., 2010), it is the Numees Fm rather than the Kaigas Fm that onlaps on basement, sealing the Tonian to Cryogenian Rosh Pinah fault. Descriptions of the Kaigas Fm as a glacial deposit (Frimmel, 2008, 2018) are inconsistent with its type locality description and are miscorrelated, as multiple authors have recognized (Jasper et al., 2000; Macdonald et al., 2010; Zieger-Hofmann et al., 2022).

3. Implications for Tonian glaciation

Our results demonstrate that there is no evidence for Tonian glaciation on the Kalahari craton. Globally, the one remaining location with putative evidence for Tonian glaciation is in the Konnarock Fm and associated Mount Rogers Fm in eastern Laurentia (Miller, 2004;

Merschat et al., 2014; MacLennan et al., 2020). Because these deposits formed at low-latitude based on established paleomagnetic poles (e.g., Eyster et al., 2020), MacLennan et al. (2020) suggested that the region could have been at high-altitude for glaciation to occur in lieu of a global glaciation event. However, like in the Rosh Pinah graben, the Mount Rogers and Konnarock formations are also associated with an active volcanic rift (Rankin, 1993; Miller, 2004), complicating the interpretation of a glaciogenic origin for the diamictites (e.g., Horton and Schmitt, 1996). While parts of the Konnarock Fm have definitive evidence for glaciation that are likely ca. 717-660 Ma Sturtian in age (Miller, 2004; Merschat et al., 2014), correlations and mapping in the area are difficult due to the lack of exposure and the fact that the Mount Rogers Fm also contains siliciclastic conglomerates with outsized clasts (Rankin, 1993). Whether the ca. 753 Ma Laurentia diamictites interpreted by MacLennan et al. (2020) are a record of glaciation or could instead be non-glacigenic and the result of deposition in an active rift basin is critical for interpreting Earth's climate state in this interval of the Tonian. Regardless, there is no evidence of Tonian glaciomarine deposition at the time on the Kalahari craton and the concept of a Kaigas glaciation should be discontinued in the literature.

4. Neoproterozoic paleogeography of Kalahari Craton

A common configuration for Kalahari's position within Rodinia is that it was conjoined to southeastern Laurentia with Amazonia as a conjugate continent laterally along the same margin (Fig. 9; e.g., Evans, 2021). This configuration considers the Grenville orogen of Laurentia and the Namaqua-Natal orogen of Kalahari to be conjugate events associated with Rodinia assembly (Evans, 2021), with the study area facing Laurentia (Fig. 9). Although

this position is consistent with the comparison between early Tonian poles from the Grenville and Namaqua-Natal belts, constraining the magnetization age of these poles is difficult and there is a lack of late Tonian poles from Kalahari that could be compared to late Tonian poles from Laurentia. As a result, different models for the position of Kalahari within Rodinia are possible (e.g., Gumsley et al., 2023). In this context, the timing of rifting and rift-related magmatic activity can aid in developing and testing models.

The Gannakouriep dikes and associated bimodal volcanism on Kalahari craton indicate some intraplate magmatism at 793 + 1.7/-1.5 Ma (Rioux et al., 2010). Differential subsidence leading into ca. 717 Ma Sturtian glaciation as well as the ca. 752 Ma Rosh Pinah volcanism are indicative of Tonian rifting that would have transitioned to thermal subsidence in the Cryogenian. This timing of rift basin development and associated magmatism is similar along the southern Appalachian portion of Laurentia's margin (McClellan and Gazel, 2014; Macdonald et al., 2023), such that the Rosh Pinah volcanics of Kalahari and the Mount Rogers Fm volcanics of Laurentia could be the expression of conjugate rifting margins at ca. 750 Ma. In the case of Laurentia, however, a passive margin did not develop until the Cambrian, more than 200 Myr later (Smoot and Southworth, 2014). This reconstruction leaves the question of what rifted from the Southern Appalachians to account for the Cambrian rift-drift transition on southwestern Laurentia (Smoot and Southworth, 2014). A likely candidate is the AREPA terrane of South America, including the Arequipa terrane, which has been suggested to be originally a piece of Proterozoic Kalahari crust that collided with Laurentia during the Grenville Orogeny and then separated during rifting (Loewy et al., 2003)—first, from Kalahari in the Tonian to Cryogenian and then from Laurentia in the Ediacaran (Hodgin et al.,

2023; Macdonald et al., 2023). AREPA terranes contain ca. 850-750 Ma detrital zircon with trace element geochemistry consistent with an intraplate origin, potentially tying AREPA to the Gannakouriep dikes (Rapela et al., 2016; Hodgin et al., 2023) and providing the missing link between Kalahari and Laurentia.

The tie proposed here between the 752 Ma Rosh Pinah volcanics and extensional basin tectonics on the SW Kalahari margin and the 752 Ma Mount Rogers complex of Virginia on the SE Laurentia margin also raises questions about the relative position of the Congo craton at this time (see supplementary text 2.2). Rift-related magmatism on the southern Congo margin at 757 ± 5 Ma, 759.95 ± 0.86 Ma, 746 ± 2, and 747 ± 2 Ma (Hoffman et al., 1996; Halverson et al., 2005; Nascimento et al., 2017) could be associated with a similar extensional region to the Rosh Pinah Fm and Mount Rogers complex, but the orientation and paleolatitude for Congo are constrained by paleomagnetic poles from the ca. 765 Luakela Volcanics (Wingate et al., 2010) and the ca. 755 Ma Mbozi Complex (Meert et al., 1995), which precludes a direct connection to the Damara margin of Kalahari and Laurentia. We propose that the Brasiliano Ocean opened as Congo separated from Rodinia with rifting between Kalahari and Laurentia opening the paleo-Iapetus Ocean soon thereafter (Fig. 9). The Iapetus Ocean would have subsequently formed with the rifting of AREPA from Laurentia.

4.1 Connecting zircon provenance to the paleogeography

Detrital zircon peaks in the Port Nolloth Group spanning 2.0-1.7 Ga were likely sourced from the 2.0 Ga Orange River Group and the 1.9-1.7 Ga Vioolsdrif Granite Suite of the Richtersveld Subprovince and Mesoproterozoic grains from the 1.4-1.0 Ga

Namaqua Belt and the Umkondo LIP (Miller, 2012; Hofmann et al., 2014). In comparison, Mesoproterozoic geochronology in the Laurentian basement massifs define three major periods of orogenesis with associated zircon crystallization: the Elzevirian (1.25-1.22 Ga), Shawinigan (1.19-1.16 Ga), and Grenvillian (1.09-0.98 Ga) (e.g., Makovsky et al., 2021; Swanson-Hysell et al., 2022). The youngest of these peaks is not well-resolved in our data. This difference may stem from the possibility that the Ottawan phase of the Grenville orogeny does not have a counterpart in the Namibian sector of the Namaqua belt, but instead is present just south of the Orange River in the Bushmanland and Garies terranes (parts of the Namaqua Belt labeled "B" and "G" respectively in Fig. 1A; see supplementary text 2.1), and/or the Arequipa terrane, which all preserve 1.06-1.01 Ga dates (Cornell et al., 2009; Hodgin et al., 2023). Thus, if the proposed tie between the Rosh Pinah volcanics and Mount Rogers Fm is correct, then the 1065-1010 Ma belts in the Bushmanland and Garies terranes reflect orogenesis correlative with the Ottawan phase, with the western Namaqua margin emplaced against the AREPA terranes and Blue Ridge in a dextral, oblique collision (Fig. 9; Miller, 2012). In this scenario, when Kalahari rifted away during the late Tonian to Cryogenian, sediments were sourced from Kalahari crust to the northeast (in present-day coordinates), along the rift shoulder defined by the Rosh Pinah fault (Fig. 1B), such that 1065-1010 Ma detritus from the Bushmanland and Garies terranes to the south and west was rare due to rift geometry.

F. Conclusions

Exposures of the Port Nolloth Group on Trekpoort Farm capture rifting in the deposition of the Stinkfontein Subgroup through the Numees Fm. Our CA-ID-TIMS weighted mean ^{206}Pb/^{238}U dates of 752.38 ± 0.26 and 751.82 ± 0.32 Ma from rhyolites in the Rosh Pinah Fm supersede the previous Pb-Pb zircon evaporation (Frimmel et al., 1996b) and SHRIMP U-Pb dates (Borg et al., 2003). Deposition of the Picklehaube and Rosh Pinah formations on Trekpoort Farm occurred roughly between >752-717 Ma. Detrital zircon geochronology supports a link between Kalahari craton and Laurentia during the Grenvillian Orogeny with potentially other intermediate terranes (e.g., AREPA).

Our mapping, stratigraphy, and geochronology shows that the ~750 Ma deposits of the Kaigas Fm are alluvial fan, fan delta, and turbidite sequences deposited during rifting of the Kalahari craton and other conjugate terranes from Laurentia, but they do not show glacial influence. If there is a ca. 750 Ma link between Kalahari and Laurentia due to the correlation of the Kaigas and Mount Rogers Fm, then the link is due to rifting, not glaciation. Our findings do not support the interpretation that there was low-latitude glaciation during the Tonian or that the Earth was teetering on the edge of global glaciation for tens of millions of years before the onset of the Sturtian Snowball Earth.

G. Acknowledgments

H. References

Alchin, D.J., Frimmel, H.E., and Jacobs, L.E., 2005, Stratigraphic setting of the metalliferous Rosh Pinah Formation and the Spitzkop and Koivib Suites in the Pan-African Gariep Belt, southwestern Namibia: South African Journal of Geology, v. 108, p. 19–34.

Allen, P.A., and Etienne, J.L., 2008, Sedimentary challenge to Snowball Earth: Nature Geoscience, v. 1, p. 817–825, doi:10.1038/ngeo355.

Blair, T.C., and McPherson, J.G., 2009, Processes and Forms of Alluvial Fans, *in* Parsons, A.J. and Abrahams, A.D. eds., Geomorphology of Desert Environments, Dordrecht, Springer Netherlands, p. 413–467, doi:10.1007/978-1-4020-5719-9_14.

Borg, G., Kärner, K., Buxton, M., Armstrong, R., and van der Merwe, S.W., 2003, Geology of the Skorpion Supergene Zinc Deposit, Southern Namibia: Economic Geology, v. 98, p. 749–771, doi:10.2113/gsecongeo.98.4.749.

Bowring, S.A., Grotzinger, J.P., Condon, D.J., Ramezani, J., Newall, M.J., and Allen, P.A., 2007, Geochronologic constraints on the chronostratigraphic framework of the Neoproterozoic Huqf Supergroup, Sultanate of Oman: American Journal of Science, v. 307, p. 1097–1145, doi:10.2475/10.2007.01.

Cornell, D.H., Pettersson, A., Whitehouse, M.J., and Schersten, A., 2009, A New Chronostratigraphic Paradigm for the Age and Tectonic History of the Mesoproterozoic Bushmanland Ore District, South Africa: Economic Geology, v. 104, p. 385–404, doi:10.2113/gsecongeo.104.3.385.

Denyszyn, S.W., Halls, H.C., Davis, D.W., and Evans, D.A.D., 2009, Paleomagnetism and U-Pb geochronology of Franklin dykes in High Arctic Canada and Greenland: a revised age and paleomagnetic pole constraining block rotations in the Nares Strait region: Canadian Journal of Earth Sciences, v. 46, p. 689–705, doi:10.1139/E09-042.

Domack, E.W., and Hoffman, P.F., 2011, An ice grounding-line wedge from the Ghaub glaciation (635 Ma) on the distal foreslope of the Otavi carbonate platform, Namibia, and its bearing on the snowball Earth hypothesis: GSA Bulletin, v. 123, p. 1448–1477, doi:10.1130/B30217.1.

Evans, D.A.D., 2021, Meso-Neoproterozoic Rodinia supercycle, *in* Pesonen, L.J., Salminen,

J., Elming, S.-.-Å., Evans, D.A.D., and Veikkolainen, T. eds., Ancient Supercontinents and the Paleogeography of Earth, Elsevier, p. 549–576, doi:10.1016/B978-0-12-818533-9.00006-0.

Eyster, A., Weiss, B.P., Karlstrom, K., and Macdonald, F.A., 2020, Paleomagnetism of the Chuar Group and evaluation of the late Tonian Laurentian apparent polar wander path with implications for the makeup and breakup of Rodinia: GSA Bulletin, v. 132, p. 710–738, doi:10.1130/B32012.1.

Ferreira, D., Marshall, J., and Rose, B., 2011, Climate determinism revisited: Multiple equilibria in a complex climate model: Journal of Climate, v. 24, p. 992–1012, doi:10.1175/2010JCLI3580.1.

Foster, D.A., Goscombe, B.D., Newstead, B., Mapani, B., Mueller, P.A., Gregory, L.C., and Muvangua, E., 2015, U-Pb age and Lu-Hf isotopic data of detrital zircons from the Neoproterozoic Damara Sequence: Implications for Congo and Kalahari before Gondwana: Gondwana Research, v. 28, p. 179–190, doi:10.1016/j.gr.2014.04.011.

Frimmel, H.E., 2008, Neoproterozoic Gariep Orogen, *in* Miller, R.M. ed., The Geology of Namibia: Volume 2, Neoproterozoic to Lower Palaeozoic, Geological Survey of Namibia, p. 14.1-14.39.

Frimmel, H.E., 2018, The Gariep Belt, *in* Geology of Southwest Gondwana, Springer International Publishing, p. 353–386, doi:10.1007/978-3-319-68920-3_13.

Frimmel, H.E., Hartnady, C.J.H., and Koller, F., 1996a, Geochemistry and tectonic setting of magmatic units in the Pan-African Gariep Belt, Namibia: Chemical Geology, v. 130, p. 101–121, doi:10.1016/0009-2541(95)00188-3.

Frimmel, H.E., Klötzli, U.S., and Siegfried, P.R., 1996b, New Pb-Pb single zircon age constraints on the timing of neoproterozoic glaciation and continental break-up in Namibia: Journal of Geology, v. 104, p. 459–469, doi:10.1086/629839.

Gaschnig, R.M., Horan, M.F., Rudnick, R.L., Vervoort, J.D., and Fisher, C.M., 2022, History of crustal growth in Africa and the Americas from detrital zircon and Nd isotopes in glacial diamictites: Precambrian Research, v. 373, doi:10.1016/j.precamres.2022.106641.

Grotzinger, J.P., Bowring, S.A., Saylor, B.Z., and Kaufman, A.J., 1995, Biostratigraphic and geochronologic constraints on early animal evolution: Science, v. 270, p. 598–604, doi:10.1126/science.270.5236.598.

Gumsley, A.P.A. et al., 2023, The Mutare–Fingeren dyke swarm: the enigma of the Kalahari Craton's exit from supercontinent Rodinia: Geological Society, London, Special Publications, v. 537, doi:10.1144/sp537-2022-206.

Halverson, G.P., Hoffman, P.F., Schrag, D.P., Maloof, A.C., and Rice, A.H.N., 2005, Toward a Neoproterozoic composite carbon-isotope record: GSA Bulletin, v. 117, p. 1181–1207, doi:10.1130/B25630.1.

Hanson, R.E., 2003, Proterozoic geochronology and tectonic evolution of southern Africa: Geological Society Special Publication, v. 206, p. 427–463, doi:10.1144/GSL.SP.2003.206.01.20.

Hodgin, E.B., Carlotto, V., Macdonald, F.A., Schmitz, M.D., and Crowley, J.L., 2023, New age constraints on the break-up of Rodinia and amalgamation of southwestern Gondwana from the Choquequirao Formation in southwestern Peru: Geological Society, London, Special Publications, v. 531, doi:10.1144/sp531-2022-197.

Hoffman, P.F., 2009, Pan-glacial—a third state in the climate system: Geology Today, v. 25, p. 100–107, doi:10.1111/j.1365-2451.2009.00716.x.

Hoffman, P.F. et al., 2017, Snowball Earth climate dynamics and Cryogenian geology-geobiology: Science Advances, v. 3, p. 43, doi:10.1126/sciadv.1600983.

Hoffman, P.F., Hawkins, D.P., Isachsen, C.E., and Bowring, S.A., 1996, Precise U-Pb zircon ages for early Damaran magmatism in the Summas Mountains and Welwitschia Inlier, northern Damara Belt, Namibia: Communs geol. Surv. Namibia, v. 11, p. 49–53.

Hoffman, P.F., and Schrag, D.P., 2002, The snowball Earth hypothesis: testing the limits of global change: Terra Nova, v. 14, p. 129–155, doi:10.1046/j.1365-3121.2002.00408.x.

Hofmann, M., Linnemann, U., Hoffmann, K.H., Gerdes, A., Eckelmann, K., and Gärtner, A., 2014, The Namuskluft and Dreigratberg sections in southern Namibia (Kalahari Craton, Gariep Belt): A geological history of Neoproterozoic rifting and recycling of cratonic crust during the dispersal of Rodinia until the amalgamation of Gondwana: International Journal of Earth Sciences, v. 103, p. 1187–1202, doi:10.1007/s00531-013-0949-6.

Hofmann, M., Linnemann, U., Hoffmann, K.H., Germs, G., Gerdes, A., Marko, L., Eckelmann, K., Gärtner, A., and Krause, R., 2015, The four Neoproterozoic glaciations of southern Namibia and their detrital zircon record: The fingerprints of four crustal growth events during two supercontinent cycles: Precambrian Research, v. 259, p. 176–188, doi:10.1016/j.precamres.2014.07.021.

Horstwood, M.S.A. et al., 2016, Community-Derived Standards for LA-ICP-MS U-(Th-)Pb Geochronology – Uncertainty Propagation, Age Interpretation and Data Reporting: Geostandards and Geoanalytical Research, v. 40, p. 311–332, doi:10.1111/j.1751-908X.2016.00379.x.

Horton, B.K., and Schmitt, J.G., 1996, Sedimentology of a lacustrine fan-delta system, Miocene Horse Camp Formation, Nevada, USA: Sedimentology, v. 43, p. 133–155, doi:10.1111/j.1365-3091.1996.tb01464.x.

Jaffey, A.H., Flynn, K.F., Glendenin, L.E., Bentley, W.C., and Essling, A.M., 1971, Precision measurement of half-lives and specific activities of ^{235}U and ^{238}U: Physical Review C, v. 4, p. 1889–1906, doi:10.1103/PhysRevC.4.1889.

Jasper, M.J.U., Stanistreet, I.G., and Charlesworth, E.G., 2000, Neoproterozoic inversion tectonics, half-graben depositories and glacial controversies, Gariep fold-thrust belt, southern Namibia: Communs geol. Surv. Namibia, v. 12, p. 187–196.

Jasper, M.J.U., Stanistreet, I.G., and Charlesworth, E.G., 1994, Recognition of Inversion Tectonics Within the Pan African Gariep Belt (Damara Orogen) in Southern Namibia.:

Jasper, M.J.U., Stanistreet, I.G., and Charlesworth, E.G., 1992, Report: Preliminary results of a study of the structural and sedimentological evolution of the late Proterozoic/early Palaeozoic.:

Key, R.M., Liyungu, A.K., Njamu, F.M., Somwe, V., Banda, J., Mosley, P.N., and Armstrong, R.A., 2001, The western arm of the Lufilian Arc in NW Zambia and its potential for copper mineralization: Journal of African Earth Sciences, v. 33, p. 503–528, doi:10.1016/s0899-5362(01)00098-7.

Kröner, A., 1975, Late Precambrian Formations in the Western Richtersveld, Northern Cape Province: v. 41, 375–433 p., doi:10.1080/00359197509519451.

Kylander-Clark, A.R.C., 2017, Petrochronology by Laser-Ablation Inductively Coupled Plasma Mass Spectrometry: Reviews in Mineralogy and Geochemistry, v. 83, p. 183–198, doi:10.2138/rmg.2017.83.6.

Kylander-Clark, A.R.C., Hacker, B.R., and Cottle, J.M., 2013, Laser-ablation split-stream ICP petrochronology: Chemical Geology, v. 345, p. 99–112, doi:10.1016/j.chemgeo.2013.02.019.

Linnemann, U. et al., 2019, New high-resolution age data from the Ediacaran–Cambrian boundary indicate rapid, ecologically driven onset of the Cambrian explosion: Terra Nova, v. 31, p. 49–58, doi:10.1111/ter.12368.

Loewy, S.L., Connelly, J.N., Dalziel, I.W.D., and Gower, C.F., 2003, Eastern Laurentia in Rodinia: Constraints from whole-rock Pb and U/Pb geochronology: Tectonophysics, v. 375, p. 169–197, doi:10.1016/S0040-1951(03)00338-X.

Macdonald, F.A., Schmitz, M.D., Strauss, J. V., Halverson, G.P., Gibson, T.M., Eyster, A., Cox, G., Mamrol, P., and Crowley, J.L., 2017, Cryogenian of Yukon: Precambrian Research, v. 319, p. 114–143, doi:10.1016/j.precamres.2017.08.015.

Macdonald, F.A., Strauss, J. V., Rose, C. V., Dudás, F.Ö., and Schrag, D.P., 2010, Stratigraphy of the Port Nolloth Group of Namibia and South Africa and Implications for the Age of Neoproterozoic Iron Formations: American Journal of Science, v. 310, p. 862–888, doi:10.2475/09.2010.05.

Macdonald, F.A., Yonkee, W.A., Flowers, R.M., and Swanson-Hysell, N.L., 2023, Neoproterozoic of Laurentia: Memoir of the Geological Society of America, v. 220, p. 331–380, doi:10.1130/2022.1220(19).

MacLennan, S.A., Eddy, M.P., Merschat, A.J., Mehra, A.K., Crockford, P.W., Maloof, A.C., Southworth, C.S., and Schoene, B., 2020, Geologic evidence for an icehouse Earth before the Sturtian global glaciation: Science Advances, v. 6, p. 1–6, doi:10.1126/sciadv.aay6647.

Makovsky, K., Samson, S.D., Moecher, D.P., and Amidon, W., 2021, Timing of Grenville

magmatism in the southern Blue Ridge, North Carolina, USA: New in situ zircon U-Pb geochronology and implications for timing of Rodinian orogenesis in eastern Laurentia: Precambrian Research, v. 363, p. 106313, doi:10.1016/j.precamres.2021.106313.

McClellan, E., and Gazel, E., 2014, The Cryogenian intra-continental rifting of Rodinia: Evidence from the Laurentian margin in eastern North America: Lithos, v. 206–207, p. 321–337, doi:10.1016/j.lithos.2014.08.006.

Meert, J.G., van der Voo, R., and Ayub, S., 1995, Paleomagnetic investigation of the Neoproterozoic Gagwe lavas and Mbozi complex, Tanzania and the assembly of Gondwana: Precambrian Research, v. 74, p. 225–244, doi:10.1016/0301-9268(95)00012-T.

Merschat, A.J., Southworth, S., McClellan, E., Tollo, R.P., Rankin, D.W., Hooper, S., and Bauer, S., 2014, Key structural and stratigraphic relationships from the northeast end of the Mountain City window and the Mount Rogers area, Virginia–North Carolina–Tennessee: Elevating Geoscience in the Southeastern United States: New Ideas about Old Terranes—Field Guides for the GSA Southeastern Section Meeting, Blacksburg, Virginia, 2014, v. 0035, p. 63–101, doi:10.1130/2014.0035(03).

Miller, R.M., 2012, Review of Mesoproterozoic Magmatism, Sedimentation and Terrane Amalgamation in Southwestern Africa: South African Journal of Geology, v. 115, p. 417–448, doi:10.2113/gssajg.115.4.417.

Miller, J.M.G., 2004, The Neoproterozoic Konnarock Formation, southwestern Virginia, USA: glaciolacustrine facies in a continental rift, in Deynoux, M., Miller, J.M.G., Domack, E.W., Eyles, N., Fairchild, I.J., and Young, G.M. eds., Earth's Glacial Record, Cambridge, UK, Cambridge University Press, p. 47–59, doi:10.1017/cbo9780511628900.004.

Nascimento, D.B., Schmitt, R.S., Ribeiro, A., Trouw, R.A.J., Passchier, C.W., and Basei, M.A.S., 2017, Depositional ages and provenance of the Neoproterozoic Damara Supergroup (northwest Namibia): Implications for the Angola-Congo and Kalahari cratons connection: Gondwana Research, v. 52, p. 153–171, doi:10.1016/j.gr.2017.09.006.

Park, Y. et al., 2020, The lead-up to the Sturtian Snowball Earth: Neoproterozoic chemostratigraphy time-calibrated by the Tambien Group of Ethiopia: GSA Bulletin, v. 132, p. 1119–1149, doi:10.1130/B35178.1.

Paton, C., Hellstrom, J., Paul, B., Woodhead, J., and Hergt, J., 2011, Iolite: Freeware for the visualisation and processing of mass spectrometric data: Journal of Analytical Atomic Spectrometry, v. 26, p. 2508, doi:10.1039/c1ja10172b.

Paton, C., Woodhead, J.D., Hellstrom, J.C., Hergt, J.M., Greig, A., and Maas, R., 2010, Improved laser ablation U-Pb zircon geochronology through robust downhole fractionation correction: Geochemistry, Geophysics, Geosystems, v. 11, doi:10.1029/2009GC002618.

Pisarevsky, S.A., Gladkochub, D.P., Konstantinov, K.M., Mazukabzov, A.M., Stanevich, A.M., Murphy, J.B., Tait, J.A., Donskaya, T. V., and Konstantinov, I.K., 2013, Paleomagnetism of Cryogenian Kitoi mafic dykes in South Siberia: Implications for Neoproterozoic paleogeography: Precambrian Research, v. 231, p. 372–382, doi:10.1016/j.precamres.2013.04.007.

Prave, A.R., Condon, D.J., Hoffmann, K.H., Tapster, S., and Fallick, A.E., 2016, Duration and nature of the end-Cryogenian (Marinoan) glaciation: Geology, v. 44, p. 631–634, doi:10.1130/G38089.1.

Ramezani, J., Beveridge, T.L., Rogers, R.R., Eberth, D.A., and Roberts, E.M., 2022, Calibrating the zenith of dinosaur diversity in the Campanian of the Western Interior Basin by CA-ID-TIMS U–Pb geochronology: Scientific Reports, v. 12, p. 1–20, doi:10.1038/s41598-022-19896-w.

Rankin, D.W., 1993, The Volcanogenic Mount Rogers Formation and the Overlying Glaciogenic Konnarock Formation—Two Late Proterozoic Units in Southwestern Virginia: U.S. Geological Survey Bulletin, v. 2029, p. 26.

Rapela, C.W., Verdecchia, S.O., Casquet, C., Pankhurst, R.J., Baldo, E.G., Galindo, C., Murra, J.A., Dahlquist, J.A., and Fanning, C.M., 2016, Identifying Laurentian and SW Gondwana sources in the Neoproterozoic to Early Paleozoic metasedimentary rocks of the Sierras Pampeanas: Paleogeographic and tectonic implications: Gondwana Research, v. 32, p. 193–212, doi:10.1016/j.gr.2015.02.010.

Rioux, M., Bowring, S., Dudás, F., and Hanson, R., 2010, Characterizing the U-Pb systematics of baddeleyite through chemical abrasion: Application of multi-step digestion methods to baddeleyite geochronology: Contributions to Mineralogy and Petrology, v. 160, p. 777–801, doi:10.1007/s00410-010-0507-1.

Rooney, A.D., Strauss, J. V., Brandon, A.D., and Macdonald, F.A., 2015, A Cryogenian chronology: Two long-lasting synchronous neoproterozoic glaciations: Geology, v. 43, p. 459–462, doi:10.1130/G36511.1.

Smoot, J.P., and Southworth, S., 2014, Volcanic rift margin model for the rift-to-drift setting of the late Neoproterozoic-early Cambrian eastern margin of Laurentia: Chilhowee Group of the Appalachian Blue Ridge: Bulletin of the Geological Society of America, v. 126, p. 201–218, doi:10.1130/B30875.1.

Swanson-Hysell, N.L., Maloof, A.C., Kirschvink, J.L., Evans, D.A.D., Halverson, G.P., and Hurtgen, M.T., 2012, Constraints on Neoproterozoic paleogeography and Paleozoic orogenesis from paleomagnetic records of the Bitter Springs Formation, Amadeus Basin, central Australia: American Journal of Science, v. 312, p. 817–884, doi:10.2475/08.2012.01.

Swanson-Hysell, N.L., Rivers, T., and van der Lee, S., 2022, The late Mesoproterozoic to early Neoproterozoic Grenvillian orogeny and the assembly of Rodinia: Turning point in the tectonic evolution of Laurentia, *in* Whitmeyer, S.J., Williams, M.L., Kellett, D.A., and Tikoff, B. eds., Laurentia: Turning Points in the Evolution of a Continent, Geological

Society of America, p. 221–250, doi:10.1130/2022.1220(14).

Von Veh, M.W., 1988, The Stratigraphy and Structural Evolution of the Late Proterozoic Gariep Belt in the Sendelingsdrif-Annisfontein Area, Northwestern Cape Province: 174 p.

Vermeesch, P., 2018, IsoplotR: A free and open toolbox for geochronology: Geoscience Frontiers, v. 9, p. 1479–1493, doi:10.1016/j.gsf.2018.04.001.

Weil, A.B., Geissman, J.W., and Ashby, J.M., 2006, A new paleomagnetic pole for the Neoproterozoic Uinta Mountain supergroup, Central Rocky Mountain States, USA: Precambrian Research, v. 147, p. 234–259, doi:10.1016/j.precamres.2006.01.017.

Wingate, M.T.D., Pisarevsky, S.A., and De Waele, B., 2010, Paleomagnetism of the 765 Ma Luakela volcanics in Northwest Zambia and implications for Neoproterozoic positions of the Congo Craton: American Journal of Science, v. 310, p. 1333–1344, doi:10.2475/10.2010.05.

Xu, B., Xiao, S., Zou, H., Chen, Y., Li, Z.X., Song, B., Liu, D., Zhou, C., and Yuan, X., 2009, SHRIMP zircon U-Pb age constraints on Neoproterozoic Quruqtagh diamictites in NW China: Precambrian Research, v. 168, p. 247–258, doi:10.1016/j.precamres.2008.10.008.

Zieger-Hofmann, M. et al., 2022, Correlation of Neoproterozoic diamictites in southern Namibia: Earth-Science Reviews, v. 233, doi:10.1016/j.earscirev.2022.104159.

I. Figures
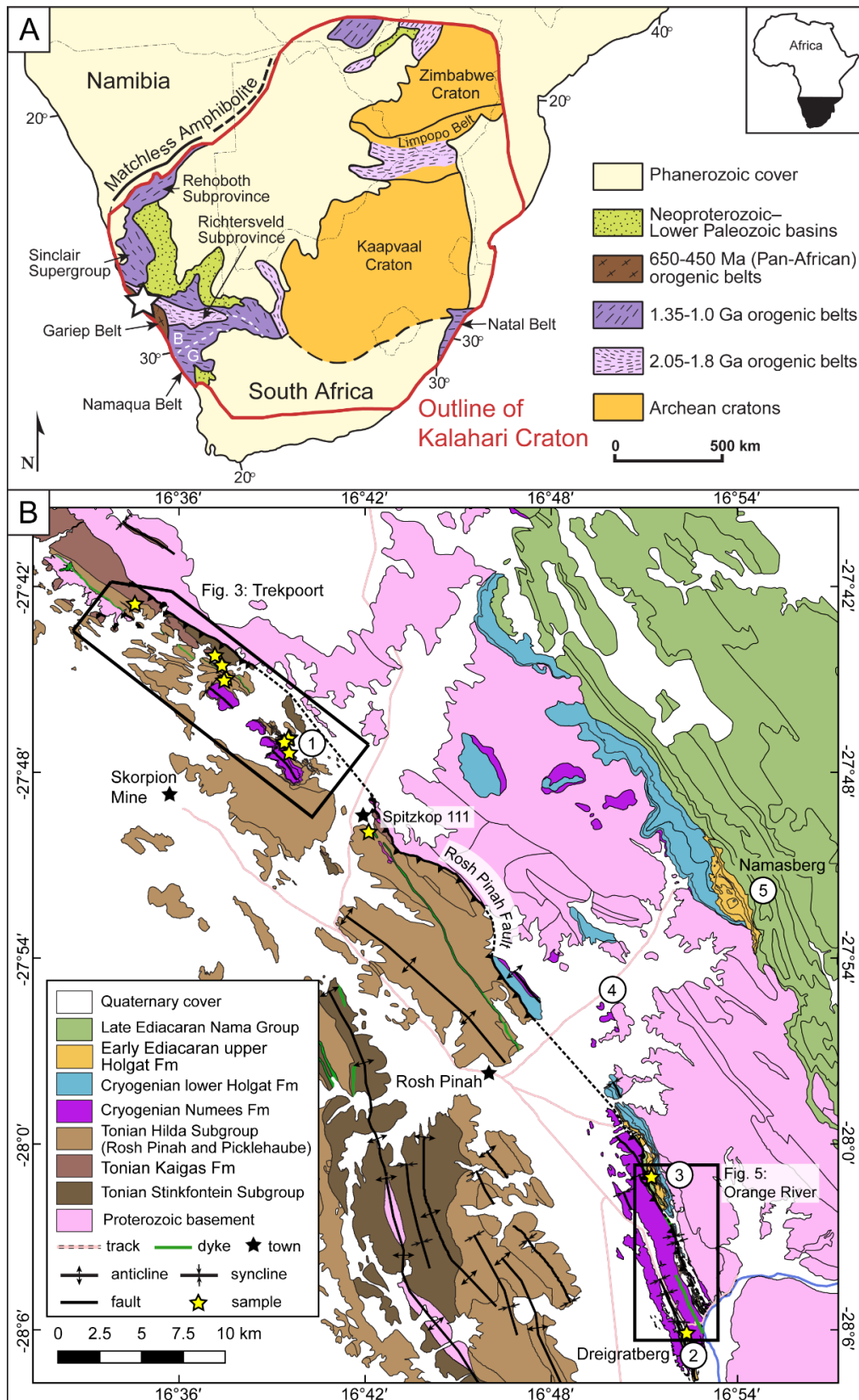
Figure 1. A) Tectonic map of southern Africa showing the outline of Kalahari craton in the Neoproterozoic, modified from Hanson (2003) and references therein. The Bushmanland and Garies terranes of the Namaqua Belt are outlined with white dashed lines following Miller (2012) and labeled with a "B" and "G" respectively. The white star indicates the location of the more detailed map in B. **B)** Geologic map of the overall study region modified from Von Veh (1988), Jasper et al. (1994), and Macdonald et al. (2010). Black boxes indicate locations of zoomed-in maps in Figs. 3 and 5. Circled numbers indicate locations of the composite stratigraphic sections in Fig. 8.
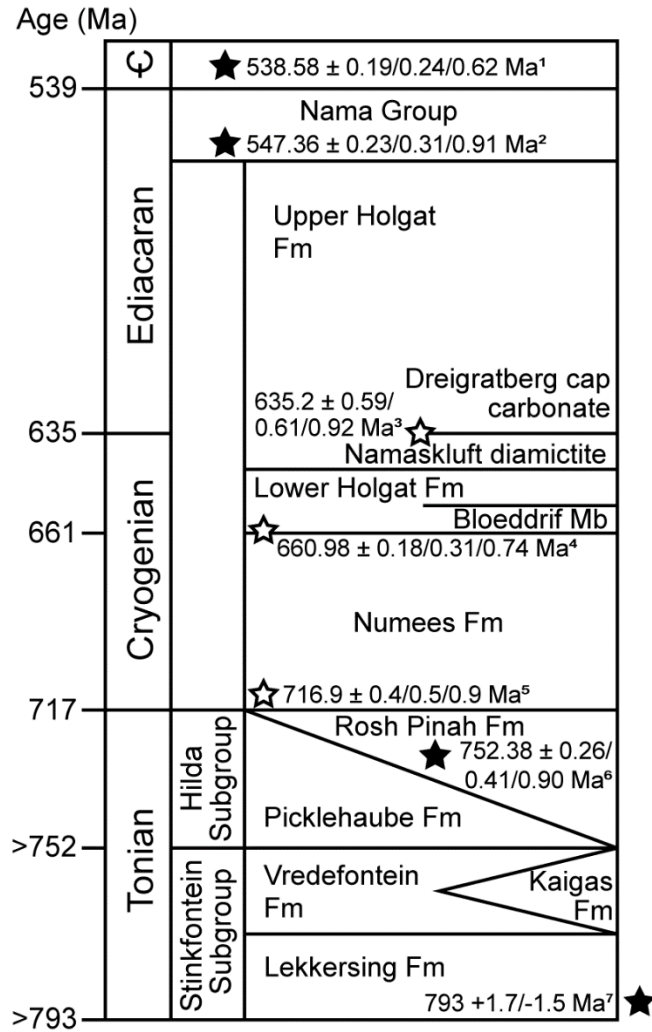
Figure 2. General stratigraphy of the Gariep belt. Filled stars indicate ages obtained within the stratigraphy while unfilled stars indicate ages obtained on other continents that are correlated based on Cryogenian glacial stratigraphy. The filled star to the right of "Lekkersing Fm" refers to the date on the Gannakouriep dikes, which while within the stratigraphy were intrusive and do not give a syn-depositional age. References are [1]Linnemann et al. (2019), [2]Bowring et al. (2007), [3]Prave et al. (2016), [4]Rooney et al. (2020), [5]Macdonald et al. (2017), [6]this study, and [7]Rioux et al. (2010).
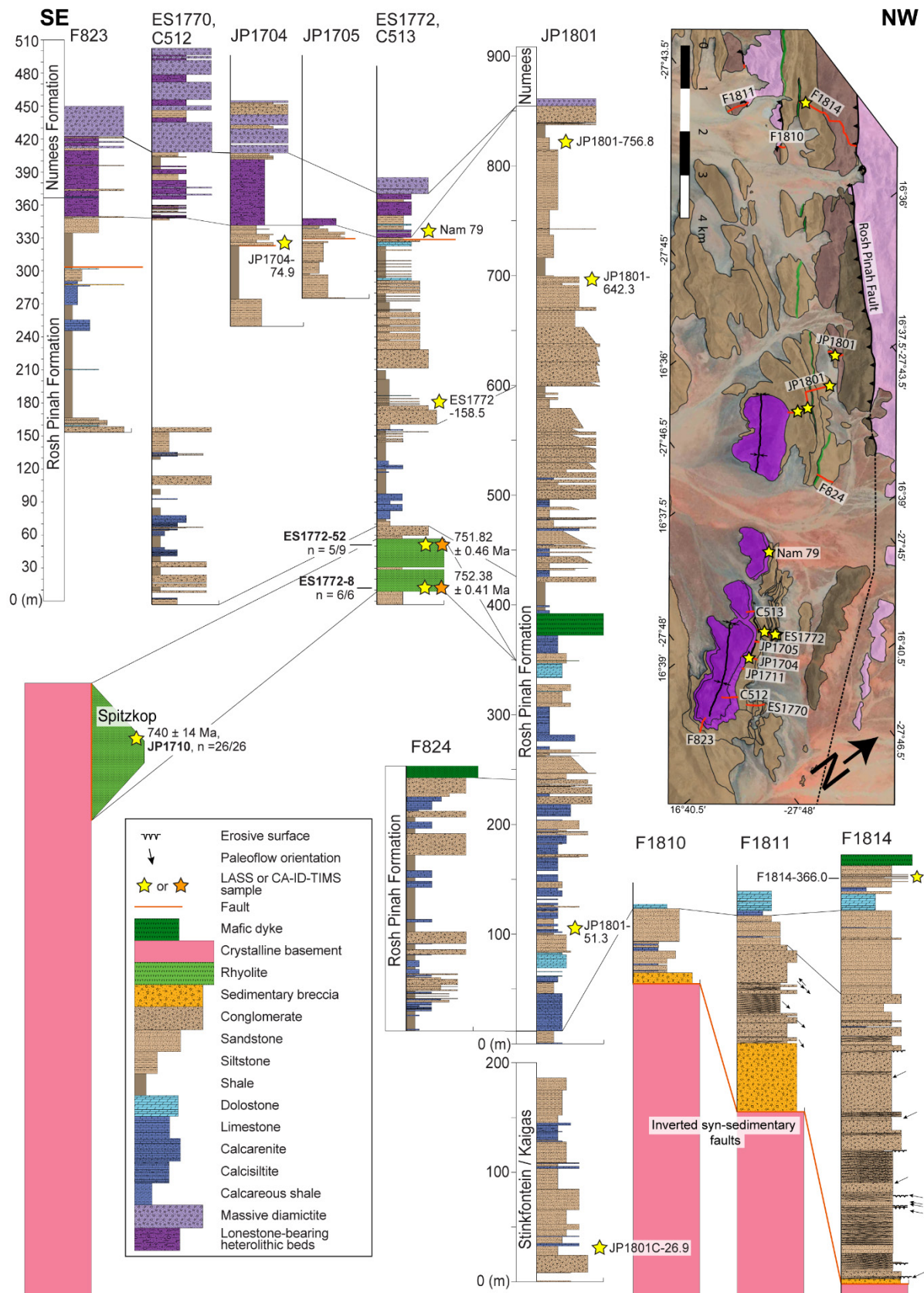
Figure 3. Parautochthonous (west of the Rosh Pinah Fault) stratigraphy of the Port Nolloth Group on farm Trekpoort 96. Sections are ordered left to right from the southeast to the northwest. Locations are labeled and shown in the geologic map in the top right and also outlined in a black box in Fig. 1. Map units are the same as in Fig. 1. The weighted mean ^{206}Pb/^{238}U dates for JP1710, ES1772-8, and ES1772-52 in the figure are shown with Y uncertainties for comparisons between different U-Pb techniques.
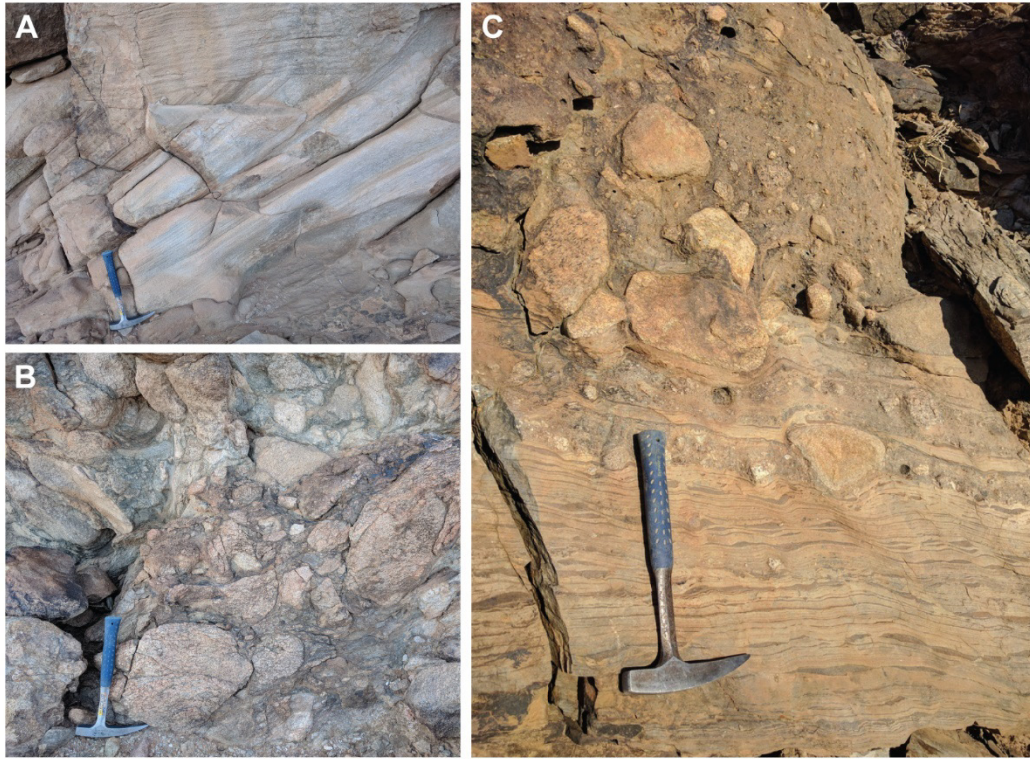
Figure 4. Photographs of Neoproterozoic units from Trekpoort farm. Hammer for scale is 33 cm in length. **A)** Decimeter-scale cross-stratification in Stinkfontein sandstones. **B)** Sedimentary breccia of the Kaigas Fm. **C)** Diamictite of the Numees Fm showing dropstones in laminated diamictite transitioning into massive diamictite above.
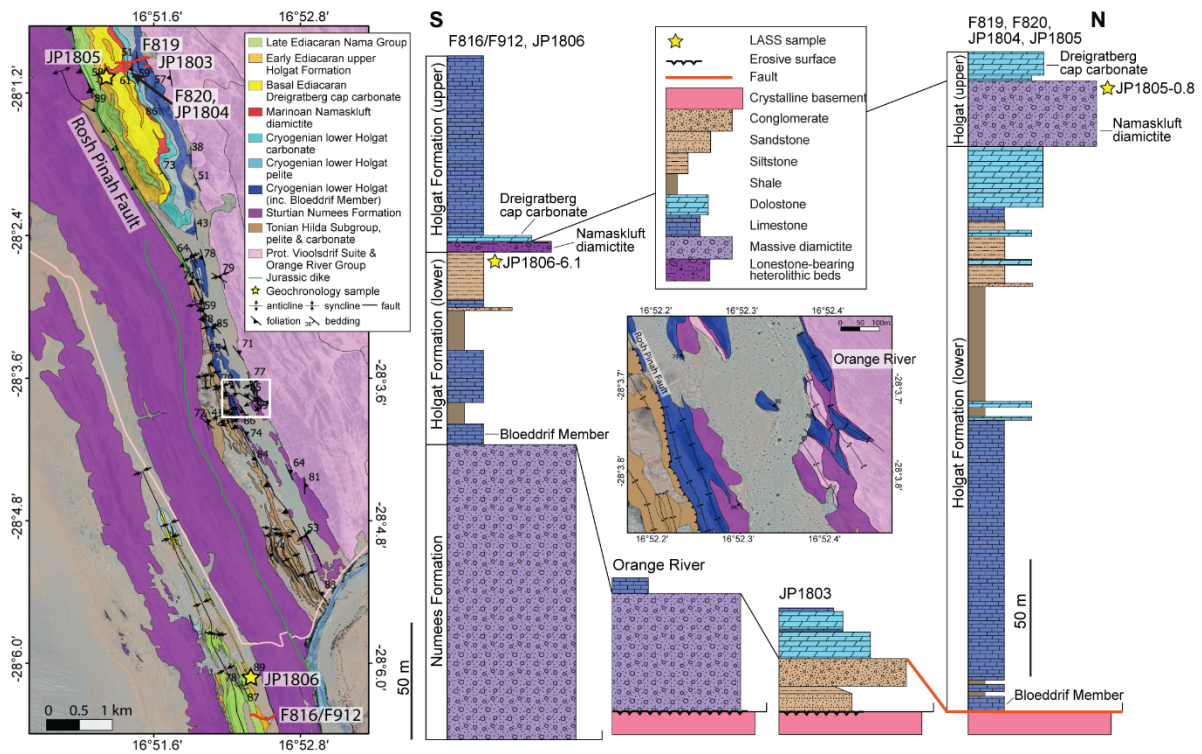
Figure 5. Autochthonous (east of the Rosh Pinah Fault) stratigraphy of the Port Nolloth Group by Orange River. The location of the zoomed-in map is indicated in the regional map (Fig. 1) by a white box and structural symbols used are the same as in Fig. 1. Sections are shown as red lines in the regional map and sample locations are indicated by yellow stars. The zoomed-in map shows in detail the stratigraphic and structural relationships between the Numees diamictite and the Bloeddrif Member on the autochthon and a schematic section is provided for context, labeled "Orange River."
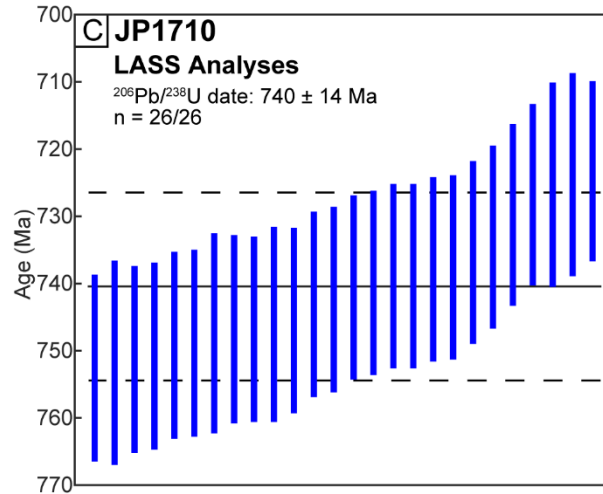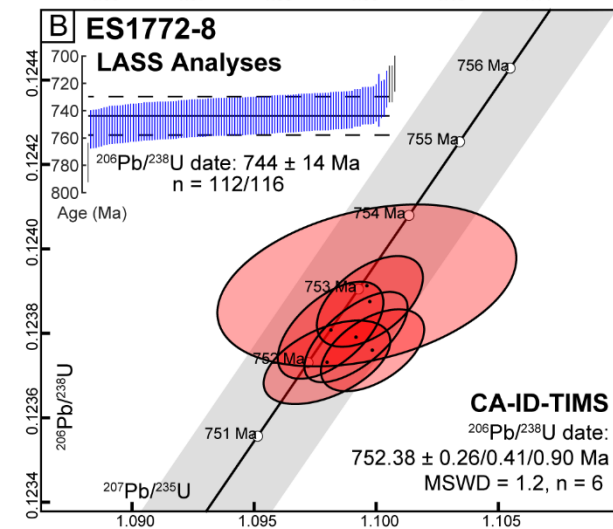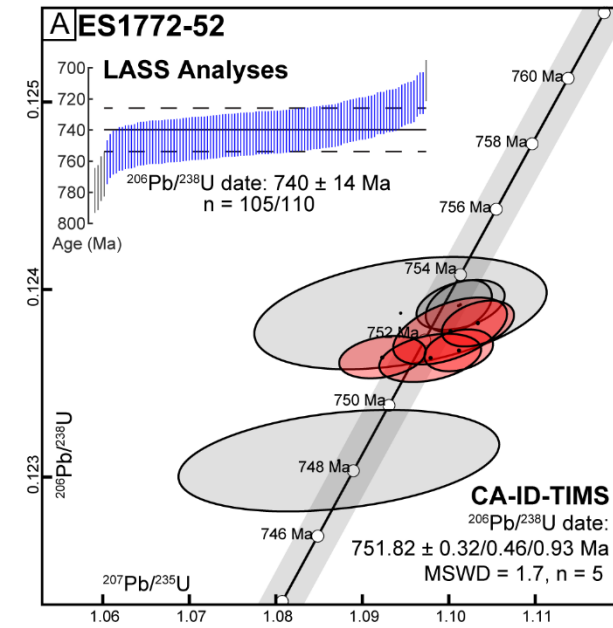
Figure 6. Concordia plots and weighted mean ^{206}Pb/^{238}U dates from LASS and CA-ID-TIMS analyses for samples ES1772-52 (**A**), ES1772-8 (**B**), and JP1710 (**C**, only LASS analyses). For LASS analyses, the plotted vertical bars represent 2s uncertainties for ^{206}Pb/^{238}U analyses and account for systematic uncertainties. Analyses that were more than 10% discordant were not plotted. Blue-colored data were included in the weighted mean calculation while grayed-out analyses are outliers identified using Chauvenet's criterion in IsoplotR (Vermeesch, 2018) that were excluded. The weighted mean is represented by the horizontal black line while the dashed lines indicate the bounds of 2% (2s) propagated from the weighted mean ratio following Horstwood et al. (2016). For CA-ID-TIMS analyses, 2σ sample uncertainties are reported in the form ± X/Y/Z Ma, where X is analytical uncertainty only, Y includes X and tracer calibration uncertainty, and Z includes both tracer calibration uncertainty and decay constant uncertainties for comparison with other isotope systems. Red ellipses show the 95% confidence interval for the analytical uncertainties of each included analysis. Grey ellipses indicate analyses that were excluded from the weighted mean.

JP1805-0.8, n = 55
Namaskluft diamictite,
Orange River

JP1806-6.1, n = 92
Lower Holgat sandstone,
Dreigratberg

Nam 79, n = 63
Numees diamictite,
Trekpoort Farm
(Hofmann et al., 2015)

JP1704-74.9, n = 55
Rosh Pinah siltstone,
Trekpoort Farm

JP1801-756.8, n = 160
Rosh Pinah sandstone,
Trekpoort Farm

JP1801-642.3, n = 135
Rosh Pinah sandstone,
Trekpoort Farm

ES1772-158.5, n = 99
Rosh Pinah sandstone,
Trekpoort Farm

JP1801-51.3, n = 22
Rosh Pinah siltstone,
Trekpoort Farm

F1814-366, n = 150
Stinkfontein sandstone
Trekpoort Farm

JP1801C-26.9, n = 25
Stinkfontein sandstone
Trekpoort Farm

Age (Ma)

500 700 900 1100 1300 1500 1700 1900 2100 2300 2500 2700 2900

Namaskluft
Lower Holgat
Numees Fm
Rosh Pinah Formation
Stinkfontein/Kaigas

Figure 7. Detrital zircon geochronology alongside a composite section showing their approximate stratigraphic positions (refer to Fig. 3 for more detail). Detrital zircon dates are plotted as KDEs in stratigraphic order. Data for sample Nam79 are from Hofmann et al. (2015). The vertical plot lines corresponding to 1100 and 1900 Ma are bolded for easier visual reference between samples.
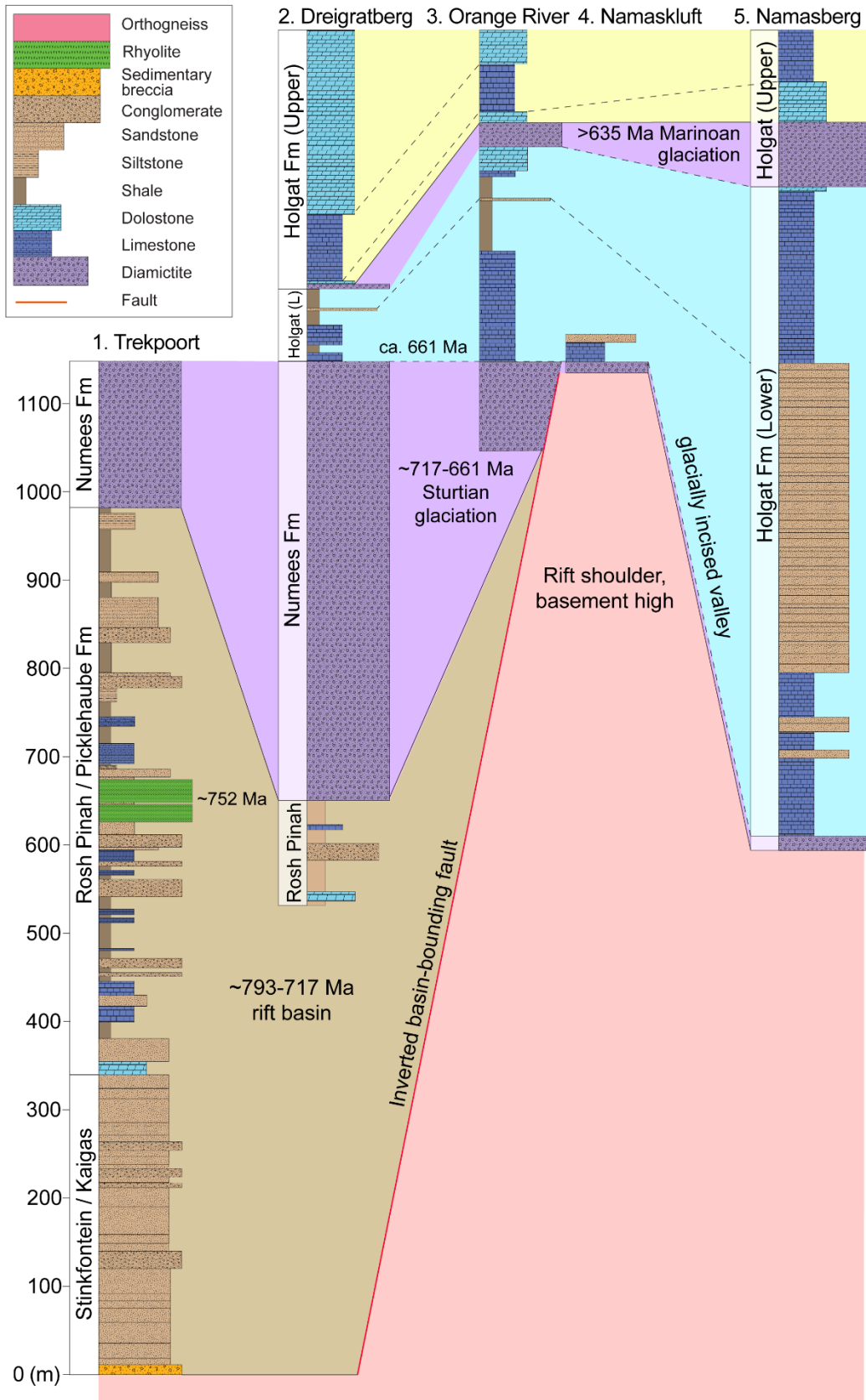
Figure 8. Composite stratigraphic sections spanning the parautochthon to autochthon from Trekpoort to Namasberg (locations indicated by circled numbers in Fig. 1).
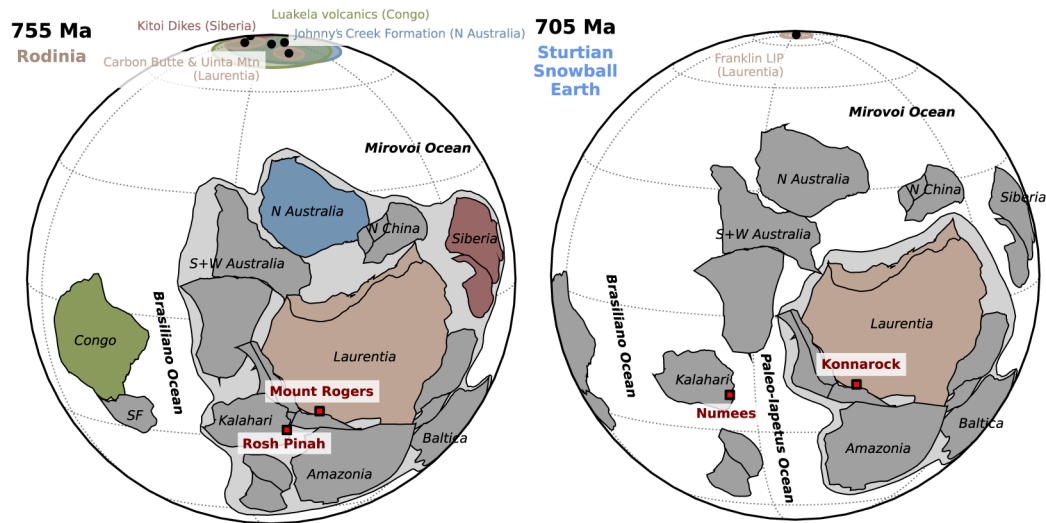
Figure 9. Paleogeographic reconstructions of Rodinia showing the interpreted position of Kalahari relative to Laurentia at two time points: ca. 755 Ma, as Rodinia break-up was initiating, and ca. 705 Ma, as Rodinia rifting was progressing and the Sturtian glaciation was ongoing. These reconstructions contextualize the Rosh Pinah and Numees formations of Kalahari and their potential correlations in the same extensional tectonomagmatic regime as the Mount Rogers and Konnarock formations of Laurentia. Note that the width and position of the AREPA (AREquipa, Pampia, Antofalla) terranes that are shown as the proposed intermediary between Laurentia and Kalahari in Rodinia are uncertain. The reconstruction is modified from Macdonald et al. (2023) and shows continental blocks interpreted to have been conjoined with Laurentia. Continents shown in color are ones with broadly contemporaneous paleomagnetic poles that constrain the continents' paleolatitudes and orientations. These poles are: Luakela Volcanics of Congo (Wingate et al., 2010), Kitoi dikes of Siberia (Pisarevsky et al., 2013), Johnny's Creek Fm of Northern Australia (Swanson-Hysell et al., 2012), Carbon Butte Fm of Laurentia (Eyster et al., 2020), Uinta Mountain Fm

of Laurentia (Weil et al., 2006), and the Franklin Large Igneous Province of Laurentia (Denyszyn et al., 2009).

III. Stratigraphy and geochronology of the Marinoan Snowball Earth deglaciation on the northwest margin of the Kalahari Craton

A. Introduction

Geologic, paleomagnetic, and geochronology studies have provided evidence for two long-lasting, low-latitude Cryogenian Snowball Earth glaciations: the Sturtian (717-661 Ma; Rooney et al., 2015) and the Marinoan (<651-635 Ma; Nelson et al., 2020). Cryogenian glacial deposits are globally ubiquitous and described on every continent, and when the stratigraphy is undisrupted, glacial diamictites are capped by extensive carbonate deposits, consistent with a large flux of alkalinity into the oceans under the extreme greenhouse conditions predicted by the Snowball Earth hypothesis (Hoffman et al., 2017). Geochronology has provided a key test for the hypothesis demonstrating that the glaciations were synchronous and long-lasting (Rooney et al., 2015). However, geochronology has also highlighted differences between the two Snowball glaciations; despite their relatively close occurrence in time, the two Snowball Earth events have distinct sedimentological features and durations. The 56-Myr Sturtian Snowball Earth is associated with iron formations and typically has a condensed, organic-rich cap limestone while the <16-Myr Marinoan Snowball Earth has a pink or yellow peloidal cap dolostone that can include barite crystal fans, tubestone stromatolites, and giant wave ripples (Hoffman et al., 2017).

Ultimately the differences in expression of chemical sediments between the two events could be due fundamentally to timing, with total duration and the rate of deglaciation affecting the sedimentological expression of the two glaciations (e.g., Hoffman et al., 2017). However,

the sparseness of geochronological constraints within stratigraphic sections spanning the glacial deposits have made it difficult to determine how time is distributed in the sedimentary record (e.g., syn-glacial vs. deglacial strata). Climate models have attempted to test different extents and durations of ice cover by simulating ice buildup and stability in response to changes in pCO$_2$ and orbital forcings (Abbot et al., 2013; Benn et al., 2015), but these remain to be grounded in the geological record with rates. The Naukluft Nappes Complex in Namibia provides continuous lateral exposure of Marinoan deposits across several km and includes volcaniclastic strata, providing the opportunity to develop a new, detailed sedimentary facies model and age model for the Marinoan glaciation and deglaciation.

B. Geologic setting

The north and west margins of the Kalahari Craton formed through Tonian rifting from the supercontinent Rodinia (see Ch. 2). These rifts developed into Cryogenian passive margins, capturing the two Snowball Earth periods. On autochthonous sections on the northern margin, Prave et al. (2011) depicted a Cryogenian to early Ediacaran passive margin capped by late Ediacaran foreland deposits of the Nama Group that were metamorphosed by the Cambrian Damara orogeny. Similarly, from autochthonous sections in the Gariep belt, Macdonald et al. (2010) interpreted the western margin as a Tonian to early Ediacaran rifted passive margin with late Ediacaran left-lateral transpressional deformation and late Ediacaran to Cambrian foreland deposition and shortening.

The geology of the Naukluft Nappes was first described in detail by Korn and Martin (1959). The stratigraphy presented here generally follows the revisions to Hartnady's (1978) units by Hoffmann et al. (1995, Miller, 2008). Neoproterozoic units of the Naukluft Nappes

consist of the fine-grained siliciclastics of the Remhoogte Formation; the diamictite-bearing Blässkranz Formation; and dominantly carbonate Tsabisis Formation, followed by the conglomerates and grainstones of the Noab Formation (Fig. 2; Hartnady, 1978; Hoffmann et al., 1995). The interbeds of sandstone, siltstone, and volcaniclastics at the top of the Blässkranz Formation has been named the Tsugaub Volcaniclastic Member by Hoffmann et al. (1995). The Tsugaub Volcaniclastic Member was originally part of Hartnady's (1978) Tsabisis Formation, but because there is no significant change in the continuity of sedimentation, it is included here as part of Blässkranz Formation. These Neoproterozoic units are exposed in the Tsondab and Tsauchab river valleys, where the base of the valley truncates exposure of the Remhoogte Formation. The Noab Formation marks the top of the sequence and the plateau.

Stratigraphic correlations and structure of the Naukluft Mountains were initially thought to reflect "gravity tectonics" and ductile flow (Korn and Martin, 1959). Structural mapping by Hartnady (1978) placed it within the framework of plate tectonic processes of subduction and continental collisions and provided a tectono-stratigraphic model for the nappes. The Naukluft Nappe Complex is preserved as a klippe on the younger foreland deposits of the Nama Group (Fig. 1; Martin, 1974; Martin et al., 1983). A K/Ar muscovite date of ~530 Ma from metapelites at the base of the Naukluft Nappe complex gives a minimum age for the earliest phase of thrusting (Ahrendt et al., 1978; Gray et al., 2008). This age agrees with geochronology on the base of Nama Group foreland deposition, which has been dated using CA-ID-TIMS to 547.36 ± 0.23/0.31/0.91 Ma (Grotzinger et al., 1995; Bowring et al., 2007). The basal shear surface of the Naukluft Nappe is strongly foliated with C-S fabrics

indicating top to the SE transport (Gray et al., 2008). Total tectonic transport is estimated between 60-80 km to the SE (Goscombe et al., 2017). The allochthonous units of the Naukluft Nappes can be correlated with units from the Hakos zone (Hoffmann, 1989), preserving Neoproterozoic slope to distal margin deposits of the northwest corner of the Kalahari Craton.

C. Methods

1. Geological mapping and stratigraphy

Stratigraphic sections were measured in conjunction with geological mapping between 2017-2019 (Figs. 3, 4). Sections were measured with a meter-stick and unit thicknesses were measured to the nearest 10 cm. Sections usually begin either at the start of rock exposure or at the base of the limestone conglomerates near the top of the Remhoogte Formation and were measured to the base of the transgressive Marinoan cap carbonate of the Tsabisis Formation. Section locations are given in Table S1. Units were broken out based on grain size, mineralogy, and bedforms. Features such as matrix and clast compositions; frequency, size, and roundedness of clasts; stratification; sorting; bedding; foliation; and color were noted for each unit if applicable.

2. Geochronology methods

Three volcaniclastic samples at different horizons within the Tsugaub Member and a number of sandstone units were processed for detrital zircon geochronology. Coordinates for the stratigraphic sections that these samples were taken from are included in Table S1. Since the aim was to obtain the youngest populations in the samples, faceted, smaller grains were

preferentially selected and made up the majority of the grains analyzed. A small selection of larger and more rounded grains were included for each sample as well. The zircon grains for each sample were mounted in epoxy and polished to expose grain cores. The grains were first screened for trace elements and preliminary dates on the Thermo Scientific X-Series II quadrupole-ICPMS (Q-ICPMS) and New Wave Research UP-213 laser ablation system at Boise State University (BSU) in 2017-2018. Comparisons of the geochemistry of the grains were then used to guide grain selection for CA-ID-TIMS work to maximize the probability of isolating distinct young age populations. All CA-ID-TIMS analyses were done at BSU between 2017-2019.

Additional detrital zircon geochronology was done using the LASS system at UCSB in 2019 following the procedures in Kylander-Clark et al. (2013) and Kylander-Clark (2017). Data were reduced using iolite4 software (Paton et al., 2010, 2011) and IsoplotR (Vermeesch, 2018). Standard error (2s) was propagated using methods described in Paton et al. (2010) and Horstwood et al. (2016).

Detailed analytical methods for LASS and CA-ID-TIMS analyses are available in the Supplementary Materials. Complete Pb and U isotopic data are given in Tables S2 and S3. Uncertainties on the CA-ID-TIMS weighted mean dates are given as 2σ and in the $\pm$ X/Y/Z Ma format, where X is the internal error based on analytical uncertainties only, Y includes X and the tracer calibration uncertainty, and Z includes Y plus the ^{238}U decay constant uncertainty of Jaffey et al. (1971).

D. Results

1. Neoproterozoic stratigraphy of the Naukluft Nappes

Maps and stratigraphy are presented in Figs. 3 and 4. Exposure of the Neoproterozoic units in the Naukluft Nappes begins with the Remhoogte Formation, which consists of >700 m of green argillite. Centimeter-scale grading from fine-grained sandstone and siltstone to argillite is locally apparent. The basal exposures of the Remhoogte Formation show evidence of structural repetition but lack good marker units to constrain the total shortening (Hartnady, 1978). Near the top of the formation, pebble- to cobble- sized carbonate clasts appear along with <30 cm-thick beds of medium- to coarse-grained lithic arenite. The top of the formation is marked by at least two cliff-forming carbonate conglomerates, one limestone and one dolostone, which are both several meters thick. A single granite lonestone was observed in one limestone conglomerate unit in section JP1904 (Fig. 5A), but otherwise no other exotic clasts were observed in the units of the Remhoogte Formation.

The Blässkranz Formation sits unconformably on top of the Remhoogte Formation, with the surface between the two formations cutting into the blue limestone conglomerate unit in the contact exposed on the Arbeid Adelt farm but in most places appearing as a paraconformable contact (Fig. 3A; Hoffmann et al., 1995 in Miller, 2008). Where it sits unconformably on top, pebbles of the underlying blue limestone conglomerate unit can be found in the basal siltstone and sandstone of the Blässkranz Formation. The base of the Blässkranz Formation locally includes granite pebbles but is otherwise clast-poor argillite. Up-section, the argillite becomes interbedded with thin (typically <30 cm) sandstone units

which is followed by thicker, cm-scale cross-bedded sandstone beds before returning to green argillite. Clast density and size generally increase in the upper parts of the formation. Cobble-to boulder-sized granite and quartzite clasts can also be found in the Blässkranz Formation but typically only appear in upper portions of the sections. Clast compositions are dominated by carbonates; throughout the Blässkranz Formation are horizons of poorly sorted, largely clast-supported, heterogeneous mixtures of carbonates, including blue limestones, oolitic grainstone, and dolomite in a tan, dolomite matrix (Fig. 5B, 5C). Dark brown-red weathering sandstone beds drape the carbonate conglomerate units and preserve ripple cross-lamination.

Sandstone units also appear at the top of the Blässkranz Formation and are interbedded with purple siltstone and green volcaniclastic units (Fig. 5D), forming the Tsugaub Member (Hoffmann et al., 1995). Climbing ripple cross-lamination can also be seen in some of the upper sandstone units. Sandstone units typically have no clasts or are clast-poor but the interbedded green argillite can contain clasts and the purple siltstone beds have a wacke texture and include granite clasts. The volcaniclastic beds have a light-green matrix with granules to pebbles of other volcanic and sedimentary units within them. The volcaniclastic beds are poorly sorted but can also show reverse then normal grading in the same bed (Fig. 5D).

The sandstones, siltstones, and volcaniclastics of the Tsugaub Member continue up to the contact with the cap carbonate sequence of the Tsabisis Formation and include large granite boulder clasts (Fig. 5E). In places, the base of the cap carbonate sequence is a massive dolostone matrix with pebble- to cobble-sized clasts of carbonates, siliciclastic rocks, and granites. More commonly, the base of the Tsabisis Formation begins with a finely laminated

dolostone that weathers pink-tan and has low-angle, swaley cross-stratification throughout. Within a few meters, bedding becomes more planar and parallel but maintains its mm-scale laminations. Thin partings of purple shale can be seen between dolostone beds. These purple shale beds increase in thickness up-section.

There are occasional intervals of imbricated, intraclast, edgewise conglomerate in the dolostone, interbedded with the purple shales. These intervals also include cross-stratified sandstone beds. Mineralogy changes above this sequence from dolostone to interbeds of purple slate and light-pink, finely laminated micritic limestone. The purple slate interbeds gradually disappear up-section and are replaced by occasional beds of planar laminated siltstone and fine-grained sandstone. Up section, the thin beds of intraclast, dolostone conglomerate and interbeds of finely laminated limestone marl and siltstone and fine-grained sandstone transition into the wavy-laminated, blush-pink to white dolomite grainstone of the Noab Formation. This contact is commonly unconformable with units of the Noab Formation resting directly on all of the underlying stratigraphy (Fig. 5F).

2. Geochronology and geochemistry

To constrain sedimentation timing and rates, volcaniclastic horizons at different distances from the base of the cap carbonate sequence in the Tsabisis Formation were processed for geochronology. Sample F828-210.5 was collected at 38.5 m below the base of the cap sequence, JP1713-193.7 was 2.3 m below the base of the cap sequence, and JP1715-187.9 was collected 9.6 m below the base of the cap sequence. Kernel density estimates (KDEs) are plotted for the volcaniclastic samples in Fig. 6 and show a significant young peak of grains at ~600-700 Ma in addition to peaks at 2.0 Ga, 1.8 Ga, and between 1.4-1.0 Ga.

Since sample F828-210.5 was the farthest below the cap sequence and could provide age constraints on a greater portion of the stratigraphic section, it was the main focus of CA-ID-TIMS analyses. A number of analyses produced dates that were reversely discordant or extremely imprecise due to both high common Pb and low radiogenic Pb amounts; these analyses were excluded from any mean date considerations. CA-ID-TIMS dates for F828-210.5 grains ranged between ~637-635 Ma and formed a single population with a weighted mean date of $^{206}Pb/^{238}U$ of 635.84 ± 0.22/0.29/0.71 Ma (2σ uncertainty, n = 11, MSWD = 1.62) (Fig. 6). Dates for grains in JP1713-193.7 ranged from ~716 Ma to 636 Ma with the youngest grain producing a $^{206}Pb/^{238}U$ date of 635.76 ± 0.79/0.81/1.04 Ma. CA-ID-TIMS dates for JP1715-187.9 grains ranged between ~714-635 Ma. The youngest three grains that overlapped within uncertainty produced a weighted mean $^{206}Pb/^{238}U$ date of 635.93 ± 0.56/0.59/0.88 Ma.

KDEs are also plotted for siliciclastic samples from near the base of the Blässkranz Formation and the top of the Remhoogte Formation (Fig. 7). The samples show similar peaks in zircon dates to the volcaniclastic units at around 1.4-1.35, 1.2, and 1.1 Ga, but do not show the young peak between 600-700 Ma.

Zircon in each of the volcaniclastic samples came from a variety of source rocks and tectonic settings. U/Yb and Nb/Yb ratios in zircon have been used to determine the tectonic setting of magmatism; U/Yb values <0.1 are more characteristic of MORB mantle (Grimes et al., 2007). U/Yb vs. Nb/Yb for Naukluft volcaniclastic samples plot mostly below the "mantle-zircon array" range determined by Grimes et al. (2015) (Fig. 8). All samples show

some populations close to this boundary line with a few grains from sample JP1715-187.9 that plot within the magmatic arc range.

E. Discussion

1. Interpretation of the U-Pb data

The 1.4-1.35, 1.2, and 1.1 Ga peaks seen in the detrital zircon data are periods of major accretionary phases on the Kalahari Craton (Fig. 6, 7; Hanson et al., 2004, 2006; Miller, 2012). The 1.4-1.35 Ga dates correspond to intraplate alkaline magmatism, while the 1.2-1.1 Ga dates are associated with accretion of the Namaqua-Natal belt onto the Kalahari Craton (Hanson et al., 2006; Miller, 2012). The 1.1 Ga dates are likely from rocks associated with the Umkondo LIP (Hanson et al., 2004, 2006). The other smaller peaks in zircon dates between 2.0-1.7 Ga could be sourced from the Richtersveld Subprovince (Miller, 2012). The lack of younger grains until the appearance of volcaniclastic units near the top of the Blässkranz Formation suggests that the basin was proximal and receiving input from the Kalahari Craton but largely passively rifting and subsiding, indicated by the appearance of carbonate debris flows throughout the stratigraphy with no associated volcanism.

The three dated volcaniclastic horizons from the Tsugaub Member near the top of the Blässkranz Formation contained grains with dates of ~636 Ma with overlapping uncertainties (Fig. 6), despite ranging between 2.3 m to 38.5 m from the base of the cap carbonate sequence, which has been dated globally at ~635-636 Ma (Hoffman et al., 2017). Thin section petrography of the volcaniclastic samples revealed a wide variety of carbonate, igneous, and siliciclastic clasts in a volcanic matrix with trachytic textures (Fig. 6). Some samples had

93

examples of partially resorbed and embayed quartz phenocrysts. Although the volcaniclastic units involve some degree of reworking, the high energy nature of these deposits require rapid and local deposition; therefore, our youngest CA-ID-TIMS dates are interpreted to reflect deposition ages. The new geochronological constraint on the section firmly establishes the diamictite and cap carbonate as Marinoan equivalents.

Of the collected volcaniclastic beds, sample F828-210.5 is the farthest (38.5 m) from the base of the cap carbonate and has a maximum depositional age of $635.84 \pm 0.22/0.29/0.71$ Ma (2σ, MSWD = 1.62, n = 11). The current highest precision age constraint on the cap carbonate above is a U-Pb concordia age of 635.23 ± 0.57 Ma from the Doushantuo Formation in South China (Condon et al., 2005). When the three most concordant analyses from the sample are considered, a weighted mean $^{206}Pb/^{238}U$ date of 635.26 ± 0.58 Ma (MSWD = 0.15) can be calculated. Since both studies used the same EARTHTIME tracer for U-Pb calibration, the dates can be compared using "X" uncertainties and overlap within uncertainty (Fig. 9). Sedimentation of the last ~40 m of the section before deglaciation occurred within the uncertainty on the age constraints of these samples. While sediment accumulation rates for the Cryogenian Snowball deposits are proposed to be as much as 15 times slower than Phanerozoic glaciomarine deposition possibly due to extremely cold and dry conditions inhibiting erosion (Partin and Sadler, 2016), deposition of the upper 40 m within timespans on the order of 10^5 yrs fall much closer to typical Phanerozoic values and would be more consistent with a margin where ice was able to advance and retreat. This portion of the stratigraphy, marked by a change to sand-sized background sedimentation, wacke textures, and boulder dropstones, reflects the deglaciation interval of a Snowball Earth event.

High-precision CA-ID-TIMS geochronology is still not precise enough to determine the deposition rates of the cap carbonate sequence, which has been estimated to be deposited within a few kyr based on oceanographic models and sedimentology (Hoffman et al., 2017; Myrow et al., 2018).

2. Sedimentary and tectonic interpretations

Constraining the distribution of time captured by a stratigraphic record is essential to interpreting changes in paleoenvironments. This is particularly true for Cryogenian glacial deposits that have alternatively been interpreted to record glaciation or deglaciation. In sections that lack ash beds and other age controls, elapsed time must be determined from the sedimentary units and features observed.

The surface between the Remhoogte Formation and the Blässkranz Formation is locally unconformable, but is conformable in many places as an onlapping surface. On farm Arbeid Adelt (Fig. 3A), the limestone conglomerate unit at the top of the Remhoogte Formation distinctly changes dip to the east where the unconformity surface is exposed. The units directly above the limestone conglomerate member follow the same dip change and thicken to the east from the erosional surface and then become conformable with a toplapping surface and unit. The granite lonestone in the limestone conglomerate member suggests that ice was already present. These conglomerates are interpreted as debrites marking the glacioeustatic falling-stand wedge and onset of the Marinoan glaciation. This interpretation is supported by carbon isotope stratigraphy through these horizons (Fig. S1, Table S4) which preserve the Trezona isotope excursion. The Trezona carbon isotope excursion is also preserved in falling-stand wedge deposits in the Franni-aus Formation of Namibia (Hoffman,

2011), and the Trezona Formation of Australia, which also preserves rare dropstones (Rose et al., 2012).

The poorly sorted carbonate conglomerate beds with sandstone drapes that appear throughout the Blässkranz Formation are interpreted to be debris flow deposits. In other parts of the section, thin sandstone beds showing either planar bedding or small (decimeter-scale) hummocky cross-stratification followed by thicker sandstone beds that may show crossbedding are likely turbiditic (i.e., Bouma B and C), with the green argillite representing continuing background silt and clay sedimentation. Repeated debrites within graded beds are characteristic of a slope environment below the grounding-line wedge (Miall, 1985; Eyles et al., 1985; Miller, 1996). Clast-rich, massive diamictites in the Blässkranz Formation are interpreted as synglacial sediment gravity flows or flow till deposition. A similar sequence of lithologies has been described in Australia in the Trezona and Elatina formations of the Adelaide Rift Complex (Rose et al., 2012); the Trezona Formation records continuous deposition during a global eustatic sea level fall and subsequent subaerial exposure of carbonate platforms. The overlying synglacial Elatina Formation records debris flows and turbidites in sections that capture more distal slope facies (Rose et al., 2012), like the Blässkranz Formation. Near the top of the Blässkranz Formation, the change in background sedimentation from fine-grained argillite to medium- to coarse-grained siliciclastic rocks is interpreted to reflect local base-level rise at the beginning of deglaciation, and the presence of larger, boulder clasts provide evidence of ice-rafted debris (IRD). Discrete clast-rich horizons in the diamictite could represent individual melt-out events. Deglaciation continues through the appearance of the cap carbonate sequence within the Tsabisis Formation, with exotic

granite clasts in the basal dolostone matrix indicating continuous and rapid deposition (e.g., Hoffman and Macdonald, 2010).

Dolomites in the Noab Formation of the Kudu Nappe conformably overlie the Tsabisis Formation in some sections while cutting out stratigraphy in others, indicating that the Kudu Nappe is younger than the Northern Pavian Nappe and may be sliding on a detachment surface as opposed to being thrust on top (Hoffmann et al., 1995; Morris and Grotzinger, 2023; Fig. 1). The limited displacement on this contact was noted by Hoffmann et al. (1995), who also suggested that the Northern Pavian and Kudu nappes were thrust as one panel in the same deformational stage during the emplacement of the Naukluft Nappes.

Reverse and normal grading in volcaniclastic pebble conglomerate mass flow deposits near the top of the Blässkranz Formation demonstrate volcanic input from nearby, but no Neoproterozoic arc has been described on either the Kalahari or Congo cratons. Geochemical data for zircon grains from the Naukluft volcaniclastic deposits show mixed populations of juvenile to evolved magmatism through the crust (Fig. 8), but most of the grains fall below the line differentiating predominantly arc magmatism from mid-ocean ridge magmatism, which tends to have lower values of U/Yb relative to Nb/Yb (Grimes et al., 2015), supporting the interpretation of a reactivated rift setting.

3. Reactivation of the margin and volcanism-driven deglaciation

Our geochronology demonstrates that the top ~40 m of the Blässkranz Formation was deposited within uncertainty of the age of the Marinoan cap, indicating that deglaciation was rapid and started by 635.84 ± 0.22/0.29/0.71 Ma. CA-ID-TIMS analyses on zircon from a mudstone sample in the Cottons Breccia of Tasmania, Australia, within 0.7 m of the cap

carbonate, produced a weighted mean $^{206}Pb/^{238}U$ date of 636.41 ± 0.34/0.45/0.80 Ma (Calver et al., 2013). Additionally, an ash sample taken from the Ghaub Formation on the Swakop terrane in central Namibia ~30 m below the contact with the Marinoan cap carbonate produced a CA-ID-TIMS weighted mean $^{206}Pb/^{238}U$ date of 635.21 ± 0.59/0.61/0.92 Ma (Prave et al., 2016). These studies also used the EARTHTIME tracer calibration and can be directly compared to this study using "X" uncertainties. Our date for the Naukluft volcaniclastics is closely coincident with these other samples (Fig. 9). The coincidence of magmatic zircon ages indicate that several different margins were active at the same time, at ~636 Ma.

The apparent widespread volcanism may have been a contributing factor in the shorter duration of the Marinoan Snowball Earth relative to the Sturtian (e.g., Lan et al., 2022). It has been proposed that ice loading can significantly affect the rate of volcanism on an active margin; ice loading would suppress volcanism during an extensive glaciation, but a period of melting and ice retreat would unload the margin and result in an increase in volcanism, producing ash and dust that would reduce the albedo of existing ice cover and cause further ice retreat in a feedback cycle until deglaciation is complete (Huybers and Langmuir, 2009). While atmospheric CO_2 requires millions of years to reach the estimated threshold for deglaciation and only becomes more challenging to build up over time as sinks like seafloor weathering consume CO_2 (Brady and Gíslason, 1997; Coogan and Gillis, 2013; Gernon et al., 2016; Hoffman et al., 2017), changing Earth's surface albedo through volcanism can drastically and quickly decrease the threshold to deglaciation by orders of magnitude (Abbot and Halevy, 2010; Le Hir et al., 2010; Hoffman et al., 2017). Volcanism as a mechanism for

driving rapid Snowball deglaciation (e.g., Lan et al., 2022) is consistent with our geochronology.

The long duration for the Sturtian could help explain why the Sturtian cap sequence is so condensed relative to the Marinoan—the process of building up enough CO_2 in the atmosphere to reach deglaciation thresholds likely meant that ice sheets were experiencing radiative forcings from CO_2, and land ice would have already retreated and sea levels responded partially before the deposition of the cap carbonate with the collapse of sea ice (Benn et al., 2015; Hoffman et al., 2017). Any signal of transgression in the sedimentary record would have been more distributed over time than the transgression following a rapid deglaciation due to volcanism.

F. Conclusions

Mapping and measuring stratigraphic sections in the Naukluft nappes allows for the identification of separate phases of a Snowball glaciation, starting with the first appearance of ice and base-level fall represented by the appearance of massive carbonate debrites with rare granite lonestones in an otherwise clast-free green argillite. The first appearance of lonestones in the green argillite above these carbonate mass flows is interpreted to reflect local ice growth. Syn-Snowball deposition is recorded by thin-bedded turbidites with minor debrites and flow tills. The beginning of deglaciation can be identified through the coarsening in background sedimentation and the appearance of volcaniclastic deposits and boulder-sized dropstones. A date of 635.84 ± 0.22/0.29/0.71 Ma on a volcaniclastic sample near the top of the Blässkranz Formation overlaps with existing age constraints on the Marinoan cap carbonate. The appearance of a ~636-640 Ma peak in detrital zircon spectra (Fig. 6, Table S2)

indicates a reactivation of the margin and the coincidence in age with volcanism elsewhere on the Swakop terrane, in Tasmania, and in South China supports widespread volcanism at the time, which may have contributed to a shorter Marinoan glaciation relative to the Sturtian.

G. Acknowledgments

H. References

Abbot, D.S., and Halevy, I., 2010, Dust aerosol important for snowball earth deglaciation: Journal of Climate, v. 23, p. 4121–4132, doi:10.1175/2010JCLI3378.1.

Abbot, D.S., Voigt, A., Li, D., Hir, G. Le, Pierrehumbert, R.T., Branson, M., Pollard, D., and Daniel, D.D., 2013, Robust elements of Snowball Earth atmospheric circulation and oases for life: Journal of Geophysical Research Atmospheres, v. 118, p. 6017–6027, doi:10.1002/jgrd.50540.

Ahrendt, H., Hunziker, J.C., and Weber, K., 1978, Age and degree of metamorphism and time of nappe emplacement along the southern margin of the Damara Orogen/Namibia (SW-Africa): Geologische Rundschau, v. 67, p. 719–742, doi:10.1007/BF01802814.

Benn, D.I. et al., 2015, Orbitally forced ice sheet fluctuations during the Marinoan Snowball Earth glaciation: Nature Geoscience, v. 8, p. 704–707, doi:10.1038/ngeo2502.

Bowring, S.A., Grotzinger, J.P., Condon, D.J., Ramezani, J., Newall, M.J., and Allen, P.A., 2007, Geochronologic constraints on the chronostratigraphic framework of the Neoproterozoic Huqf Supergroup, Sultanate of Oman: American Journal of Science, v. 307, p. 1097–1145, doi:10.2475/10.2007.01.

Brady, P. V., and Gíslason, S.R., 1997, Seafloor weathering controls on atmospheric CO2 and global climate: Geochimica et Cosmochimica Acta, v. 61, p. 965–973, doi:10.1016/S0016-7037(96)00385-7.

Calver, C.R., Crowley, J.L., Wingate, M.T.D., Evans, D.A.D., Raub, T.D., and Schmitz, M.D., 2013, Globally synchronous marinoan deglaciation indicated by U-Pb geochronology of the cottons Breccia, Tasmania, Australia: Geology, v. 41, p. 1127–1130, doi:10.1130/G34568.1.

Condon, D., Zhu, M., Bowring, S., Wang, W., Yang, A., and Jin, Y., 2005, U-Pb ages from the Neoproterozoic Doushantuo Formation, China: Science, v. 308, p. 95–98, doi:10.1126/science.1107765.

Coogan, L.A., and Gillis, K.M., 2013, Evidence that low-temperature oceanic hydrothermal systems play an important role in the silicate-carbonate weathering cycle and long-term climate regulation: Geochemistry, Geophysics, Geosystems, v. 14, p. 1771–1786, doi:10.1002/ggge.20113.

Eyles, C.H., Eyles, N., and Miall, A.D., 1985, Models of glaciomarine sedimentation and their application to the interpretation of ancient glacial sequences: Palaeogeography, Palaeoclimatology, Palaeoecology, v. 51, p. 15–84, doi:10.1016/0031-0182(85)90080-X.

Gernon, T.M., Hincks, T.K., Tyrrell, T., Rohling, E.J., and Palmer, M.R., 2016, Snowball Earth ocean chemistry driven by extensive ridge volcanism during Rodinia breakup: Nature Geoscience, v. 9, p. 242–248, doi:10.1038/ngeo2632.

Goscombe, B., Foster, D.A., Gray, D., Wade, B., Marsellos, A., and Titus, J., 2017, Deformation correlations, stress field switches and evolution of an orogenic intersection: The Pan-African Kaoko-Damara orogenic junction, Namibia: Geoscience Frontiers, v. 8, p. 1187–1232, doi:10.1016/j.gsf.2017.05.001.

Gray, D.R., Foster, D.A., Meert, J.G., Goscombe, B.D., Armstrong, R., Trouw, R.A.J., and Passchier, C.W., 2008, A Damara orogen perspective on the assembly of southwestern Gondwana: Geological Society Special Publication, v. 294, p. 257–278, doi:10.1144/SP294.14.

Grimes, C.B., John, B.E., Kelemen, P.B., Mazdab, F.K., Wooden, J.L., Cheadle, M.J., Hanghøj, K., and Schwartz, J.J., 2007, Trace element chemistry of zircons from oceanic crust: A method for distinguishing detrital zircon provenance: Geology, v. 35, p. 643, doi:10.1130/G23603A.1.

Grimes, C.B., Wooden, J.L., Cheadle, M.J., and John, B.E., 2015, "Fingerprinting" tectono-magmatic provenance using trace elements in igneous zircon: Contributions to Mineralogy and Petrology, v. 170, p. 1–26, doi:10.1007/s00410-015-1199-3.

Grotzinger, J.P., Bowring, S.A., Saylor, B.Z., and Kaufman, A.J., 1995, Biostratigraphic and geochronologic constraints on early animal evolution: Science, v. 270, p. 598–604, doi:10.1126/science.270.5236.598.

Hanson, R.E. et al., 2006, Mesoproterozoic intraplate magmatism in the Kalahari Craton: A review: Journal of African Earth Sciences, v. 46, p. 141–167, doi:10.1016/j.jafrearsci.2006.01.016.

Hanson, R.E., Crowley, J.L., Bowring, S.A., Ramezani, J., Gose, W.A., Dalziel, I.W.D., Pancake, J.A., Seidel, E.K., Blenkinsop, T.G., and Mukwakwami, J., 2004, Coeval Large-Scale Magmatism in the Kalahari and Laurentian Cratons During Rodinia Assembly: Science, v. 304, p. 1126–1129, doi:10.1126/science.1096329.

Hartnady, C.J.H., 1978, The Structural Geology of the Naukluft Nappe Complex and Its

Relationship to the Damara Orogenic Belt, South West Africa/Namibia: University of Cape Town, 509 p.

Le Hir, G., Donnadieu, Y., Krinner, G., and Ramstein, G., 2010, Toward the snowball earth deglaciation...: Climate Dynamics, v. 35, p. 285–297, doi:10.1007/s00382-010-0748-8.

Hoffman, P.F. et al., 2017, Snowball Earth climate dynamics and Cryogenian geology-geobiology: Science Advances, v. 3, p. 43, doi:10.1126/sciadv.1600983.

Hoffman, P.F., 2011, Strange bedfellows: Glacial diamictite and cap carbonate from the Marinoan (635 Ma) glaciation in Namibia: Sedimentology, v. 58, p. 57–119, doi:10.1111/j.1365-3091.2010.01206.x.

Hoffman, P.F., and Macdonald, F.A., 2010, Sheet-crack cements and early regression in Marinoan (635Ma) cap dolostones: Regional benchmarks of vanishing ice-sheets? Earth and Planetary Science Letters, v. 300, p. 374–384, doi:10.1016/j.epsl.2010.10.027.

Hoffmann, K.H., 1989, New aspects of lithostratigraphic subdivision and correlation of late Proterozoic to early Cambrian rocks of the southern Damara Belt and their correlation with the central and northern Damara Belt and Gariep Belt: Communications of the Geological Society of Namibia, v. 5, p. 59–67.

Hoffmann, K.-H., Saylor, B.Z., Grotzinger, J.P., and Hegenberger, W., 1995, Field guide to the Nama, Witvlei and related basins in southern Namibia, Part A: Witvlei Group and equivalents in the Naukluft Nappe Complex: unpublished.

Horstwood, M.S.A. et al., 2016, Community-Derived Standards for LA-ICP-MS U-(Th-)Pb Geochronology – Uncertainty Propagation, Age Interpretation and Data Reporting: Geostandards and Geoanalytical Research, v. 40, p. 311–332, doi:10.1111/j.1751-908X.2016.00379.x.

Huybers, P., and Langmuir, C., 2009, Feedback between deglaciation, volcanism, and atmospheric CO2: Earth and Planetary Science Letters, v. 286, p. 479–491, doi:10.1016/j.epsl.2009.07.014.

Jaffey, A.H., Flynn, K.F., Glendenin, L.E., Bentley, W.C., and Essling, A.M., 1971, Precision measurement of half-lives and specific activities of 235U and 238U: Physical Review C, v. 4, p. 1889–1906, doi:10.1103/PhysRevC.4.1889.

Korn, H., and Martin, H., 1959, Gravity tectonics in the Naukluft Mountains of South West Africa: v. 70, 1047–1078 p.

Kylander-Clark, A.R.C., 2017, Petrochronology by Laser-Ablation Inductively Coupled Plasma Mass Spectrometry: Reviews in Mineralogy and Geochemistry, v. 83, p. 183–198, doi:10.2138/rmg.2017.83.6.

Kylander-Clark, A.R.C., Hacker, B.R., and Cottle, J.M., 2013, Laser-ablation split-stream ICP petrochronology: Chemical Geology, v. 345, p. 99–112, doi:10.1016/j.chemgeo.2013.02.019.

Lan, Z., Huyskens, M.H., Le Hir, G., Mitchell, R.N., Yin, Q.Z., Zhang, G., and Li, X.H., 2022, Massive Volcanism May Have Foreshortened the Marinoan Snowball Earth: Geophysical Research Letters, v. 49, doi:10.1029/2021GL097156.

Macdonald, F.A., Strauss, J. V., Rose, C. V., Dudás, F.Ö., and Schrag, D.P., 2010, Stratigraphy of the Port Nolloth Group of Namibia and South Africa and Implications for the Age of Neoproterozoic Iron Formations: American Journal of Science, v. 310, p. 862–888, doi:10.2475/09.2010.05.

Martin, H., 1974, Damara rocks as nappes on the Naukluft Mountains, South West Africa, *in* Bull. Precambrian Res. Unit., 15, p. 153–165.

Martin, H., Porada, H., and Wittig, R., 1983, Where lies the root zone of the Naukluft Nappe Complex: Evolution of the Damara Orogen of South West Africa/Namibia, Special Publications, v. 11, p. 199–207.

Miall, A.D., 1985, Sedimentation on an early Proterozoic continental margin under glacial influence: the Gowganda Formation (Huronian), Elliot Lake area, Ontario, Canada: Sedimentology, v. 32, p. 763–788, doi:10.1111/j.1365-3091.1985.tb00733.x.

Miller, R.M., 2008, 13.5.2.9. Naukluft Nappe Complex, *in* The Geology of Namibia: Volume 2, Neoproterozoic to Lower Palaeozoic, p. 13- 317:13-329.

Miller, J.M.G., 1996, Glacial sediments, *in* Sedimentary Processes; Stratigraphy, Facies and Environment, p. 454–483.

Miller, R.M., 2012, Review of Mesoproterozoic Magmatism, Sedimentation and Terrane Amalgamation in Southwestern Africa: South African Journal of Geology, v. 115, p. 417–448, doi:10.2113/gssajg.115.4.417.

Morris, F.K., and Grotzinger, J.P., 2023, Facies and stratigraphy of the basal Ediacaran cap carbonate, Naukluft Mountains, Namibia: Precambrian Research, v. 394, p. 107113, doi:10.1016/j.precamres.2023.107113.

Myrow, P.M., Lamb, M.P., and Ewing, R.C., 2018, Rapid sea level rise in the aftermath of a neoproterozoic snowball earth: Science, v. 360, p. 649–651, doi:10.1126/science.aap8612.

Nelson, L.L., Smith, E.F., Hodgin, E.B., Crowley, J.L., Schmitz, M.D., and Macdonald, F.A., 2020, Geochronological constraints on Neoproterozoic rifting and onset of the Marinoan glaciation from the Kingston Peak Formation in Death Valley, California (USA): Geology, v. 48, p. 1083–1087, doi:10.1130/G47668.1.

Partin, C.A., and Sadler, P.M., 2016, Slow net sediment accumulation sets snowball Earth apart from all younger glacial episodes: Geology, v. 44, p. 1019–1022, doi:10.1130/G38350.1.

Paton, C., Hellstrom, J., Paul, B., Woodhead, J., and Hergt, J., 2011, Iolite: Freeware for the visualisation and processing of mass spectrometric data: Journal of Analytical Atomic Spectrometry, v. 26, p. 2508, doi:10.1039/c1ja10172b.

Paton, C., Woodhead, J.D., Hellstrom, J.C., Hergt, J.M., Greig, A., and Maas, R., 2010, Improved laser ablation U-Pb zircon geochronology through robust downhole fractionation correction: Geochemistry, Geophysics, Geosystems, v. 11, doi:10.1029/2009GC002618.

Prave, A.R., Condon, D.J., Hoffmann, K.H., Tapster, S., and Fallick, A.E., 2016, Duration and nature of the end-Cryogenian (Marinoan) glaciation: Geology, v. 44, p. 631–634, doi:10.1130/G38089.1.

Prave, A.R., Hoffman, K.-H., Hegenberger, W., and Fallick, A.E., 2011, Chapter 15: The Witvlei Group of East-Central Namibia, *in* Arnaud, E., Halverson, G.P., and Shields-Zhou, G. eds., The Geological Record of Neoproterozoic Glaciations, London, The Geological Society of London, p. 211–216.

Rooney, A.D., Strauss, J. V., Brandon, A.D., and Macdonald, F.A., 2015, A Cryogenian chronology: Two long-lasting synchronous neoproterozoic glaciations: Geology, v. 43,

p. 459–462, doi:10.1130/G36511.1.

Rose, C. V., Swanson-Hysell, N.L., Husson, J.M., Poppick, L.N., Cottle, J.M., Schoene, B., and Maloof, A.C., 2012, Constraints on the origin and relative timing of the Trezona δ 13C anomaly below the end-Cryogenian glaciation: Earth and Planetary Science Letters, v. 319–320, p. 241–250, doi:10.1016/j.epsl.2011.12.027.

Spencer, C.J., Yakymchuk, C., and Ghaznavi, M., 2017, Geoscience Frontiers Visualising data distributions with kernel density estimation and reduced chi-squared statistic: Geoscience Frontiers, v. 8, p. 1247–1252, doi:10.1016/j.gsf.2017.05.002.

Vermeesch, P., 2018, IsoplotR: A free and open toolbox for geochronology: Geoscience Frontiers, v. 9, p. 1479–1493, doi:10.1016/j.gsf.2018.04.001.

I. Figures
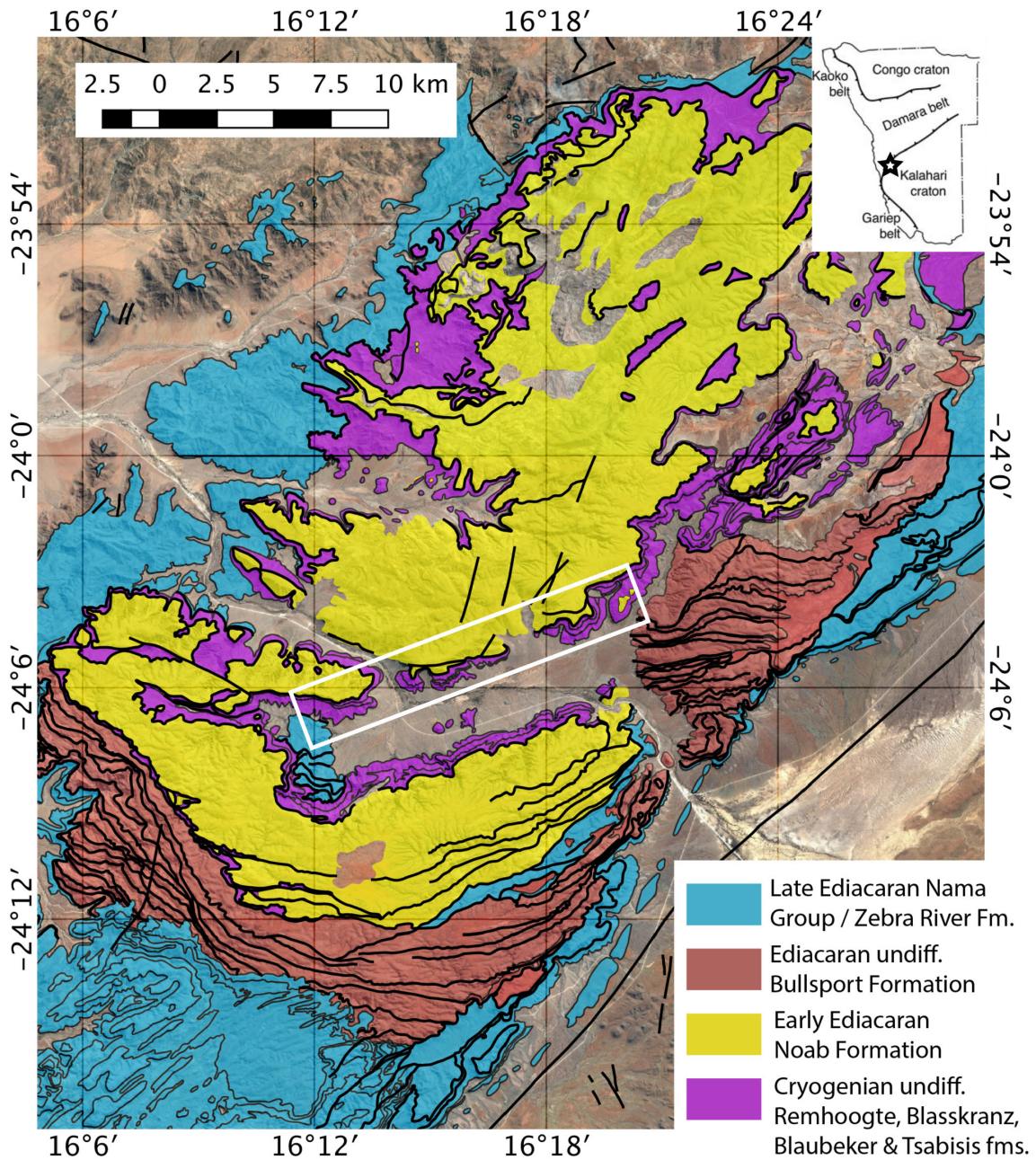
Figure 1. Map of the Naukluft Nappes, modified from Hartnady (1978). The location of the Nappes relative to the rest of Namibia and the Kalahari Craton is indicated in the inset map by the unfilled star. The white rectangle on the geologic map denotes the study area.
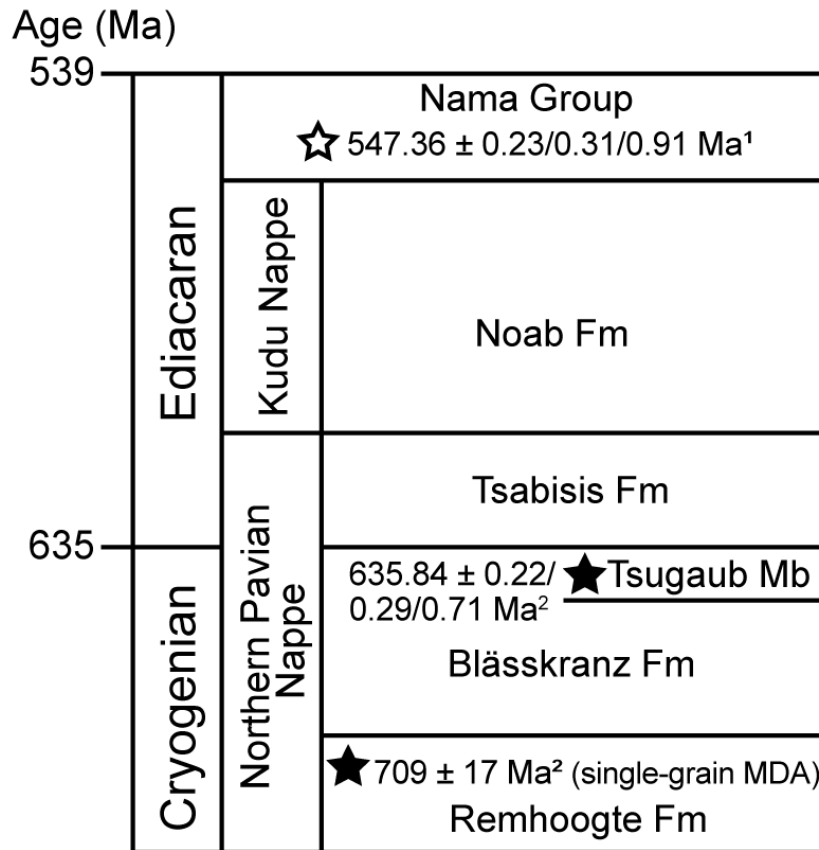
Figure 2. General Cryogenian and Ediacaran stratigraphy of the Naukluft nappes. Filled stars indicate ages obtained within the stratigraphy while unfilled stars indicate ages obtained elsewhere. References are [1]Bowring et al. (2007) and [2]this study.

Noab Fm	Blässkranz Fm	Remhoogte Fm
Dolostone	Red, sandy diamictite	Limestone conglomerate
Tsabisis Fm	Carbonate debris flow, carbonate clasts	Dolostone breccia
Silts and marls	Clast-rich green argillite diamictite	Green argillite
Cap carbonate	Clast-poor green argillite diamictite	
Tsugaub member		
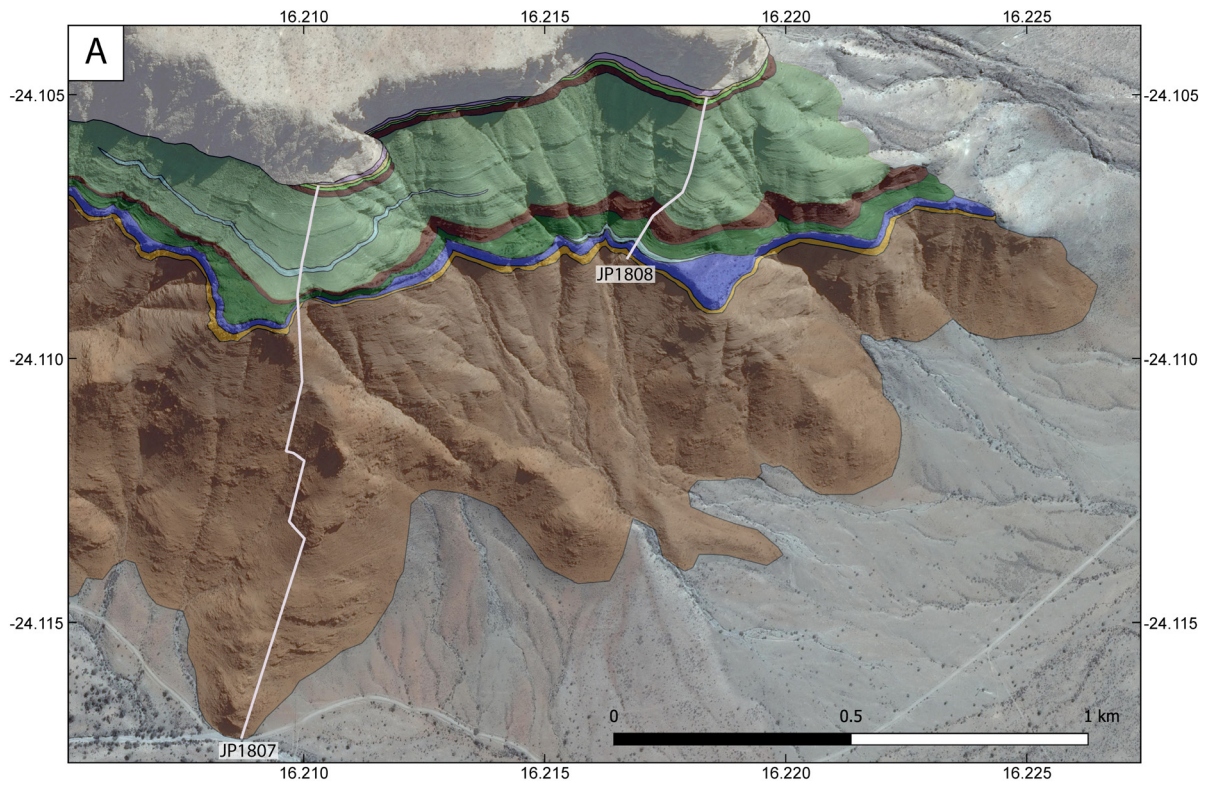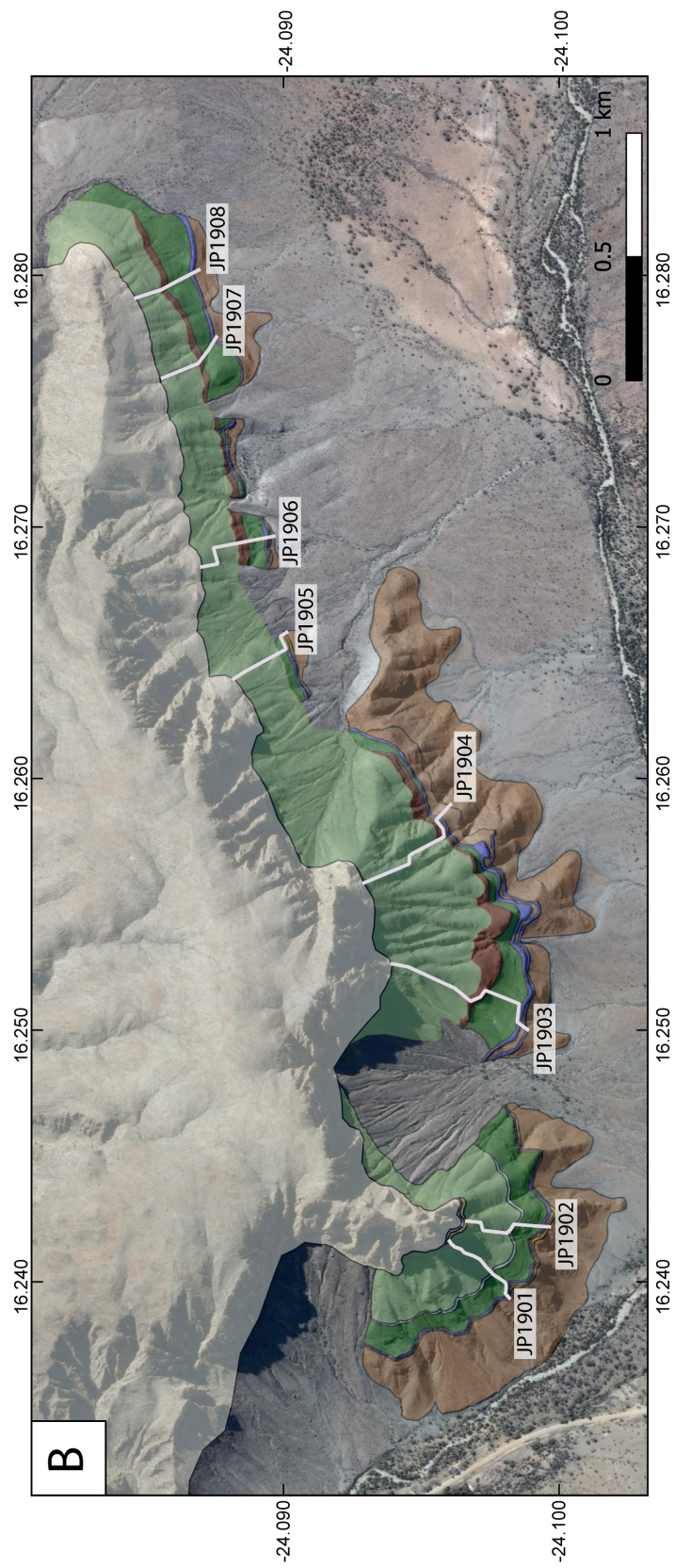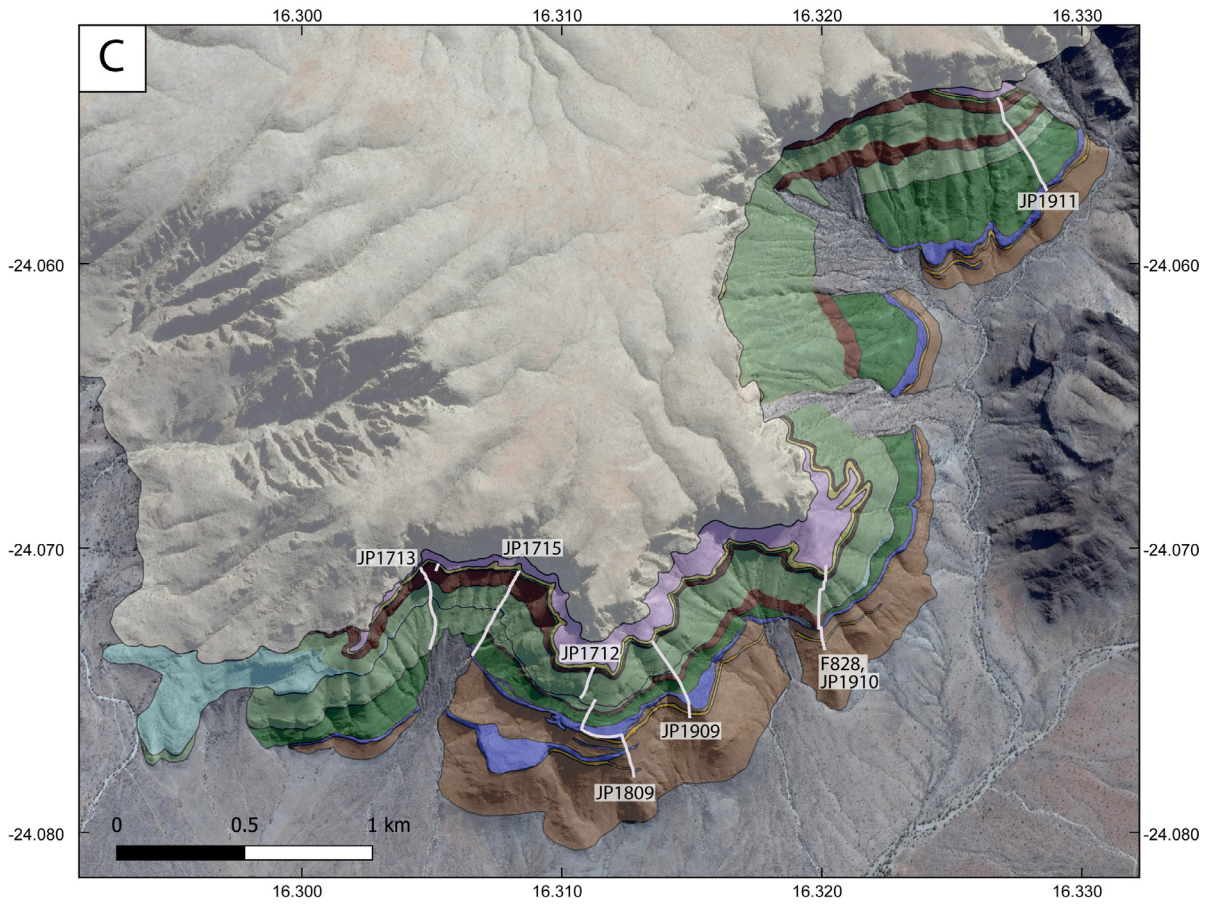
Figure 3. Geologic maps of Neoproterozoic units from farm Arbeid Adelt to the eastern boundary of farm Blässkranz from the panel indicated in Fig. 1 by the white rectangle. Maps are labeled **A**, **B**, and **C** from west to east. White lines indicate locations of measured sections. The youngest unit, the dolostone of the Noab Formation, sits on top of all Cryogenian units on a detachment surface, variably cutting down into the units below it.

Legend

Matrix
- ■ Olive green
- ■ Light brown
- ■ Red
- ■ Tan

- ■ Volcanic
- ■ Calcisiltite
- ■ Micrite-rhythmite
- ↯ Aragonite fans

Volcaniclastic shale and sandstone interbeds	Stratified clast-rich diamictite	Interbedded sandstone and siltstone
Quartzite	Stratified clast-poor diamictite	Calcareous silt/interbedded silt and limestone
Carbonate breccia with carbonate matrix	Bedded sandstone	Limestone
Conglomerate	Calcareous sand	Dolostone
Diamictite with conglomeratic lenses	Dolomitic sand	Nodular carbonate
Clast-poor diamictite	Siltstone	Interbedded shale and silty limestone

Figure 4. Measured stratigraphic sections of the Remhoogte, Blässkranz, and Tsabisis formations. Locations are noted on the maps in Fig. 3. JP1807 started at the base of exposure of the Remhoogte and is cropped to only show the last ~200 m of the green argillite. Other sections started at or were dropped down to the top of the Remhoogte Formation, defined in this study as the top of the last blue limestone conglomerate unit. Sections end at the base of the cap carbonate member of the Tsabisis Formation. Volcaniclastic samples dated in this study are marked on the sections with a star and sample name.
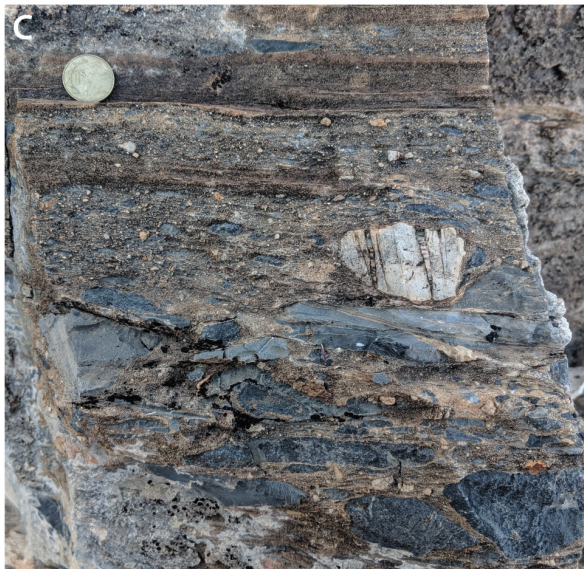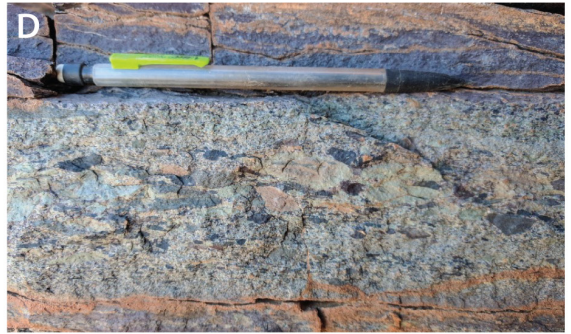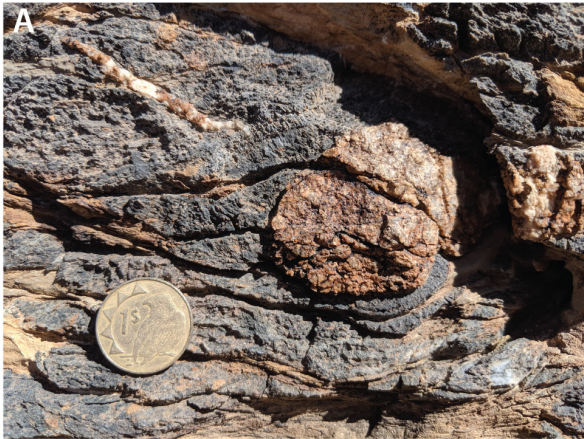
Figure 5. Field photographs depicting key stratigraphic features. For scale, the coin is 2.3 cm in diameter, the pencil is 15 cm in length, and the hammer is 33 cm long. **A)** The lowermost appearance of a granite lonestone is in the limestone debris flows of the Remhoogte Formation. **B)** Carbonate debris flows frequently occur throughout the Blässkranz Formation and sometimes contain ooid grains in the matrix. **C)** Stratified diamictite of the Blässkranz Formation consisting of repeated sediment gravity flows. **D)** The Tsugaub Volcaniclastic Member of the Blässkranz Formation typically has a light green matrix supporting various clasts. This example shows an example of reverse to normal grading. **E)** A granite boulder lonestone sits at the contact between the cap carbonate of the Tsabisis Formation and the purple wackestones and red sandstones of the uppermost Blässkranz Formation. **F)** In places, the uppermost portion of the Blässkranz Formation is missing due to an erosional unconformity and the Ediacaran Noab Formation lies directly above. Carbonate debris flows of the Noab Formation can include m-scale blocks of the Tsabisis cap carbonate (see also Morris and Grotzinger, 2023).

F828-210.5
$^{206}Pb/^{238}U$ weighted mean date =
635.84 ± 0.22/0.29/0.71Ma
n = 11, MSWD = 1.62

JP1715-187.9
$^{206}Pb/^{238}U$ weighted
mean date =
**635.93 ±
0.56/0.59/0.88 Ma**
n = 3, MSWD = 2.04

JP1713-193.7
$^{206}Pb/^{238}U$ single-grain date =
635.76 ± 0.79/0.81/1.04 Ma

F828-210.5, n = 71
JP1712-125.0, n = 51
JP1715-187.9, n = 33
JP1713-193.7, n = 39
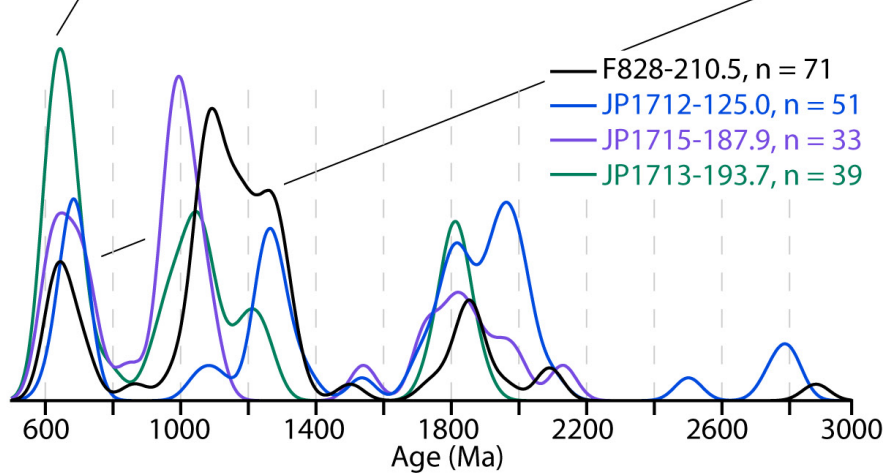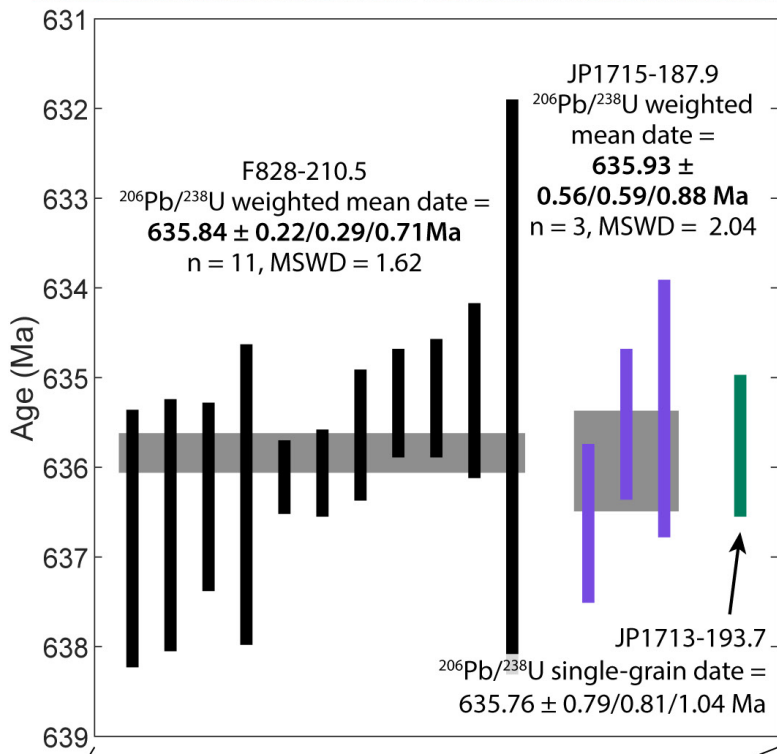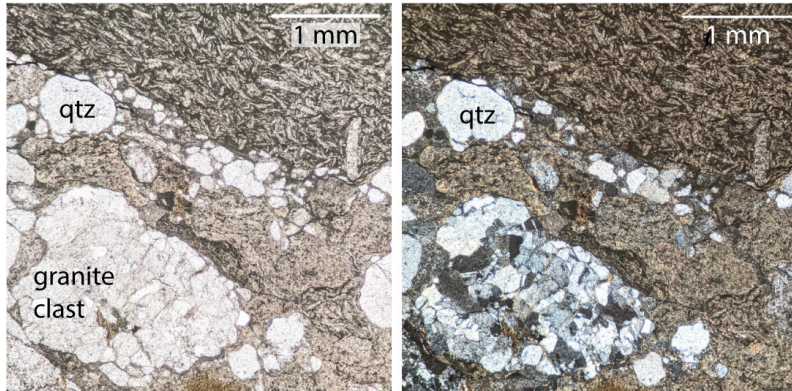
Figure 6. Ranked age plot for samples F828-210.5, JP1715-187.9, and JP1713-193.7 showing CA-ID-TIMS analyses on zircon, above the Q-ICPMS $^{206}Pb/^{238}U$ dates for the samples shown as a kernel density plot using KDredX2 (Spencer et al., 2017). All data is presented in tables S2 and S3. Only Q-ICPMS analyses that were >635 Ma or overlapped within uncertainty were included in the KDEs. The wide age distribution in the volcaniclastic flows reflects the incorporation of sedimentary material from many different sources. The flows were high energy, poorly sorted, and sometimes demonstrated reverse and normal grading (Fig. 5D). The photomicrograph of sample JP1713-193.7 shows mineral grains and rock clasts entrained in a volcanic matrix with a trachytic texture delineated by plagioclase phenocrysts.
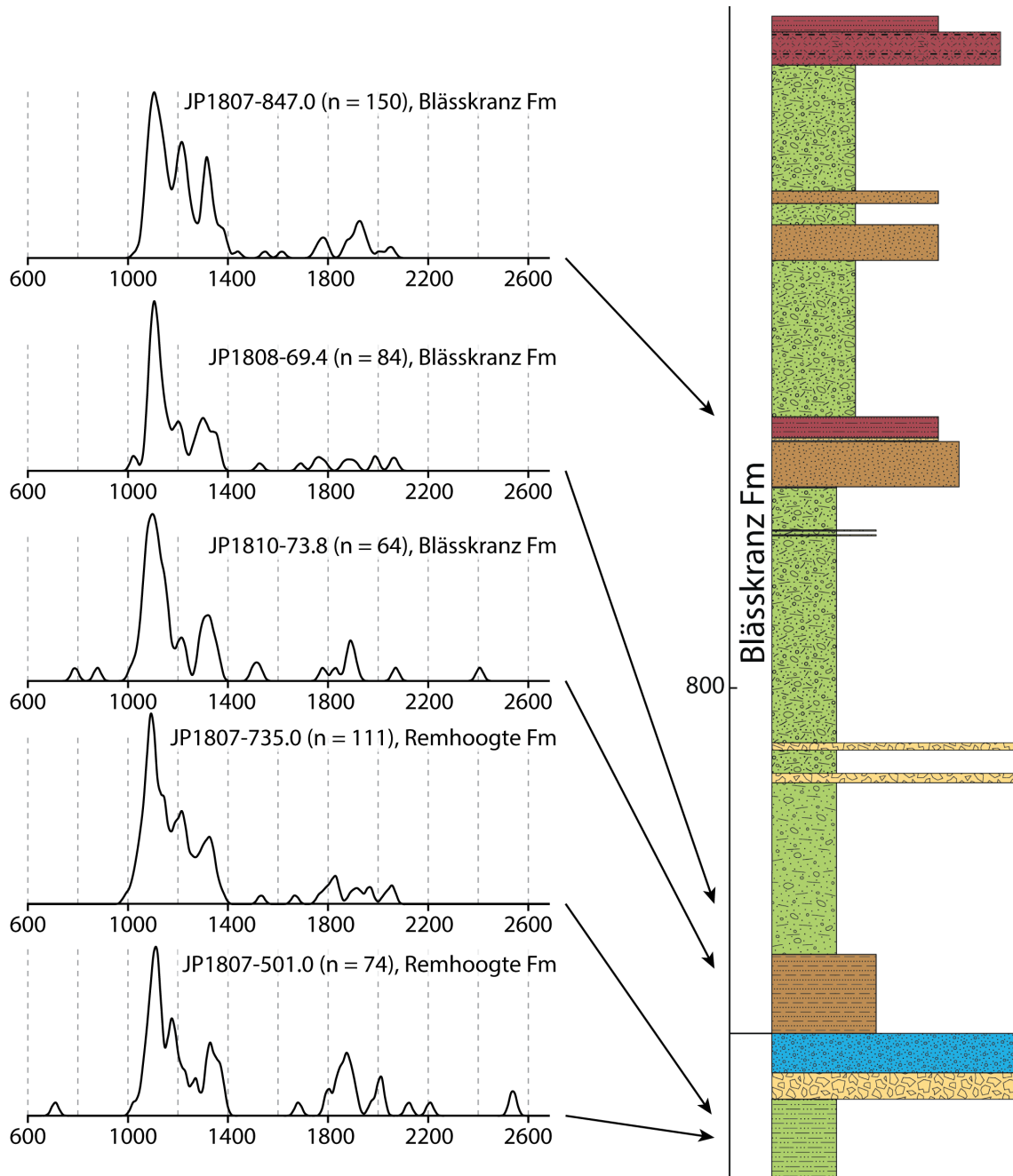
Figure 7. Detrital zircon spectra for Naukluft siliciclastic samples near the base of the Blässkranz Formation and at the top of the Remhoogte Formation. All samples show similar peaks at ~1.35, 1.2, and 1.1 Ga.

118
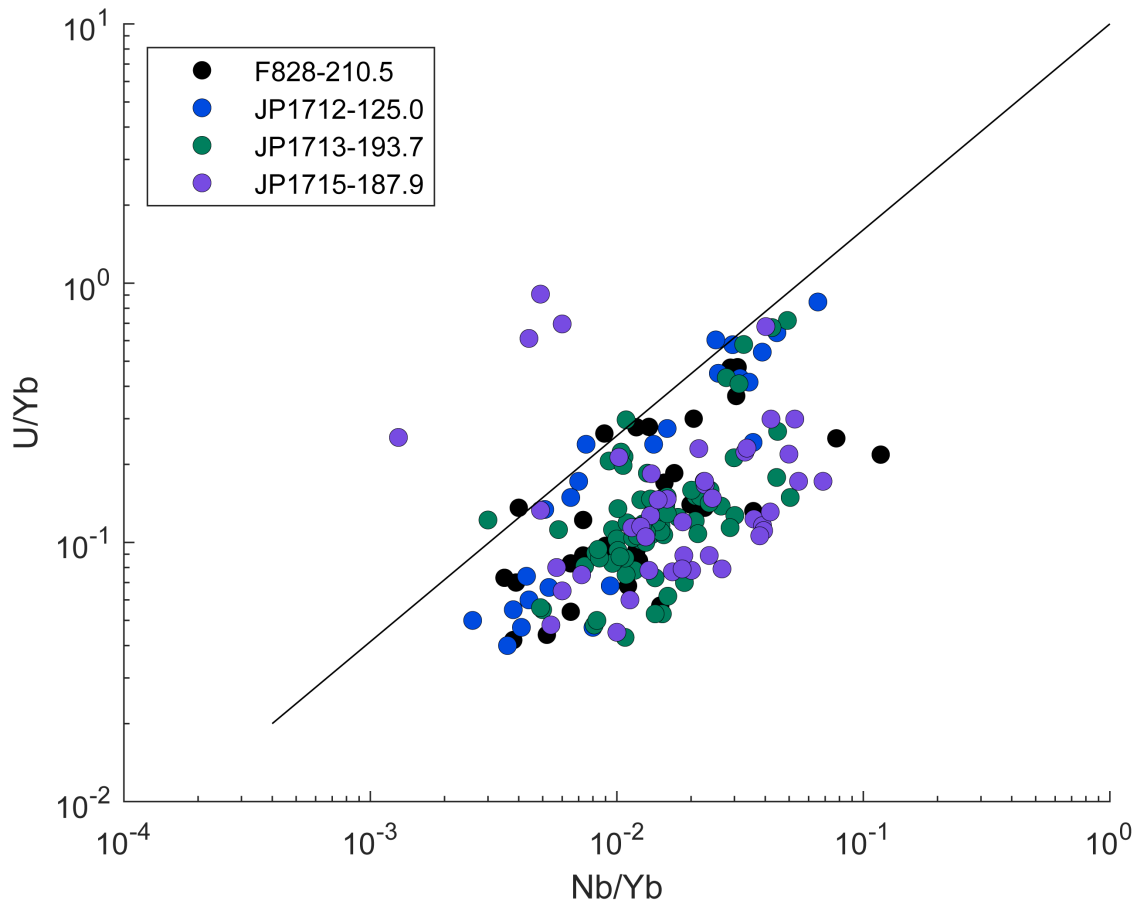
Figure 8. U/Yb vs. Nb/Yb for Naukluft volcaniclastic samples plot mostly below the "mantle-zircon array" range determined by Grimes et al. (2015). Magmatic arc zircon typically plot above the line plotted as the upper bound of the mantle-zircon range. All samples show some populations close to this boundary line with a few from sample JP1715-187.9 that plot well within the magmatic arc range.
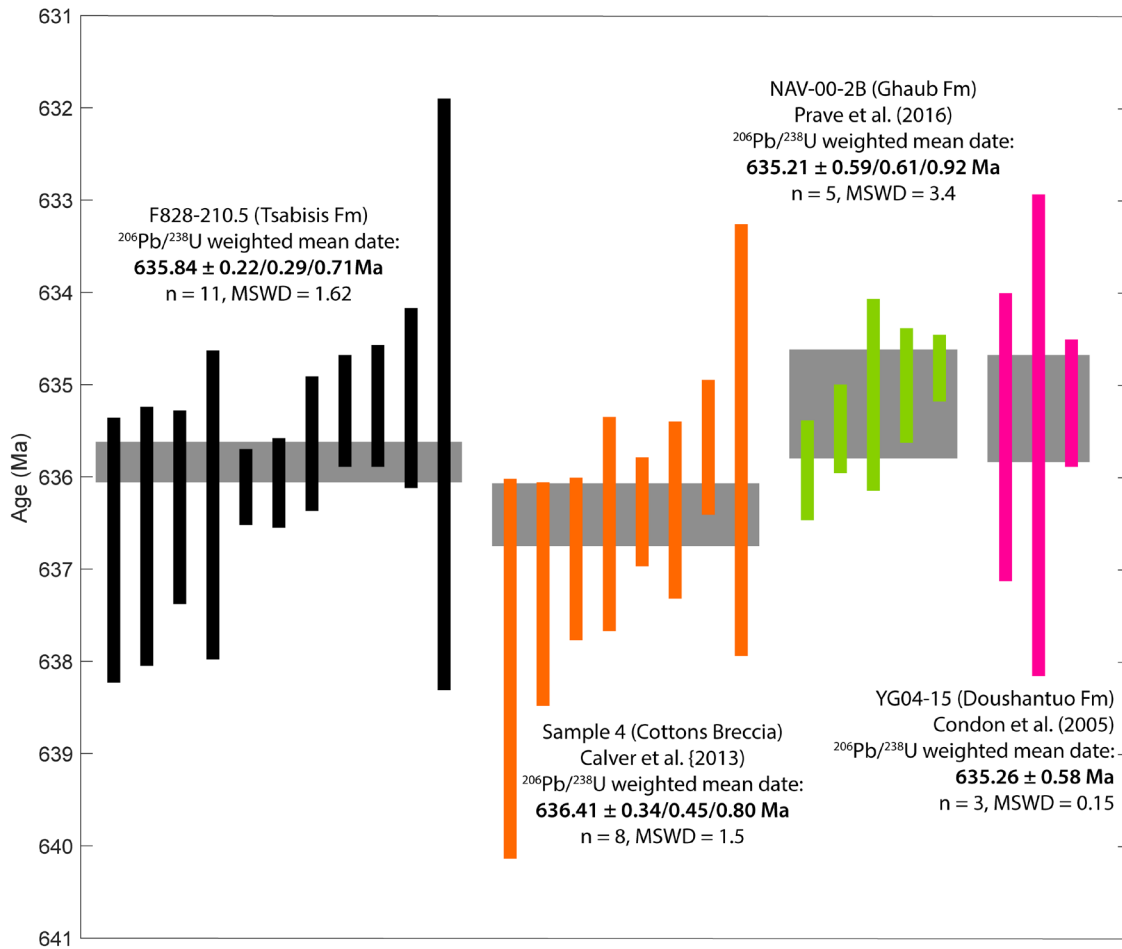
Figure 9. Ranked age plots comparing the weighted mean $^{206}Pb/^{238}U$ date of sample F828-210.5 from this study to other high-precision dates just below and above the Marinoan cap carbonate in other localities. Sample F828-210.5 is 38.5 m below the cap while Sample 4 from the Cottons Breccia in Tasmania, Australia is from a mudstone within 0.7 m of the cap (Calver et al., 2013). Sample NAV-00-2B from the Swakop terrane in central Namibia is from an ash bed ~30 m below the base of the cap (Prave et al., 2016), and YG04-15 is an ash from the Doushantuo Formation in South China 2.3 m above the base of the cap (Condon et al., 2005).

All samples used EARTHTIME tracer for U-Pb calibration and can be compared using "X"

uncertainties.

Appendix I

Supplementary materials for Chapter 1, "Emplacement of the Franklin large igneous province and initiation of the Sturtian Snowball Earth," can be accessed online at https://www.science.org/doi/full/10.1126/sciadv.adc9430#supplementary-materials.

Appendix II

Supplementary Material for Chapter 2:

Tonian basins record rifting of Kalahari from Rodinia and no evidence of a pre-Sturtian Kaigas glaciation

1. Detailed analytical methods

Sample locations and brief descriptions are listed in Table S1. Zircon mineral separation was carried out at Harvard University and the University of California, Santa Barbara (UCSB). Zircon grains were separated using standard crushing, magnetic susceptibility, and high-density liquid techniques. A variety of grains were picked by hand to capture the range of morphologies in the sample, but preference was given to multi-faceted prismatic forms. Selected grains were then annealed at 900ºC for 60 hours in a muffle furnace before being mounted in 1-inch diameter EpoFix resin rounds and polished to mid-section with a 0.3 μm finish. Cathodoluminescence (CL) imaging was obtained using an FEI Quanta 400F field emission gun scanning electron microscope (FEG-SEM) with a Centaurus detector at UCSB.

1.1. LASS geochronology

Laser ablation split stream (LASS) analyses used either the Nu Instruments Plasma 3D MC-ICPMS or the Nu Plasma High Resolution-Enhanced Sensitivity MC-ICPMS at UCSB, following the procedures described in Kylander-Clark et al. (2013) and Kylander-Clark (2017). Trace elements were measured on an Agilent 7700X quadrupole ICPMS. A Cetac/Photon Machines 193 nm Analyte excimer laser was used to ablate samples in a double-

chambered HelEx cell. Every 10 sample spots were bracketed with the primary zircon standard 91500 (Wiedenbeck et al., 1995), and every other block was bracketed with the secondary zircon standard GJ1 (Jackson et al., 2004), and tertiary standards in a rotating list. All experiments included Plešovice (Sláma et al., 2008) as a tertiary standard and others included a selection of MudTank (Black and Gulson, 1978; Gain et al., 2019), Peixe (Dickinson and Gehrels, 2003), FC-1 (Paces and Miller, 1993), 94-35 (Klepeis et al., 1998; Chang et al., 2006), or R33 (Black et al., 2004). For some experiments, a NIST612 spot was added to every block prior to the 91500 spot to regulate the laser arm movement. A spot size of 25 μm was used for every analysis except subsets of samples JP1704-74.9, JP1801-756.8, and JP1806-6.1 where a spot size of 20 μm was used due to small grain sizes.

Data were reduced using iolite4 software (Paton et al., 2010, 2011) and IsoplotR (Vermeesch, 2018). Standard error was propagated using methods described in Paton et al. (2010). The long-term excess variance is captured by 2% 2σ on ^{206}Pb/^{238}U ratios and 1.5% (2σ) for ^{207}Pb/^{206}Pb ratios for the setups used (Kylander-Clark et al., 2013; Horstwood et al., 2016). These percentages represent systematic uncertainties that are the limiting uncertainties for the data produced and cannot be reduced by increasing the number of analyses (Horstwood et al., 2016); therefore, any uncertainties less than these percentages for the respective ratios were increased to match and are denoted as "2s" to distinguish the added dispersion. ^{207}Pb/^{235}U ratios were calculated and uncertainties were propagated from ^{207}Pb/^{206}Pb and ^{206}Pb/^{238}U ratios and uncertainties using the ^{238}U/^{235}U value of 137.818 ± 0.045 (2σ; Hiess et al., 2012). Correlation coefficients were subsequently recalculated using the updated uncertainties (Schmitz and Schoene, 2007). Dates and their uncertainties were also recalculated in IsoplotR

(Vermeesch, 2018). Uncertainties for weighted mean dates are reported with 2% (2s) systematic error as well in order to compare data between analytical sessions and different U-Pb techniques (see Horstwood et al., 2016). Complete analytical data are presented in Table S2.

1.2. CA-ID-TIMS geochronology

Zircons were dislodged from their mounts and chemically abraded (Mattinson, 2005) by partial dissolution in 29 M HF at 210°C for 10 hours in Parr acid digestion vessels in order to mitigate the effects of radiation-induced Pb loss (Mattinson, 2005). Chemically abraded zircon grains were then fluxed successively in 3.5 M HNO_3 and 6 M HCl on a hot plate and in an ultrasonic bath and thoroughly rinsed after each step with MQ water to remove the leachates, before being loaded individually into PFA microcapsules. Each microcapsule was spiked with the EARTHTIME ET535 mixed ^{205}Pb-^{233}U-^{235}U tracer (Condon et al., 2015; McLean et al., 2015) before complete dissolution in 29 M HF in Parr acid digestion vessels held at 210°C for 48 hours. Following an HCl-based anion exchange column chemistry procedure (Krogh, 1973), the purified U and Pb were loaded together onto an outgassed Re filament in a silica gel/phosphoric acid mixture for isotopic measurements. Ratios of U and Pb isotopes were measured on an IsotopX X62 multi-collector thermal ionization mass spectrometer equipped with a Daly photomultiplier ion counting system at MIT. Pb isotopes were measured as mono-atomic ions in peak hopping mode on the ion counter and were corrected for mass-dependent isotope fractionation by applying an independently determined fractionation correction of 0.18% ± 0.05% per atomic mass unit (2σ). U isotopes were

measured as dioxide ions in a static mode using three Faraday collectors, while subjected to a within-run mass fractionation correction using the $^{233}U/^{235}U$ ratio of the spike and a sample $^{238}U/^{235}U$ ratio of 137.818 ± 0.045 (Hiess et al., 2012), as well as an oxide correction based on an $^{18}O/^{16}O$ ratio of 0.00205 ± 0.00005.

Data reduction, calculation of dates and propagation of uncertainties used the Tripoli and ET_Redux applications and algorithms (McLean et al., 2011; Bowring et al., 2011). The measured $^{206}Pb/^{238}U$ dates were corrected for initial ^{230}Th disequilibrium based on a magma Th/U ratio of 2.8 ± 1.0 (2σ). Complete analytical data are presented in Table S3.

2.1. Northern Kalahari paleogeography

The core of the Kalahari Craton is composed of the Zimbabwe, Kaapvaal, and Grunehogna cratons, which collided and amalgamated by ca. 1750 Ma (Jacobs et al., 2008). In the Mesoproterozoic, the northwestern margin (present-day coordinates) consisted of the volcano-sedimentary Sinclair Supergroup, which includes the Rehoboth and Konkiep subprovinces (Miller, 2012).

The Sinclair Supergroup is further divided into the Nauzerus and Tsumis groups, with U-Pb zircon dates of 1225 ± 10 Ma (Schneider et al., 2004) and 1226 ± 11 Ma (Becker et al., 2006). Both are intruded by the Gamsberg Granitic Suite and other 1210 ± 8 Ma porphyry dykes (Ziegler and Stoessel, 1993). The Rehoboth Subprovince has Paleoproterozoic basement (Cornell et al., 2011) and volcano-sedimentary cover dated to ~1.85-1.72 Ga (Becker et al., 2006; Becker and Schalk, 2008). It also includes the ~1.1 and 1.09 Ga rocks of the Langberg Formation (Becker et al., 2005), which is thought to be part of the Umkondo

Igneous Province (Hanson et al., 2004, 2006). The Konkiep Subprovince has poorly mapped and undated pre-Sinclair basement and volcano-sedimentary sequences that have been dated to ~1.47 Ga, ~1.38 Ga, ~1.33 Ga, and ~1.29 Ga (Hoal, 1990; Hoal and Heaman, 1995; Evans et al., 2007; Becker, 2008). The Konkiep Subprovince is separated from the Kakamas Terrane (also Gordonia Subprovince) to the south by the Excelsior-Lord Hill Shear Zone (Miller, 2012).

On the southern margins of the Kalahari Craton, the Namaqua-Natal belt covers >1000 km and extends under the Phanerozoic Karoo Supergroup of South Africa. The Namaqualand sector includes the Kakamas, Areachap, and Kaaien terranes that have Paleoproterozoic basement sequences and overlying volcanics and sediments that are ~1.4-1.1 Ga and ~1.09-1.08 Ga in age; the ca. 2.0-1.7 Ga Richtersveld Subprovince (Frimmel et al., 2001); and the Bushmanland and Garies terranes (ca. 1.8-1.6, 1.2-1.13, 1.06-1.01 Ga; Cornell et al., 2009). Namaquan tectonism occurred in two distinct episodes, the O'okiepian (~1.21-1.18 Ga) and Klondikean (~1.04-1.02 Ga) (Clifford et al., 2004; Clifford and Barton, 2012) events, and more recent studies of detrital zircon have expanded the maximum range of O'okiepian magmatism and sedimentation to ~1.5 Ga (Miller, 2012).

The Natal sector consists of three distinct tectonic terranes that formed in a subduction zone dipping away from the craton between ca. 1250–1100 Ma and were thrust over the Kaapvaal Craton at ~1135 Ma (Jacobs et al., 2008). By 1000 Ma, the Kalahari Craton had assembled, though some uncertainty remains concerning the tectonic history of the northern and eastern margins of the craton. During the Neoproterozoic, $\varepsilon_{Hf}(t)$ values for detrital zircon ranging from -24 to +14.8 with model T_{DM} ages between 3.1 and 1.05 Ga imply recycling of

mostly Paleoproterozoic crust and minor contribution from Archean crust (Hofmann et al., 2014). Bulk geochemical analyses of the sedimentary rocks also reflect sources derived from old continental crust and an inherited continental arc signature, with no evidence for an exotic cratonic source (Hofmann et al., 2014).

2.2 Congo-Kalahari reconstruction

Paleogeographic models commonly depict the Adamastor and Khomas oceans forming during the break-up of Rodinia separating the Congo and Kalahari craton from South American cratonic blocks, and then reuniting in the Pan-African orogenies in a similar geometry (Gray et al., 2008; Li et al., 2008; Konopásek et al., 2020; Hoffman, 2021; Caxito and Alkmim, 2023). These fixist models were recently reinforced by a ca. 1.11 Ga paleomagnetic pole from Congo that is consistent with a long-lived connection between SW Congo and the northern margin of the Kalahari (Salminen et al., 2018). However, this restoration is non-unique. Congo could be flipped 180° and still satisfy the paleomagnetic poles and the dike orientations of both the Umkondo LIP and the Huila-Epembe dikes (Ernst et al., 2013; Swanson-Hysell et al., 2015).

An additional argument for the inversion of a narrow V-shaped Khomas ocean is the similarity in stratigraphy across both margins and into the basinal allochthonous terranes of the Ugab and Swakop zones (Hoffmann and Prave, 1996). However, many margins globally display Tonian to Cryogenian rifted passive margins, which was one of the original arguments for the breakup of Rodinia (Hoffman, 1991), so this argument is also non-unique. On the southern margin of the Congo craton, rift-related volcanic rocks have been dated at 757 ±5

Ma, 759.95 ±0.86 Ma, 746 ±2, and 747 ±2 Ma (Hoffman et al., 1996; Halverson et al., 2005; Nascimento et al., 2017), broadly coeval with the Rosh Pinah volcanics dated here, but the flipped orientation of Congo would place these volcanics closer to the Rosh Pinah volcanics on the southwest margin of Kalahari (Ernst et al., 2013; Swanson-Hysell et al., 2015).

Multiple geological, paleomagnetic, and isotopic constraints suggest the southwest margin of the Kalahari collided with Laurentia between 1.11 and 1.00 Ga, with the Namaqua-Natal belt as the conjugate to the southern end of the Grenville orogen (Jacobs et al., 1993; Swanson-Hysell et al., 2015). In the fixist models, this would require a Stenian collision of the western margin of Congo with Laurentia and/or Amazonia. However, there are no known Stenian metamorphic rocks on the western margin of the Congo craton. Instead, Stenian igneous and metamorphic rocks are restricted to the eastern margin of the Congo in the Irumide belt (De Waele et al., 2006), again favoring a flipped Congo orientation.

The tie proposed here between the 752 Ma Rosh Pinah volcanics and graben on the SW Kalahari margin, and the 752 Ma Mount Rogers complex of Virginia on the SE Laurentia margin provides another argument for the flipped position of the Congo. If Kalahari's position against Laurentia persisted until ca. 752 Ma, paleomagnetic data from Laurentia provide a Late Tonian pole path that would fix Kalahari between 10-30° S (Eyster et al., 2020; Macdonald et al., 2023). In the fixist models, this would place Congo at mid-latitudes, below 30° S. However, paleomagnetic data from the Congo requires that it is at the equator ca. 765-748 Ma (Meert et al., 1995; Wingate et al., 2010). Instead, in the flipped model that we develop here, Congo can occupy equatorial latitudes and satisfy the Late Tonian Luakela and Mbozi poles (Meert et al., 1995; Wingate et al., 2010).

References

Becker, T., 2008, The Kairab Formation east of Sesriem and the associated, subvolcanic intrusive rocks, *in* Miller, R.M. ed., The Geology of Namibia, Windhoek, Geological Survey of Namibia, p. 8.10-8.16.

Becker, T., Garoeb, H., Ledru, P., and Milesi, J.P., 2005, The Mesoproterozoic event within the Rehoboth Basement Inlier of Namibia: Review and new aspects of stratigraphy, geochemistry structure and plate tectonic setting: South African Journal of Geology, v. 108, p. 465–492, doi:10.2113/108.4.465.

Becker, T., and Schalk, K.E.L., 2008, Rehoboth Group, *in* Miller, R.M. ed., The Geology of Namibia, Windhoek, Geological Survey of Namibia, p. 5.29-5.61.

Becker, T., Schreiber, U., Kampunzu, A.B., and Armstrong, R., 2006, Mesoproterozoic rocks of Namibia and their plate tectonic setting: Journal of African Earth Sciences, v. 46, p. 112–140, doi:10.1016/j.jafrearsci.2006.01.015.

Black, L.P. et al., 2004, Improved $^{206}Pb/^{238}U$ microprobe geochronology by the monitoring of a trace-element-related matrix effect; SHRIMP, ID-TIMS, ELA-ICP-MS and oxygen isotope documentation for a series of zircon standards: Chemical Geology, v. 205, p. 115–140, doi:10.1016/j.chemgeo.2004.01.003.

Black, L.P., and Gulson, B.L., 1978, The age of the Mud Tank carbonatite, Strangways Range, Northern Territory: BMR Journal of Australian Geology and Geophysics, v. 3, p. 227–232.

Bowring, J.F., McLean, N.M., and Bowring, S.A., 2011, Engineering cyber infrastructure for U-Pb geochronology: Tripoli and U-Pb_Redux: Geochemistry, Geophysics, Geosystems, v. 12, doi:10.1029/2010GC003479.

Caxito, F. de A., and Alkmim, F.F., 2023, The role of V-shaped oceans and ribbon continents in the Brasiliano/PanAfrican assembly of western Gondwana: Scientific Reports, v. 13, p. 1–16, doi:10.1038/s41598-023-28717-7.

Chang, Z., Vervoort, J.D., McClelland, W.C., and Knaack, C., 2006, U-Pb dating of zircon by LA-ICP-MS: Geochemistry, Geophysics, Geosystems, v. 7, doi:10.1029/2005GC001100.

Clifford, T.N., and Barton, E.S., 2012, The O'okiep Copper District, Namaqualand, South Africa: a review of the geology with emphasis on the petrogenesis of the cupriferous Koperberg Suite: Mineralium Deposita, v. 47, p. 837–857.

Clifford, T.N., Barton, E.S., Stern, R.A., and Duchesne, J.-C., 2004, U-Pb zircon calendar for Namaqua (Grenville) crustal events in the granulite-facies terrane of the O'okiep Copper District of South Africa: Journal of Petrology, v. 45, p. 669–691.

Condon, D.J., Schoene, B., McLean, N.M., Bowring, S.A., and Parrish, R.R., 2015, Metrology and traceability of U-Pb isotope dilution geochronology (EARTHTIME Tracer Calibration Part I): Geochimica et Cosmochimica Acta, v. 164, p. 464–480, doi:10.1016/j.gca.2015.05.026.

Cornell, D.H., Pettersson, A., Whitehouse, M.J., and Schersten, A., 2009, A New Chronostratigraphic Paradigm for the Age and Tectonic History of the Mesoproterozoic

Bushmanland Ore District, South Africa: Economic Geology, v. 104, p. 385–404, doi:10.2113/gsecongeo.104.3.385.

Cornell, D.H., van Schijndel, V., Ingolfsson, O., Scherstén, A., Karlsson, L., Wojtyla, J., and Karlsson, K., 2011, Evidence from Dwyka tillite cobbles of Archaean basement beneath the Kalahari sands of southern Africa: Lithos, v. 125, p. 482–502, doi:10.1016/j.lithos.2011.03.006.

Dickinson, W.R., and Gehrels, G.E., 2003, U-Pb ages of detrital zircons from Permian and Jurassic eolian sandstones of the Colorado Plateau, USA: Paleogeographic implications: Sedimentary Geology, v. 163, p. 29–66, doi:10.1016/S0037-0738(03)00158-1.

Ernst, R.E., Pereira, E., Hamilton, M.A., Pisarevsky, S.A., Rodriques, J., Tassinari, C.C.G., Teixeira, W., and Van-Dunem, V., 2013, Mesoproterozoic intraplate magmatic "barcode" record of the Angola portion of the Congo Craton: Newly dated magmatic events at 1505 and 1110Ma and implications for Nuna (Columbia) supercontinent reconstructions: Precambrian Research, v. 230, p. 103–118, doi:10.1016/j.precamres.2013.01.010.

Evans, D.M., Windrim, D.P., and Armstrong, R.A., 2007, Age of Metavolcanic rocks at the northern margin of the Namaqua-Natal Metamorphic Province in the Karas Mountains, Namibia, defined by SHRIMP U-Pb dating of zircons: South African Journal of Geology, v. 110, p. 47–54, doi:10.2113/gssajg.110.1.47.

Eyster, A., Weiss, B.P., Karlstrom, K., and Macdonald, F.A., 2020, Paleomagnetism of the Chuar Group and evaluation of the late Tonian Laurentian apparent polar wander path with implications for the makeup and breakup of Rodinia: GSA Bulletin, v. 132, p. 710–738, doi:10.1130/B32012.1.

Frimmel, H.E., Zartman, R.E., and Späth, A., 2001, The Richtersveld igneous complex, South Africa: U-Pb zircon and geochemical evidence for the beginning of Neoproterozoic continental breakup: Journal of Geology, v. 109, p. 493–508, doi:10.1086/320795.

Gain, S.E.M., Gréau, Y., Henry, H., Belousova, E., Dainis, I., Griffin, W.L., and O'Reilly, S.Y., 2019, Mud Tank Zircon: Long-Term Evaluation of a Reference Material for U-Pb Dating, Hf-Isotope Analysis and Trace Element Analysis: Geostandards and Geoanalytical Research, v. 43, p. 339–354, doi:10.1111/ggr.12265.

Gray, D.R., Foster, D.A., Meert, J.G., Goscombe, B.D., Armstrong, R., Trouw, R.A.J., and Passchier, C.W., 2008, A Damara orogen perspective on the assembly of southwestern Gondwana: Geological Society Special Publication, v. 294, p. 257–278, doi:10.1144/SP294.14.

Halverson, G.P., Hoffman, P.F., Schrag, D.P., Maloof, A.C., and Rice, A.H.N., 2005, Toward a Neoproterozoic composite carbon-isotope record: GSA Bulletin, v. 117, p. 1181–1207, doi:10.1130/B25630.1.

Hanson, R.E. et al., 2006, Mesoproterozoic intraplate magmatism in the Kalahari Craton: A review: Journal of African Earth Sciences, v. 46, p. 141–167, doi:10.1016/j.jafrearsci.2006.01.016.

Hanson, R.E., Crowley, J.L., Bowring, S.A., Ramezani, J., Gose, W.A., Dalziel, I.W.D., Pancake, J.A., Seidel, E.K., Blenkinsop, T.G., and Mukwakwami, J., 2004, Coeval Large-Scale Magmatism in the Kalahari and Laurentian Cratons During Rodinia Assembly: Science, v. 304, p. 1126–1129, doi:10.1126/science.1096329.

Hiess, J., Condon, D.J., McLean, N., and Noble, S.R., 2012, $^{238}U/^{235}U$ systematics in terrestrial uranium-bearing minerals: Science, v. 335, p. 1610–1614, doi:10.1126/science.1215507.

Hoal, B.G., 1990, The geology and geochemistry of the Proterozoic Awasib Mountain terrain, southern Namibia: Memoir of the Geological Society of Namibia, v. 11, p. 163 pp.

Hoal, B.G., and Heaman, L.M., 1995, The Sinclair sequence: U-Pb age constraints from the Awasib Mountain area: Communications of the Geological Survey of Namibia, v. 10, p. 83–91.

Hoffman, P.F., 1991, Did the breakout of Laurentia turn Gondwanaland inside-out? Science, v. 252, p. 1409–1412, doi:10.1126/science.252.5011.1409.

Hoffman, P.F., 2021, On the kinematics and timing of Rodinia breakup: a possible rift–transform junction of Cryogenian age at the southwest cape of Congo Craton (northwest Namibia): South African Journal of Geology, v. 124, doi:10.25131/sajg.124.0038.

Hoffman, P.F., Hawkins, D.P., Isachsen, C.E., and Bowring, S.A., 1996, Precise U-Pb zircon ages for early Damaran magmatism in the Summas Mountains and Welwitschia Inlier, northern Damara Belt, Namibia: Communs geol. Surv. Namibia, v. 11, p. 49–53.

Hoffmann, K.-H., and Prave, A.R., 1996, A preliminary note on revised subdivision and regional correlation of the Otavi Group based on glaciogenic diamctites and associated cap dolostones: Communications of the Geological Survey of Namibia, v. 11, p. 83–88.

Hofmann, M., Linnemann, U., Hoffmann, K.H., Gerdes, A., Eckelmann, K., and Gärtner, A., 2014, The Namuskluft and Dreigratberg sections in southern Namibia (Kalahari Craton, Gariep Belt): A geological history of Neoproterozoic rifting and recycling of cratonic crust during the dispersal of Rodinia until the amalgamation of Gondwana: International Journal of Earth Sciences, v. 103, p. 1187–1202, doi:10.1007/s00531-013-0949-6.

Horstwood, M.S.A. et al., 2016, Community-Derived Standards for LA-ICP-MS U-(Th-)Pb Geochronology – Uncertainty Propagation, Age Interpretation and Data Reporting: Geostandards and Geoanalytical Research, v. 40, p. 311–332, doi:10.1111/j.1751-908X.2016.00379.x.

Jackson, S.E., Pearson, N.J., Griffin, W.L., and Belousova, E.A., 2004, The application of laser ablation-inductively coupled plasma-mass spectrometry to in situ U-Pb zircon geochronology: Chemical Geology, v. 211, p. 47–69, doi:10.1016/j.chemgeo.2004.06.017.

Jacobs, J., Pisarevsky, S., Thomas, R.J., and Becker, T., 2008, The Kalahari Craton during the assembly and dispersal of Rodinia: Precambrian Research, v. 160, p. 142–158, doi:10.1016/j.precamres.2007.04.022.

Jacobs, J., Thomas, R.J., and Weber, K., 1993, Accretion and indentation tectonics at the southern edge of the Kaapvaal Craton during the Kibaran (Grenville) orogeny: Geology, v. 21, p. 203–206, doi:10.1130/0091-7613(1993)021<0203:AAITAT>2.3.CO;2.

Klepeis, K.A., Crawford, M.L., and Gehrels, G., 1998, Structural history of the crustal-scale Coast shear zone north of Portland Canal, southeast Alaska and British Columbia: Journal of Structural Geology, v. 20, p. 883–904, doi:10.1016/S0191-8141(98)00020-0.

Konopásek, J., Cavalcante, C., Fossen, H., and Janoušek, V., 2020, Adamastor – an ocean that never existed? Earth-Science Reviews, v. 205, p. 103201, doi:10.1016/j.earscirev.2020.103201.

Krogh, T.E., 1973, A low-contamination method for hydrothermal decomposition of zircon

and extraction of U and Pb for isotopic age determinations: Geochimica et Cosmochimica Acta, v. 37, p. 485–494.

Kylander-Clark, A.R.C., 2017, Petrochronology by Laser-Ablation Inductively Coupled Plasma Mass Spectrometry: Reviews in Mineralogy and Geochemistry, v. 83, p. 183–198, doi:10.2138/rmg.2017.83.6.

Kylander-Clark, A.R.C., Hacker, B.R., and Cottle, J.M., 2013, Laser-ablation split-stream ICP petrochronology: Chemical Geology, v. 345, p. 99–112, doi:10.1016/j.chemgeo.2013.02.019.

Li, Z.X. et al., 2008, Assembly, configuration, and break-up history of Rodinia: A synthesis: Precambrian Research, v. 160, p. 179–210, doi:10.1016/j.precamres.2007.04.021.

Macdonald, F.A., Yonkee, W.A., Flowers, R.M., and Swanson-Hysell, N.L., 2023, Neoproterozoic of Laurentia: Memoir of the Geological Society of America, v. 220, p. 331–380, doi:10.1130/2022.1220(19).

Mattinson, J.M., 2005, Zircon U-Pb chemical abrasion (“CA-TIMS”) method: Combined annealing and multi-step partial dissolution analysis for improved precision and accuracy of zircon ages: Chemical Geology, v. 220, p. 47–66, doi:10.1016/j.chemgeo.2005.03.011.

McLean, N.M., Bowring, J.F., and Bowring, S.A., 2011, An algorithm for U-Pb isotope dilution data reduction and uncertainty propagation: Geochemistry, Geophysics, Geosystems, v. 12, doi:10.1029/2010GC003478.

McLean, N.M., Condon, D.J., Schoene, B., and Bowring, S.A., 2015, Evaluating uncertainties in the calibration of isotopic reference materials and multi-element isotopic tracers (EARTHTIME Tracer Calibration Part II): Geochimica et Cosmochimica Acta, v. 164, p. 481–501, doi:10.1016/j.gca.2015.02.040.

Meert, J.G., van der Voo, R., and Ayub, S., 1995, Paleomagnetic investigation of the Neoproterozoic Gagwe lavas and Mbozi complex, Tanzania and the assembly of Gondwana: Precambrian Research, v. 74, p. 225–244, doi:10.1016/0301-9268(95)00012-T.

Miller, R.M., 2012, Review of Mesoproterozoic Magmatism, Sedimentation and Terrane Amalgamation in Southwestern Africa: South African Journal of Geology, v. 115, p. 417–448, doi:10.2113/gssajg.115.4.417.

Nascimento, D.B., Schmitt, R.S., Ribeiro, A., Trouw, R.A.J., Passchier, C.W., and Basei, M.A.S., 2017, Depositional ages and provenance of the Neoproterozoic Damara Supergroup (northwest Namibia): Implications for the Angola-Congo and Kalahari cratons connection: Gondwana Research, v. 52, p. 153–171, doi:10.1016/j.gr.2017.09.006.

Paces, J.B., and Miller, J.D., 1993, Precise U-Pb ages of Duluth Complex and related mafic intrusions, northeastern Minnesota: Geochronological insights to physical, petrogenetic, paleomagnetic, and tectonomagmatic processes associated with the 1.1 Ga Midcontinent Rift System: Journal of Geophysical Research: Solid Earth, v. 98, p. 13997–14013, doi:10.1029/93JB01159.

Paton, C., Hellstrom, J., Paul, B., Woodhead, J., and Hergt, J., 2011, Iolite: Freeware for the visualisation and processing of mass spectrometric data: Journal of Analytical Atomic Spectrometry, v. 26, p. 2508, doi:10.1039/c1ja10172b.

Paton, C., Woodhead, J.D., Hellstrom, J.C., Hergt, J.M., Greig, A., and Maas, R., 2010, Improved laser ablation U-Pb zircon geochronology through robust downhole fractionation correction: Geochemistry, Geophysics, Geosystems, v. 11, doi:10.1029/2009GC002618.

Salminen, J., Hanson, R., Evans, D.A.D., Gong, Z., Larson, T., Walker, O., Gumsley, A., Söderlund, U., and Ernst, R., 2018, Direct Mesoproterozoic connection of the Congo and Kalahari cratons in proto-Africa: Strange attractors across supercontinental cycles: Geology, v. 46, p. 1011–1014, doi:10.1130/G45294.1.

Schmitz, M.D., and Schoene, B., 2007, Derivation of isotope ratios, errors, and error correlations for U-Pb geochronology using ^{205}Pb-^{235}U-(^{233}U)-spiked isotope dilution thermal ionization mass spectrometric data: Geochemistry, Geophysics, Geosystems, v. 8, p. 1–20, doi:10.1029/2006GC001492.

Schneider, T., Becker, T., Borg, G., Hilken, U., Hansen, B.T., and Weber, K., 2004, New U-Pb zircon ages of the Nückopf Formation and their significance for the Mesoproterozoic event in Namibia: Communs geol. Surv. Namibia, v. 13, p. 63–74.

Sláma, J. et al., 2008, Plešovice zircon — A new natural reference material for U – Pb and Hf isotopic microanalysis: v. 249, p. 1–35, doi:10.1016/j.chemgeo.2007.11.005.

Swanson-Hysell, N.L., Kilian, T.M., and Hanson, R.E., 2015, A new grand mean palaeomagnetic pole for the 1.11 ga Umkondo large igneous province with implications for palaeogeography and the geomagnetic field: Geophysical Journal International, v. 203, p. 2237–2247, doi:10.1093/gji/ggv402.

Vermeesch, P., 2018, IsoplotR: A free and open toolbox for geochronology: Geoscience Frontiers, v. 9, p. 1479–1493, doi:10.1016/j.gsf.2018.04.001.

De Waele, B., Kampunzu, A.B., Mapani, B.S.E., and Tembo, F., 2006, The Mesoproterozoic Irumide belt of Zambia: Journal of African Earth Sciences, v. 46, p. 36–70, doi:10.1016/j.jafrearsci.2006.01.018.

Wiedenbeck, M., Allé, P., Corfu, F., Griffin, W. l., Meier, M., Oberli, F., Von Quadt, A., Roddick, J.C., and Spiegel, W., 1995, Three Natural Zircon Standards for U-Th-Pb, Lu-Hf, Trace Element and REE Analyses: Geostandards and Geoanalytical Research, v. 19, p. 1–23, doi:10.1111/j.1751-908X.1995.tb00147.x.

Wingate, M.T.D., Pisarevsky, S.A., and De Waele, B., 2010, Paleomagnetism of the 765 Ma Luakela volcanics in Northwest Zambia and implications for Neoproterozoic positions of the Congo Craton: American Journal of Science, v. 310, p. 1333–1344, doi:10.2475/10.2010.05.

Ziegler, U.R.F., and Stoessel, G.F.U., 1993, Age determinations in the Rehoboth Basement Inlier, Namibia: Memoir of the Geological Society of Namibia, v. 14, p. 106 pp.

Sample name	Lat (°)	Long (°)	Formation	Description
ES1770	-27.7769	16.6681	Rosh Pinah	Tuffaceous sandstone
ES1772-8	-27.7823	16.6578	Rosh Pinah	Porphyritic rhyolite
ES1772-52	-27.7826	16.6575	Rosh Pinah	Porphyritic rhyolite
ES1772-158.5	-27.7836	16.6568	Rosh Pinah	Fine tuffaceous sandstone
JP1704-74.9	-27.7901	16.6584	Rosh Pinah	Siltstone
JP1710	-27.8336	16.7025	Spitzkop Suite	Rhyolite with scoria clasts
JP1801C-26.9	-27.7364	16.6200	Rosh Pinah	Green and white banded fine sandstone
F1814-366.0	-27.7111	16.5732	Rosh Pinah	Green and white banded fine sandstone
JP1801-51.3	-27.7424	16.6218	Rosh Pinah	Green-blue schist
JP1801-642.3	-27.7514	16.6239	Rosh Pinah	Coarse arkosic sandstone
JP1801-756.8	-27.7520	16.6231	Rosh Pinah	Fine sandstone
JP1805-0.8	-28.0177	16.8535	Lower Holgat (Namaskluft member)	Diamictite with siltstone matrix
JP1806-6.1	-28.1019	16.8733	Lower Holgat (nonglacial interlude)	Fine sandstone

Table S1. Sample coordinates and lithologies

Table S2. U-Pb LASS data (separate Excel file)

Table S3. U-Pb isotopic data from CA-ID-TIMS zircon analyses.

						Ratios							Ages (Ma)							LA-ICPMS	
Sample Fractions	Pb(c) (pg)	Pb* Pb(c)	U (pg)	Th U	206Pb 204Pb	208Pb 206Pb	206Pb 238U	err (2σ%)	207Pb 235U	err (2σ%)	207Pb 206Pb	err (2σ%)	206Pb 238U	err (2σ)	207Pb 235U	err (2σ)	207Pb 206Pb	err (2σ)	corr. coef.	206Pb 238U	err (2σ)
(a)	(b)	(b)	(c)		(d)	(e)	(f)		(f)		(f)										
ES1772-52																					
zm69	0.20	45.0	62	0.96	2396.7	0.294	0.123918	(.11)	1.10136	(.46)	0.06449	(.43)	753.08	0.76	754.0	2.5	756.8	9.2	0.37	744	14
zm67	0.18	69.6	85	0.94	3708.5	0.290	0.123912	(.11)	1.10115	(.35)	0.06448	(.32)	753.04	0.80	753.9	1.8	756.5	6.8	0.38	749	14
zm17	0.21	15.0	22	0.90	819.9	0.277	0.123874	(.24)	1.09442	(1.54)	0.06411	(1.47)	752.8	1.7	750.6	8.2	744	31	0.37	737	14
zm74	0.22	53.9	79	0.99	2842.5	0.306	0.123819	(.10)	1.10337	(.38)	0.06466	(.35)	**752.50**	**0.70**	755.0	2.0	762.3	7.5	0.37	747	14
zm72	0.44	44.2	123	1.32	2176.1	0.405	0.123779	(.14)	1.10016	(.60)	0.06449	(.54)	**752.3**	**1.0**	753.4	3.2	757	11	0.50	746	14
zm73	0.23	57.9	90	1.03	3022.2	0.318	0.123676	(.09)	1.10115	(.36)	0.06460	(.34)	**751.69**	**0.64**	753.9	1.9	760.5	7.3	0.28	754	14
zm75	0.20	50.2	71	0.93	2691.7	0.285	0.123639	(.09)	1.09233	(.46)	0.06410	(.44)	**751.48**	**0.65**	749.6	2.4	744.1	9.3	0.28	738	14
zm48	0.24	39.0	64	1.05	2036.4	0.323	0.123635	(.10)	1.09785	(.54)	0.06443	(.51)	**751.45**	**0.74**	752.3	2.8	755	11	0.34	722	13
zm16	0.29	12.0	25	0.90	661.0	0.276	0.123088	(.22)	1.08728	(1.71)	0.06409	(1.65)	748.3	1.6	747.2	9.0	744	35	0.32	724	14
ES1772-8																					
zL13	0.50	49.6	175	0.87	2695.3	0.267	0.123913	(.15)	1.09962	(.56)	0.06439	(.52)	**753.0**	**1.1**	753.2	3.0	754	11	0.34	746	14
zL10	0.17	131.6	156	0.87	7116.5	0.267	0.123875	(.09)	1.09974	(.20)	0.06442	(.17)	**752.83**	**0.62**	753.2	1.0	754.4	3.6	0.52	742	14
zL15	0.24	209.2	355	0.88	11276	0.270	0.123807	(.09)	1.09813	(.20)	0.06436	(.16)	**752.44**	**0.66**	752.4	1.0	752.5	3.4	0.57	747	14
zL24	0.17	150.6	176	0.90	8079.9	0.277	0.123791	(.09)	1.09918	(.19)	0.06443	(.15)	**752.35**	**0.61**	753.0	1.0	754.7	3.2	0.66	739	14
zL6	0.25	126.2	219	0.90	6776.4	0.277	0.123760	(.08)	1.09985	(.19)	0.06448	(.16)	**752.17**	**0.56**	753.3	1.0	756.6	3.5	0.51	744	14
zL20	0.31	107.7	237	0.83	5887.5	0.254	0.123731	(.08)	1.09798	(.24)	0.06439	(.21)	**752.00**	**0.57**	752.4	1.3	753.5	4.4	0.50	744	14

Table S3. U-Pb CA-ID TIMS data. (a) Thermally annealed and pre-treated single zircon. Analyses used in weighted mean date calculation are in bold.(b) Total common-Pb (Pbc) in analysis. Pb* is radiogenic lead. (c) Total sample U content. (d) Measured ratio corrected for spike and fractionation only. (e) Radiogenic Pb ratio. (f) Corrected for fractionation, spike and blank. Also corrected for initial Th/U disequilibrium using radiogenic ^{208}Pb and Th/Umagma = 2.8. Mass fractionation correction of 0.18%/amu ± 0.04%/amu (atomic mass unit) was applied to single-collector Daly analyses. All common Pb assumed to be laboratory blank. Total procedural blank less than 0.1 pg for U. Blank isotopic composition: ^{206}Pb/^{204}Pb = 18.15 ± 0.47, ^{207}Pb/^{204}Pb =15.30 ± 0.30, ^{208}Pb/^{204}Pb = 37.11 ± 0.87. Corr. coef. = correlation coefficient. Ages calculated using the decay constants λ_{238} = 1.55125E-10 y^{-1} and λ_{235} = 9.8485E-10 y^{-1} (Jaffey et al., 1971).

Appendix III

Supplementary Material for Chapter 3:

Stratigraphy and geochronology of the Marinoan Snowball Earth deglaciation on the northwest margin of the Kalahari Craton

1. **CA-ID-TIMS analytical methods**

Mineral separation for the U-Pb analyses was done at Harvard University and UCSB. All samples were hand-sledged into chips that were ≤1 cm3 and then pulsed in 1–2 s intervals in a SPEX 8530 ShatterBox® while sieving for the <500 μm fraction. The <500 μm fraction for each sample was either washed in gold pans until a few g of material were left or handwashed in 5 L beakers to remove fine material and dried under heat lamps or in low-temperature ovens before being run on the Frantz magnetic separator. If the Frantz magnetic separator was used, highly magnetic minerals were first removed using a hand magnet and then samples were typically run twice on the Frantz, first at 0.3 A and 20° tilt and the second time at 0.6 A and 20° tilt. If the sample was mostly magnetic, the tilt angle was increased by 5–10° to ensure that no non-magnetic grains were carried by the flow of magnetic grains. Heavy liquid density separation using methylene iodide was the last step for isolating the dense mineral fraction of zircon following separation on the Frantz. Zircon grains were hand-picked for each sample from either this final fraction or directly following gold panning.

All CA-ID-TIMS analyses were done at Boise State University. U-Pb dates were obtained using the CA-ID-TIMS procedure developed by Mattinson (2005). Zircon grains were first annealed at 900°C for 60 hours. The grains were then chemically abraded using 29 M HF in Parr acid digestion vessels held at 180°C or 190°C for 12 hrs. There were no major

differences between analyses noted for the different chemical abrasion temperatures. The leachate was discarded, and the remaining samples were rinsed repeatedly in MQ H2O and 3.5 M HNO$_3$, sonicated for 30 min. and fluxed on the hot plate for 30 min. after the first round of rinsing. Samples were spiked using the EARTHTIME mixed U-Pb isotope tracer solution (ET535; Condon et al., 2015) and fully dissolved in Parr acid digestion vessels held at 220°C for 48 hrs. U and Pb were extracted from the samples through column chemistry with AG-1 X8, 200–400 mesh, Cl$^-$ anion exchange resin following methods modified from Krogh (1973). Measurements were made on an IsotopX IsoProbe-T thermal ionization mass spectrometer (TIMS). Pb isotopes were measured by peak hopping on the Daly detector and U isotopes were measured in static collection mode on Faraday cups.

U-Pb dates and uncertainties were calculated following Schmitz and Schoene (2007). The value 137.818 ± 0.045 (2σ) was used for the $^{238}U/^{235}U$ ratio in natural zircon (Hiess et al., 2012). Model Th/U ratios were calculated iteratively from measured $^{206}Pb/^{208}Pb$ ratios and calculated $^{206}Pb/^{238}U$ ages. Up to 1 pg of common Pb (Pbc) was assumed to be procedural blank and accounted for using the measured laboratory Pbc isotopic composition. Excess Pbc was attributed to initial common Pb using the two-stage Pb isotope evolution model (Stacey and Kramers, 1975) at the nominal sample age. Complete analytical data are presented in Table S2.

2. LASS analytical methods

Laser ablation split stream (LASS) analyses used either the Nu Instruments Plasma 3D MC-ICP-MS or the Nu Plasma High Resolution-Enhanced Sensitivity (HR-ES) MC-ICPMS

at the Preston Cloud Laboratory at UCSB, following the procedures described in Kylander-Clark et al. (2013; 2017). Trace elements were measured on an Agilent 7700X quadrupole ICP-MS. A Cetac/Photon Machines 193 nm Analyte excimer laser was used to ablate samples in a double-chambered HelEx cell. The sample spot size was 25 μm. Every 10 sample spots were bracketed with the primary zircon standard 91500 (Wiedenbeck et al., 1995), and every other block was bracketed with the secondary zircon standard GJ1 (Jackson et al., 2004), and tertiary standards in a rotating list. All experiments included Plešovice (Sláma et al., 2008) as a tertiary standard and others included a selection of MudTank (Black and Gulson, 1978; Gain et al., 2019), Peixe (Dickinson and Gehrels, 2003), FC-1 (Paces and Miller, 1993), 94-35 (Klepeis et al., 1998; Chang et al., 2006), or R33 (Black et al., 2004). For some experiments, a NIST612 spot was added to every block prior to the 91500 spot to regulate the laser arm movement.

Data were reduced using iolite4 software (Paton et al., 2010, 2011) and IsoplotR (Vermeesch, 2018). Standard error (2σ) was propagated using methods described in Paton et al. (2010). The long-term excess variance is captured by 2% uncertainty (2σ) on $^{206}Pb/^{238}U$ ratios and 1.5% (2σ) for $^{207}Pb/^{206}Pb$ ratios for the setups used (Kylander-Clark et al., 2013; Horstwood et al., 2016). These percentages represent systematic uncertainties that are the limiting uncertainties for the data produced and cannot be reduced by increasing the number of analyses (Horstwood et al., 2016); therefore, no uncertainties less than these percentages for the respective ratios were used. $^{207}Pb/^{235}U$ ratios were calculated and uncertainties were propagated from $^{207}Pb/^{206}Pb$ and $^{206}Pb/^{238}U$ ratios and uncertainties using the $^{238}U/^{235}U$ value of 137.818 ± 0.045 (2σ; Hiess et al., 2012). Correlation coefficients were subsequently

141

recalculated using the updated uncertainties. Dates and their uncertainties were also recalculated in IsoplotR (Vermeesch, 2018). Complete analytical data are presented in Table S3.

3. Carbon and oxygen isotope procedures

Carbonate samples were cut with a saw perpendicular to lamination. Between 5-20 mg of powder were micro-drilled from the individual laminations (where visible), avoiding veining, cracks, and siliciclastic components. Isotopic analyses were performed on aliquots of this powder. Carbonate $\delta^{13}C$ and $\delta^{18}O$ isotopic data were acquired simultaneously on a VG Optima dual inlet mass spectrometer attached to a VG Isocarb preparation device at Harvard University. Approximately 1 mg of sample powder was reacted in a purified H_3PO_4 bath at 90°C. Degassed CO_2 was collected cryogenically and analyzed using an in-house reference gas. External error (1σ) from standards was better than ± 0.1 per mil for both $\delta^{13}C$ and $\delta^{18}O$. Samples were calibrated to Vienna Pee-Dee Belemnite (VPDB) using the Cararra marble standard. The memory effect potentially resulting from the common acid-bath system was minimized by increasing the reaction time for dolomite samples. Memory effect is estimated at ± 0.1 per mil based on variability of standards run after dolomite samples. Carbon ($\delta^{13}C$) and oxygen ($\delta^{18}O$) isotopic results are reported in per mil notation of $^{13}C/^{12}C$ and $^{18}O/^{16}O$, respectively, relative to the standard VPDB. Complete analytical data are presented in Table S4.

References

Black, L.P. et al., 2004, Improved $^{206}Pb/^{238}U$ microprobe geochronology by the monitoring of a trace-element-related matrix effect; SHRIMP, ID-TIMS, ELA-ICP-MS and oxygen

isotope documentation for a series of zircon standards: Chemical Geology, v. 205, p. 115–140, doi:10.1016/j.chemgeo.2004.01.003.

Black, L.P., and Gulson, B.L., 1978, The age of the Mud Tank carbonatite, Strangways Range, Northern Territory: BMR Journal of Australian Geology and Geophysics, v. 3, p. 227–232.

Chang, Z., Vervoort, J.D., McClelland, W.C., and Knaack, C., 2006, U-Pb dating of zircon by LA-ICP-MS: Geochemistry, Geophysics, Geosystems, v. 7, doi:10.1029/2005GC001100.

Condon, D.J., Schoene, B., McLean, N.M., Bowring, S.A., and Parrish, R.R., 2015, Metrology and traceability of U-Pb isotope dilution geochronology (EARTHTIME Tracer Calibration Part I): Geochimica et Cosmochimica Acta, v. 164, p. 464–480, doi:10.1016/j.gca.2015.05.026.

Dickinson, W.R., and Gehrels, G.E., 2003, U-Pb ages of detrital zircons from Permian and Jurassic eolian sandstones of the Colorado Plateau, USA: Paleogeographic implications: Sedimentary Geology, v. 163, p. 29–66, doi:10.1016/S0037-0738(03)00158-1.

Gain, S.E.M., Gréau, Y., Henry, H., Belousova, E., Dainis, I., Griffin, W.L., and O'Reilly, S.Y., 2019, Mud Tank Zircon: Long-Term Evaluation of a Reference Material for U-Pb Dating, Hf-Isotope Analysis and Trace Element Analysis: Geostandards and Geoanalytical Research, v. 43, p. 339–354, doi:10.1111/ggr.12265.

Hiess, J., Condon, D.J., McLean, N., and Noble, S.R., 2012, ^{238}U/^{235}U systematics in terrestrial uranium-bearing minerals: Science, v. 335, p. 1610–1614, doi:10.1126/science.1215507.

Horstwood, M.S.A. et al., 2016, Community-Derived Standards for LA-ICP-MS U-(Th-)Pb Geochronology – Uncertainty Propagation, Age Interpretation and Data Reporting: Geostandards and Geoanalytical Research, v. 40, p. 311–332, doi:10.1111/j.1751-908X.2016.00379.x.

Jackson, S.E., Pearson, N.J., Griffin, W.L., and Belousova, E.A., 2004, The application of laser ablation-inductively coupled plasma-mass spectrometry to in situ U-Pb zircon geochronology: Chemical Geology, v. 211, p. 47–69, doi:10.1016/j.chemgeo.2004.06.017.

Jaffey, A.H., Flynn, K.F., Glendenin, L.E., Bentley, W.C., and Essling, A.M., 1971, Precision measurement of half-lives and specific activities of 235U and 238U: Physical Review C, v. 4, p. 1889–1906, doi:10.1103/PhysRevC.4.1889.

Klepeis, K.A., Crawford, M.L., and Gehrels, G., 1998, Structural history of the crustal-scale Coast shear zone north of Portland Canal, southeast Alaska and British Columbia: Journal of Structural Geology, v. 20, p. 883–904, doi:10.1016/S0191-8141(98)00020-0.

Krogh, T.E., 1973, A low-contamination method for hydrothermal decomposition of zircon and extraction of U and Pb for isotopic age determinations: Geochimica et Cosmochimica Acta, v. 37, p. 485–494.

Kylander-Clark, A.R.C., 2017, Petrochronology by Laser-Ablation Inductively Coupled Plasma Mass Spectrometry: Reviews in Mineralogy and Geochemistry, v. 83, p. 183–198, doi:10.2138/rmg.2017.83.6.

Kylander-Clark, A.R.C., Hacker, B.R., and Cottle, J.M., 2013, Laser-ablation split-stream ICP petrochronology: Chemical Geology, v. 345, p. 99–112, doi:10.1016/j.chemgeo.2013.02.019.

Mattinson, J.M., 2005, Zircon U-Pb chemical abrasion ("CA-TIMS") method: Combined annealing and multi-step partial dissolution analysis for improved precision and accuracy of zircon ages: Chemical Geology, v. 220, p. 47–66, doi:10.1016/j.chemgeo.2005.03.011.

Morris, F.K., and Grotzinger, J.P., 2023, Facies and stratigraphy of the basal Ediacaran cap carbonate, Naukluft Mountains, Namibia: Precambrian Research, v. 394, p. 107113, doi:10.1016/j.precamres.2023.107113.

Paces, J.B., and Miller, J.D., 1993, Precise U-Pb ages of Duluth Complex and related mafic intrusions, northeastern Minnesota: Geochronological insights to physical, petrogenetic, paleomagnetic, and tectonomagmatic processes associated with the 1.1 Ga Midcontinent Rift System: Journal of Geophysical Research: Solid Earth, v. 98, p. 13997–14013, doi:10.1029/93JB01159.

Paton, C., Hellstrom, J., Paul, B., Woodhead, J., and Hergt, J., 2011, Iolite: Freeware for the visualisation and processing of mass spectrometric data: Journal of Analytical Atomic Spectrometry, v. 26, p. 2508, doi:10.1039/c1ja10172b.

Paton, C., Woodhead, J.D., Hellstrom, J.C., Hergt, J.M., Greig, A., and Maas, R., 2010, Improved laser ablation U-Pb zircon geochronology through robust downhole fractionation correction: Geochemistry, Geophysics, Geosystems, v. 11, doi:10.1029/2009GC002618.

Schmitz, M.D., and Schoene, B., 2007, Derivation of isotope ratios, errors, and error correlations for U-Pb geochronology using 205Pb-235U-(233U)-spiked isotope dilution thermal ionization mass spectrometric data: Geochemistry, Geophysics, Geosystems, v. 8, p. 1–20, doi:10.1029/2006GC001492.

Sláma, J. et al., 2008, Plešovice zircon — A new natural reference material for U – Pb and Hf isotopic microanalysis: v. 249, p. 1–35, doi:10.1016/j.chemgeo.2007.11.005.

Stacey, J.S., and Kramers, J.D., 1975, Approximation of terrestrial lead isotope evolution by a two-stage model: Earth and Planetary Science Letters, v. 26, p. 207–221, doi:10.1016/0012-821X(75)90088-6.

Vermeesch, P., 2018, IsoplotR: A free and open toolbox for geochronology: Geoscience Frontiers, v. 9, p. 1479–1493, doi:10.1016/j.gsf.2018.04.001.

Wiedenbeck, M., Allé, P., Corfu, F., Griffin, W. l., Meier, M., Oberli, F., Von Quadt, A., Roddick, J.C., and Spiegel, W., 1995, Three Natural Zircon Standards for U-Th-Pb, Lu-Hf, Trace Element and REE Analyses: Geostandards and Geoanalytical Research, v. 19, p. 1–23, doi:10.1111/j.1751-908X.1995.tb00147.x.

Section	Lat (°)	Long (°)
F828	-24.07355	16.32011
F829	-24.07631	16.31393
P3204	-24.0752	16.3141
JP1712	-24.07526	16.31075
JP1713	-24.07333	16.30472
JP1714	-24.07056	16.30500
JP1715	-24.07306	16.30694
JP1807	-24.11719	16.20871
JP1808	-24.10810	16.21672
JP1809	-24.07803	16.31278
JP1810	-24.07375	16.30658
JP1901	-24.09816	16.23934
JP1902	-24.09961	16.24218
JP1903	-24.09883	16.25006
JP1904	-24.09599	16.25903
JP1905	-24.09010	16.26578
JP1906	-24.08953	16.26974
JP1907	-24.08768	16.27725
JP1908	-24.08691	16.28019
JP1909	-24.07594	16.31492
JP1910	-24.07294	16.32045
JP1911	-24.05740	16.32864

Table S1. Section locations

Farm Blässkranz, Naukluft allochthon, Namibia
P3204, F828, F829

146
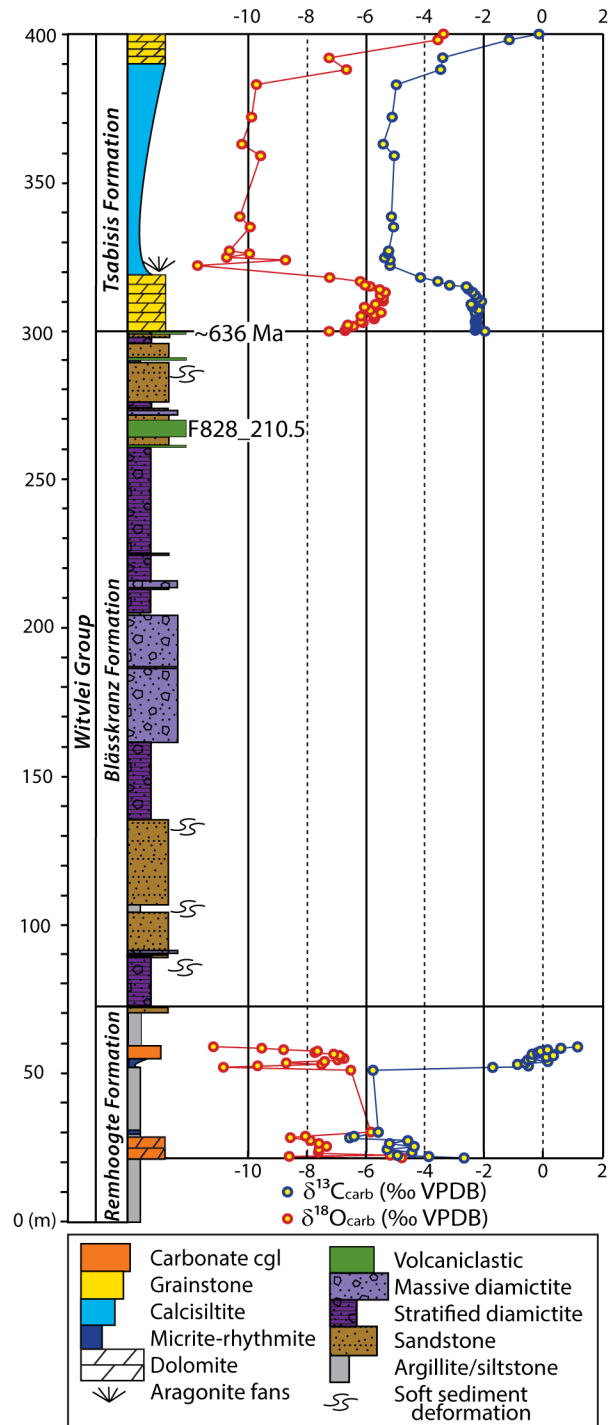
Figure S1. Carbon isotope chemostratigraphy of the Naukluft Nappes. Analyses of $\delta^{13}C_{carb}$ and $\delta^{18}O_{carb}$ from carbonate debrites at the top of the Remhoogte Formation show anomalously negative values that correlate with the Trezona excursion preceding the Marinoan Snowball Earth event. Up-section in the cap carbonate of the Tsabisis Formation, another negative anomaly can be seen that has been correlated with the Ediacaran Maieberg excursion, consistent with published data for this locality presented in Morris and Grotzinger (2023).

	Compositional Parameters					Radiogenic Isotope Ratios							Isotopic Ages					
Sample	Th/U	Pb*/Pbc	Pbc (pg)	206Pb/204Pb	208Pb/206Pb	207Pb/206Pb	2σ %err	207Pb/235U	2σ %err	206Pb/238U	2σ %err	corr. coef.	207Pb/206Pb	2σ abs	207Pb/235U	2σ abs	206Pb/238U	2σ abs
(a)	(b)	(c)	(c)	(d)	(e)	(e)	(f)	(e)	(f)	(e)	(f)		(g)	(f)	(g)	(f)	(g)	(f)
F828-210.5, 206Pb/238U weighted mean date = 635.84 ± 0.22/0.29/0.71 Ma, n = 11, MSWD = 1.62																		
z3	0.689	1	3.97	63	0.214	0.060986	2.817	0.866680	3.028	0.103115	0.780	0.390	637.77	60.60	633.76	14.27	632.64	4.70
z4	0.559	3	2.30	193	0.174	0.060422	1.033	0.863888	1.142	0.103743	0.277	0.496	617.74	22.30	632.24	5.38	636.31	1.68
z5	0.773	10	1.08	592	0.240	0.060884	0.602	0.868952	0.657	0.103559	0.109	0.568	634.17	12.95	635.00	3.10	635.23	0.66
z6	0.428	2	1.48	153	0.133	0.060580	2.527	0.866845	2.718	0.103826	0.237	0.821	623.38	54.50	633.85	12.82	636.79	1.44
z7	0.580	1	5.37	75	0.180	0.061717	1.828	0.881736	1.931	0.103664	0.460	0.337	663.35	39.15	641.92	9.19	635.85	2.78
z8	1.257	4	0.76	206	0.390	0.061438	2.236	0.897083	2.611	0.105947	1.063	0.531	653.64	47.98	650.17	12.54	649.17	6.56
z9	1.330	1	8.08	80	0.413	0.061417	1.589	0.879171	1.730	0.103867	0.629	0.396	652.91	34.10	640.53	8.22	637.03	3.82
z12	0.531	5	0.50	315	0.165	0.060110	1.120	0.849737	1.211	0.102573	0.191	0.543	606.55	24.21	624.50	5.65	629.47	1.14
z13	0.579	9	0.74	547	0.180	0.060043	0.627	0.857029	0.686	0.103568	0.100	0.635	604.16	13.57	628.50	3.21	635.29	0.61
z15	0.565	3	0.51	194	0.176	0.060181	2.167	0.858736	2.350	0.103537	0.530	0.445	609.11	46.84	629.43	11.03	635.11	3.20
z17	0.801	4	0.45	234	0.249	0.060453	1.693	0.864822	1.804	0.103801	0.232	0.528	618.86	36.53	632.75	8.49	636.65	1.41
z19	0.661	8	0.61	467	0.205	0.060716	1.170	0.869173	1.259	0.103872	0.189	0.530	628.21	25.21	635.12	5.94	637.06	1.15
z20	0.604	6	0.57	381	0.188	0.060247	0.955	0.859739	1.037	0.103544	0.161	0.565	611.48	20.63	629.98	4.87	635.15	0.98
z21	0.621	10	0.46	593	0.193	0.060553	0.631	0.864816	0.693	0.103629	0.121	0.579	622.44	13.61	632.75	3.26	635.64	0.73
z22	0.456	5	0.63	340	0.141	0.061086	1.235	0.873421	1.327	0.103748	0.173	0.579	641.29	26.55	637.42	6.28	636.33	1.05
z23	0.588	33	0.71	1934	0.183	0.060677	0.179	0.867192	0.228	0.103701	0.080	0.721	626.84	3.86	634.04	1.08	636.06	0.49
z24	0.524	34	0.79	2026	0.163	0.060567	0.201	0.865679	0.244	0.103709	0.068	0.723	622.91	4.33	633.22	1.15	636.11	0.41
JP1715-187.9, 206Pb/238U weighted mean date = 635.93 ± 0.56/0.59/0.88 Ma, n = 3, MSWD = 2.04																		
z1	1.121	16	0.35	826	0.348	0.061355	0.452	0.881193	0.508	0.104212	0.130	0.535	650.73	9.71	641.63	2.42	639.04	0.79
z2	0.938	20	0.41	1114	0.291	0.061058	0.311	0.878333	0.374	0.104378	0.140	0.601	640.31	6.68	640.08	1.77	640.02	0.85
z3	0.659	42	0.30	2438	0.205	0.060888	0.193	0.871010	0.268	0.103797	0.146	0.715	634.32	4.16	636.12	1.27	636.62	0.88
z4	1.487	18	0.33	867	0.462	0.061366	0.385	0.878644	0.479	0.103891	0.217	0.618	651.14	8.27	640.25	2.28	637.17	1.32
z5	0.657	15	0.62	888	0.204	0.060966	0.372	0.876126	0.425	0.104273	0.109	0.584	637.08	8.00	638.89	2.02	639.40	0.66
z7	0.526	11	0.45	671	0.163	0.060975	0.523	0.873690	0.586	0.103967	0.140	0.542	637.40	11.26	637.57	2.77	637.62	0.85
z8	0.555	29	0.69	1740	0.172	0.060866	0.209	0.868852	0.340	0.103578	0.237	0.794	633.52	4.50	634.94	1.60	635.34	1.43
z9	1.383	7	0.74	356	0.429	0.061497	0.987	0.882740	1.065	0.104153	0.162	0.536	655.69	21.18	642.46	5.07	638.70	0.98
z10	0.754	43	0.37	2448	0.233	0.063109	0.134	1.018720	0.221	0.117126	0.165	0.797	710.96	2.85	713.27	1.13	714.00	1.12
z11	0.867	89	0.20	4858	0.269	0.061062	0.073	0.867494	0.118	0.103083	0.084	0.788	640.46	1.58	634.21	0.56	632.45	0.51
z12	0.758	80	0.24	4481	0.236	0.060993	0.088	0.870921	0.170	0.103607	0.139	0.856	638.03	1.89	636.07	0.80	635.52	0.84
z13	1.181	145	0.14	7390	0.367	0.061018	0.074	0.877145	0.227	0.104305	0.211	0.945	638.91	1.59	639.44	1.08	639.59	1.29
JP1713-193.7, 206Pb/238U date = 635.76 ± 0.79/0.81/1.04 Ma, n = 1																		
z1	0.649	14	0.66	813	0.202	0.061032	0.413	0.874486	0.462	0.103966	0.090	0.612	639.39	8.89	638.00	2.19	637.61	0.55
z2	0.547	8	1.96	466	0.170	0.061131	0.403	0.873234	0.465	0.103649	0.130	0.587	642.87	8.66	637.32	2.20	635.76	0.79
z4	0.603	6	3.08	368	0.187	0.061145	0.377	0.875677	0.435	0.103914	0.121	0.588	643.38	8.11	638.65	2.06	637.31	0.73
z6	1.310	47	0.37	2329	0.407	0.061013	0.281	0.882533	0.281	0.104955	0.201	0.831	638.72	3.44	642.35	1.34	643.38	1.23
z7	1.387	35	0.53	1705	0.431	0.061005	0.211	0.879969	0.257	0.104664	0.078	0.684	638.44	4.55	640.97	1.22	641.68	0.48
z8	0.559	140	0.24	8237	0.173	0.063294	0.077	1.025082	0.138	0.117514	0.069	0.932	717.17	1.64	716.46	0.71	716.24	0.47
z11	1.227	21	0.44	1083	0.381	0.060876	0.446	0.873781	0.490	0.104148	0.091	0.552	633.89	9.61	637.62	2.32	638.67	0.55

Table S2. U-Pb CA-ID-TIMS data. Analyses in red were not included in 206Pb/238U weighted mean date calculations. Analyses that were more than 10% discordant or not run to completion due to high blanks and/or low amounts of radiogenic Pb have been removed. (a) z1, z2 etc. are labels for single zircon grains or fragments annealed and chemically abraded after Mattinson (2005). (b) Model Th/U ratio iteratively calculated from the radiogenic ^{208}Pb/^{206}Pb ratio and ^{206}Pb/^{238}U age. (c) Pb* and Pbc represent radiogenic and common Pb, respectively; mol % ^{206}Pb* with respect to radiogenic, blank and initial common Pb. (d) Measured ratio corrected for spike and fractionation only. Fractionation estimated at 0.18 +/- 0.03 %/a.m.u. for Daly analyses, based on analysis of NBS-981 and NBS-982. (e) Corrected for fractionation, spike, and common Pb; up to 1 pg of common Pb was assumed to be procedural blank: ^{206}Pb/^{204}Pb = 18.042 ± 0.61%; ^{207}Pb/^{204}Pb = 15.537 ± 0.52%; ^{208}Pb/^{204}Pb = 37.686 ± 0.63% (all uncertainties 1σ). Excess over blank was assigned to initial common Pb, using the Stacey and Kramers (1975) two-stage Pb isotope evolution model at the nominal sample age. (f) Errors are 2σ, propagated using the algorithms of Schmitz and Schoene (2007). (g) Calculations are based on the decay constants of Jaffey et al. (1971). ^{206}Pb/^{238}U and ^{207}Pb/^{206}Pb ages corrected for initial disequilibrium in ^{230}Th/^{238}U using Th/U [magma] = 3.

Table S3. U-Pb LA-ICPMS data (separate Excel file)

F828: -24.07355°S, 16.32011°E; Tsabisis Formation

Sample	$\delta^{18}O$	$\delta^{13}C$
2.0	-6.53	-5.76
3.0	-10.85	-1.70
3.5	-9.69	-0.49
4.0	-7.52	-0.86
4.5	-8.72	-0.60
5.0	-7.42	0.17
5.5	-6.97	-0.51
6.0	-6.76	-0.38
6.5	-6.88	0.12
7.0	-6.91	0.36
7.5	-7.11	-0.36
8.0	-7.75	-0.18
8.5	-7.66	-0.08
9.0	-8.81	0.16
9.5	-9.55	0.61
10.0	-11.19	1.18

F829: 24.07631°S, 16.31393°E; Remhoogte Formation

Sample	$\delta^{18}O$	$\delta^{13}C$
0.1	-4.80	-2.67
0.6	-8.62	-3.87
1.0	-5.19	-4.93
2.0	-7.63	-4.44
3.0	-7.61	-5.28
4.0	-7.35	-4.36
5.0	-7.61	-5.20
6.0	-7.90	-4.58
7.0	-8.58	-6.55
7.5	-8.07	-6.40
8.9	-5.85	-5.58
30.0	-6.53	-5.76
31.0	-10.85	-1.70
31.5	-9.69	-0.49
32.0	-7.52	-0.86
32.5	-8.72	-0.60
33.0	-7.42	0.17
33.5	-6.97	-0.51
34.0	-6.76	-0.38
34.5	-6.88	0.12
35.0	-6.91	0.36
35.5	-7.11	-0.36
36.0	-7.75	-0.18
36.5	-7.66	-0.08
37.0	-8.81	0.16

37.5	-9.55	0.61
38.0	-11.19	1.18

P3204: 24.0752°S, 16.3141°E; Tsabisis Formation

Sample	$\delta^{18}O$	$\delta^{13}C$
0	-6.67	-2.02
0.2	-7.20	-2.03
0.5	-6.80	-2.30
1.1	-6.76	-2.26
1.6	-6.52	-2.32
2.1	-6.69	-2.32
2.7	-6.08	-2.23
3.1	-6.15	-2.36
4.1	-5.84	-2.31
4.4	-5.72	-2.25
5	-6.22	-2.22
5.5	-5.77	-2.32
6		
6.3	-5.59	-2.35
7	-5.94	-2.17
8	-6.07	-2.45
9	-5.72	-2.54
10	-5.40	-2.13
11.2	-5.38	-2.24
12.1	-5.58	-2.37
13	-5.36	-2.42
14	-5.59	-2.59
14.5	-5.60	-2.88
14.9	-5.80	-3.01
15	-5.94	-2.67
15.7	-6.13	-3.16
16.7	-6.18	-3.68
18	-7.25	-4.24
20.9	-8.25	-4.72
22	-11.52	-5.15
23.8	-8.69	-5.11
24.7	-10.65	-5.35
26	-9.97	-5.21
27	-10.48	-5.17
35	-9.77	-5.04
38.5	-10.23	-5.10
50		
52.5	-10.13	-4.51
59	-9.61	-5.02
62.5	-10.08	-5.39
72	-9.90	-5.08
79.5		

83	-9.70	-4.99
88	-6.75	-3.66
92	-7.20	-3.40
98	-3.74	-1.15
100	-3.44	-0.18

Table S4. Carbon and oxygen isotope data.